

Pontificia Universidad Católica del Perú

Escuela de Posgrado



Testing pALPIDE sensors for particle detection and
Characterization of a Laser beam using a webcam
CMOS sensor

Tesis para optar el grado académico de Doctor en Física que presenta:

M.Sc. Carlos Soncco Meza

Asesor: Dr. Alberto Martin Gago Medina

Co-asesor: Dr. José Luis Bazo Alba

Lima, 2022

Informe de similitud

Yo, Alberto Martin Gago Medina, docente de la Escuela de Posgrado de la Pontificia Universidad Católica del Perú, asesor(a) de la tesis/el trabajo de investigación titulado *Testing pALPIDE sensors for particle detection and Characterization of a Laser beam using a webcam CMOS sensor* del autor Carlos Soncco Meza,


dejo constancia de lo siguiente:

- El mencionado documento tiene un índice de puntuación de similitud de 20% Así lo consigna el reporte de similitud emitido por el software *Turnitin* el 20/11/2022.
- He revisado con detalle dicho reporte y confirmo que cada una de las coincidencias detectadas no constituyen plagio alguno.
- Las citas a otros autores y sus respectivas referencias cumplen con las pautas académicas.

Lugar _____ y _____

fecha:

Lima, 13 de diciembre de 2022

Apellidos y nombres del asesor / de la asesora: <u>Gago Medina, Alberto Martín</u>	
DNI: 07835422	Firma: 
ORCID: 0000-0002-0019-9692	

Abstract

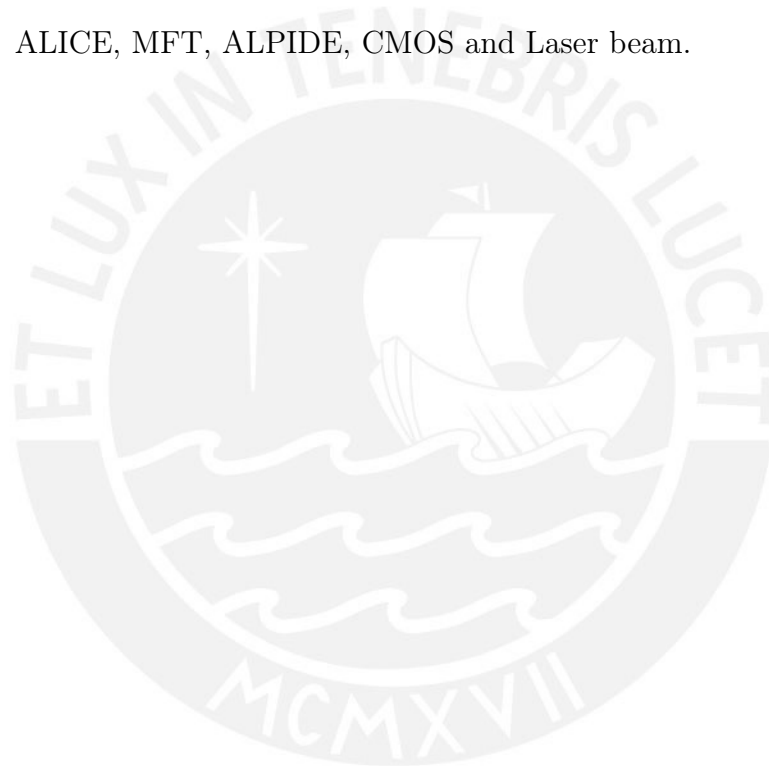
The upgrade program of the Large Hadron Collider (LHC) was implemented during the second Long Shutdown program (2019/2020). For this program, the ALICE Collaboration (A Large Ion Collider Experiment) proposed, among others, a new detector called Muon Forward Tracker (MFT). The primary goal of the MFT detector, installed on December 2021 and located between the Inner Tracker System (ITS) and the Muon Spectrometer, is to improve the capability of vertex reconstruction. The MFT is equipped with the same pixel sensors used for the ITS upgrade. These sensors are the ALICE Pixel Detectors (ALPIDE), a kind of monolithic active pixel sensor. The MFT is composed of five arrays of pixel sensors which are configured as parallel discs covering $-3.6 < \eta < -2.45$.

Some prototypes were designed in order to achieve the final version of the ALPIDE, such as the pALPIDE family, which was divided into three versions (i.e., pALPIDE-1,2,3). The ALICE upgrade also included a new system for the data taking and simulation called Online-offline (O2) to replace AliRoot. We designed the geometry of two non-active parts of the MFT and included them in the O2 system.

The first goal of this thesis is focused on the characterization of the pALPIDE-2. This sensor is segmented into four groups corresponding to four types of pixels. This characterization includes the test of analogue and digital. According to these tests, we identified a group of pixels that do not work correctly. The threshold scan tests showed the threshold level in each pixel is influenced by the input capacitance according to its n-well size and the surrounding area. Also, we studied the response of the pALPIDE-2 when it was exposed to a soft x-ray source, varying the distance between them. This test showed that the hit count changed according to the inverse square of the distance.

The second goal of this thesis was to implement a low-cost tool based on a CMOS sensor to characterize laser beams. This tool comprises a Raspberry, a Pi Camera with a pitch size of $1.4 \mu\text{m}$, and an optical system. To test the accuracy of the results of this tool, we made similar measurements with other sensors. A photodiode and a light-dependent resistor performed these measurements, which showed the spot radius size compatibility. However, the CMOS sensor expressed the highest precision and is a more affordable tool than commercial devices.

Keywords: ALICE, MFT, ALPIDE, CMOS and Laser beam.



Resumen

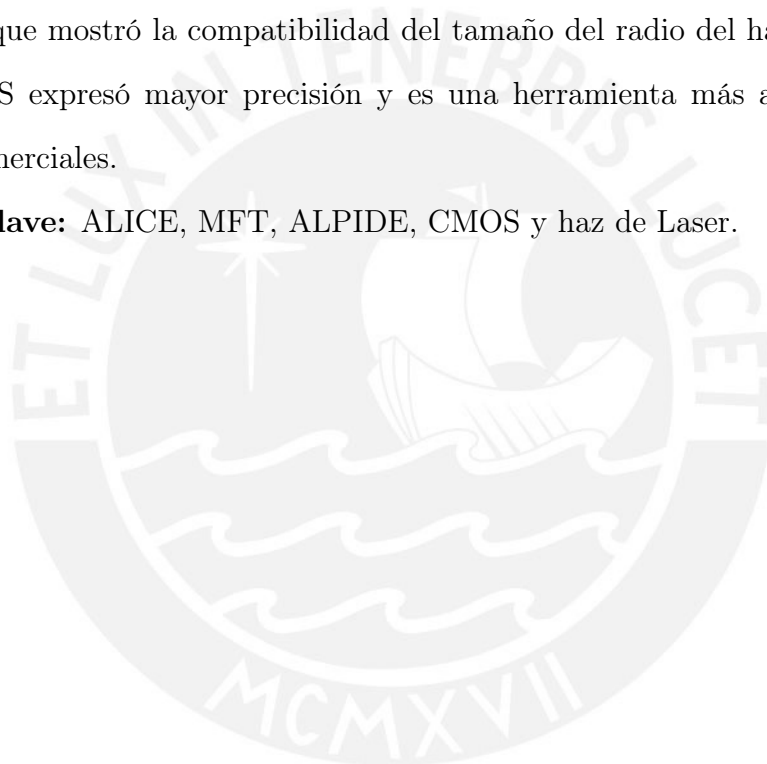
El programa de actualización del Gran Colisionador de Hadrones (LHC) se implementó durante el segundo programa de Apagado prolongado (2019/2020). Para el programa, la Colaboración ALICE (A Large Ion Collider Experiment) propuso, entre otros, un nuevo detector llamado Muon Forward Tracker (MFT). El objetivo principal del detector MFT, instalado en diciembre de 2021 y ubicado entre el sistema de seguimiento interno (ITS) y el espectrómetro de muones, es mejorar la capacidad de reconstrucción de vértices. El MFT está equipado con los mismos sensores de píxeles utilizados para la actualización de ITS. Estos sensores son los detectores de píxeles ALICE (ALPIDE), una especie de sensor monolítico de píxeles activos. El MFT está compuesto por cinco conjuntos de sensores de píxeles que están configurados como discos paralelos que cubren $-3.6 < \eta < -2.45$. Se diseñaron algunos prototipos para lograr la versión final del ALPIDE, como la familia pALPIDE, que se dividió en tres versiones (i.e., pALPIDE-1,2,3). La actualización de ALICE también incluyó un nuevo sistema para la toma de datos y simulación llamado Online-offline (O2) para reemplazar a AliRoot. Diseñamos la geometría de dos partes no activas del MFT y las incluimos en el sistema O2.

El primer objetivo de esta tesis se centra en la caracterización del pALPIDE-2. Este sensor está segmentado en cuatro grupos correspondientes a cuatro tipos de píxeles. Esta caracterización incluye la prueba de analógico y digital. Según estas pruebas, identificamos un grupo de píxeles que no funcionan correctamente. Las pruebas de escaneo de umbral mostraron que el nivel de umbral en cada píxel está influenciado por la capacitancia de entrada de acuerdo con su tamaño de n pozos y el área circundante. También estudiamos la respuesta del pALPIDE-2 cuando fue expuesto a una fuente de rayos X blanda, variando

la distancia entre ellos. Esta prueba mostró que el conteo de pixeles activados cambiaba según el inverso del cuadrado de la distancia.

El segundo objetivo de esta tesis fue implementar una herramienta de bajo costo basada en un sensor CMOS para caracterizar rayos láser. Esta herramienta consta de un Raspberry, una cámara Pi con un tamaño de pixel de $1,4 \mu\text{m}$ y un sistema óptico. Para probar la precisión de los resultados de esta herramienta, realizamos mediciones similares con otros sensores. Un fotodiodo y una resistencia dependiente de la luz realizaron estas mediciones, lo que mostró la compatibilidad del tamaño del radio del haz. Sin embargo, el sensor CMOS expresó mayor precisión y es una herramienta más asequible que los dispositivos comerciales.

Palabras clave: ALICE, MFT, ALPIDE, CMOS y haz de Laser.



Acknowledgements

Thanks to all my family and people who help me to finish this step of my life. With special grateful to Miguel Bonnett, Rodrigo Helaconde, José Bazo and Alberto Gago. Also, my gratitude is to the Optic Quantum and applied optics teams.

Finally, thank Ciencia Activa-CONCYTEC 2016.



Contents

Abstract	iii
Acknowledgements	vii
Contents	viii
List of Figures	xi
List of Tables	xv
Introduction	1
1 Heavy Ions Physics Collider	3
1.1 Physics of the strong interaction	3
1.1.1 Quantum Chromodynamics	4
1.1.2 QCD Phases	5
1.1.3 Lattice	9
1.1.4 Heavy ion collisions	9
1.1.5 Space-time evolution of the ion collision	11
1.1.6 Signature or observables of QGP	11
1.1.7 Elliptic Flow	16
1.2 The ALICE experiment	17
1.2.1 ALICE detector	18

1.2.2	The Inner Tracking System	20
1.2.3	Time Projection Chamber (TPC)	22
1.2.4	Fast Interaction Trigger (FIT)	23
1.2.5	Muon spectrometer	24
2	The Muon Forward Tracker	27
2.1	The Ladder	28
2.2	The half-disk	29
2.3	MFT half-barrel	30
2.4	Online-offline computing system	31
3	Monolithic Active Pixel Sensors	37
3.1	Charge Generation and Collection in MAPS	37
3.1.1	Energy loss of charged particles	38
3.1.2	Energy loss of electromagnetic radiation	39
3.1.3	Collection diode	40
3.2	Principles of Operation of MAPS	42
3.2.1	Signal formation	43
3.2.2	Spatial resolution	44
3.3	Radiation damage effects	45
3.4	Small scale prototypes	46
3.5	pALPIDE-1 sensor	47
3.6	pALPIDE-2 sensor	48
3.6.1	Pixel matrix	50
3.6.2	Front-end circuit	50
3.7	pALPIDE-3	53
3.8	ALPIDE sensor	54
3.8.1	Pixel ALPIDE Architecture	55

3.9	Digital Scan	57
3.10	Analogue Scan	58
3.11	Threshold Scan Studies	59
3.12	Fake hit rate	63
3.13	Radioactive Source Iron-55	66
3.13.1	Experimental setup	68
3.13.2	Data taking and analysis	69
4	Laser characterization with a CMOS sensor.	74
4.1	The laser	75
4.1.1	Transverse Electromagnetic Mode of a laser	75
4.2	Experimental Setup	78
4.2.1	Photodiode	79
4.2.2	The Raspberry Pi Camera	80
4.2.3	Light Dependent Resistor	80
4.2.4	Laser Type	80
4.3	Measurements of the spot profile	81
4.3.1	Measurements of the spot size using three different sensors	84
4.4	Comparing prices of sensors	87
5	Conclusions	88
	Bibliography	90

List of Figures

1.1	Represent the universe's evolution, since the big bang up to present era. . .	3
1.2	The Standard model particle classification.	5
1.3	Representation of the change in the strong constant with respect to quark distance.	6
1.4	Representation of transition from confined to deconfined state according lattice QCD.	7
1.5	Schematic representation of QGP phase, Temperature vs chemical potential.	8
1.6	Representation of vector impact parameter on the transverse side.	10
1.7	Schematic representation number of participant and spectator.	11
1.8	Schematic representation space-time evolution of the heavy ion collisions .	12
1.9	Schematic representation of different photons created in each step after ions collision	14
1.10	Charmonium state in QGP	15
1.11	Anisotropic flow representation in the transverse plane	16
1.12	Schematic view of the Large Hadron Collider and the four major experiment.	17
1.13	Perpendicular view of detectors of ALICE.	19
1.14	Schematic view of the ALICE detector.	20
1.15	A Schematic representation of a transverse view of the seven-layer of the ITS configured in three barrels.	21
1.16	Position's stave forming the layers for the upgraded ITS.	22

1.17	View of the TPC shape compared with a man, including the two plates segmented to readout and the electrode.	23
1.18	Schematic view of size and geometry of the FIT, including the location with respect to other detectors.	24
1.19	The ALICE muon spectrometer.	25
2.1	Schematic representation of the MFT detector.	28
2.2	View of half-MFT located between the inner barrel and the absorber.	29
2.3	Schematic representation of the half-cone	30
2.4	Ladders with different numbers of sensors.	31
2.5	Elements of a half-disk.	32
2.6	Frontal view of half-disk-0.	33
2.7	Schematic view of the half-barrel.	34
2.8	Half-cone geometry implemented in O2 geometry.	34
2.9	Patch-panel geometry implemented in O2 geometry.	35
2.10	The a represent the second version and b is the final version of <i>half-cone</i>	35
2.11	View of MFT geometry implemented in O2 geometry.	36
3.1	p-n junction process.	41
3.2	Schematic MAPS cross-section, where a charged particle is crossing the sensor.	43
3.3	View of the cross-section pixel pALPIDE, and top view of the charge collector.	47
3.4	Position of the four sectors in the pALPIDE-1 and pALPIDE-2.	48
3.5	The pixel matrix is organized in double-columns and each of them shares a priority encoder.	50
3.6	The pALPIDEfs-2 reset mechanisms.	51
3.7	Schematic view of analogue front-end for pALPIDE-2.	52
3.8	The digital part at the front-end for pALPIDE-2	53

3.9	Schematic representation of the in-pixel circuitry implemented in ALPIDE sensor	55
3.10	Analogue stage of the pixel ALPIDE	56
3.11	Functional diagram of the digital part for the pixel on ALPIDE.	57
3.12	Hit map of the digital scan.	58
3.13	Analogue scan test responds to different injected charges. About 300 pixels are broken.	59
3.14	The $Hits/N_{inj}$ vs injected charge	60
3.15	The threshold value per pixel for the whole pixel matrix	61
3.16	The threshold distribution for all sectors	62
3.17	Mean threshold value in the 32 regions.	63
3.18	The threshold value varying ITH for each sector.	64
3.19	Threshold distribution for four different values of ITH for each sector.	65
3.20	Hit response of pixels at different temperatures.	66
3.21	Hit response of pixels at different temperatures.	67
3.22	Mass attenuation coefficient of air as function of the photon energy.	69
3.23	The geometry of the Fe^{55} source.	70
3.24	Experimental setup for the ^{55}Fe and the pALPIDE-2.	71
3.25	Cumulative hits generated by the X-ray source (^{55}Fe) for different positions.	72
3.26	Cumulative hit generated by ^{55}Fe excluding hits generated by noise and hot pixels. An inverse squared fit for each sector of pALPIDE-2	73
3.27	Cumulative hit normalized for the four sectors of pALPIDE-2 when exposed to a Fe-55 at different distances.	73
4.1	The width of the Gaussian beam varies according to the axial distance, and w_0 is the radius of the waist.	76
4.2	The Gaussian intensity profile of a laser beam.	77

4.3	Schematic representation of the experimental setup.	79
4.4	Raspberry board with electrical connection to the three light sensors: webcam, photodiode, and LDR.	81
4.5	A frame of the laser beam, where the z-axis is the intensity in ADC units .	82
4.6	Variation of the x-radius beam in the function of axis propagation.	83
4.7	Variation of the y-radius beam in the function of axis propagation.	84
4.8	A Gaussian cumulative distribution fit for the voltage measurements of the photodiode.	86



List of Tables

2.1	Number of sensors and ladders distribution in each Half-Disk and in the full MFT.	31
3.1	Characteristics of the four different pixel types of the pALPIDE-1.	48
3.2	Characteristics of the four different pixel types of the pALPIDE-2	49
3.3	Signal of the pixel.	54
3.4	Characteristics of the front end circuit of the pALPIDE-3.	54
3.5	Differences between pALPIDE-2 and ALPIDE (final version)	55
3.6	Mean threshold scan for the whole pixel matrix pALPIDE-2	62
3.7	Mean threshold value sector for four different ITH	62
3.8	The fake hit rate for each sector of the pALPIDE-2	64
3.9	Mean threshold value by sector for four different ITH	65
3.10	Emission channels after ^{55}Fe decays into ^{55}Mn per 100 decays	67
4.1	Comparison of radii obtained from the CMOS sensor with the results from the photodiode and LDR.	87
4.2	Commercial devices to measure a laser beam size	87



Introduction

There are physical phenomena in nature that are far from being fully understood. One of this phenomenon happened a few microseconds after the Big Bang when the Universe was filled with a hot soup of freely moving colored charged quarks and gluons. This deconfined state of matter is called the Quark-Gluon Plasma (QGP) and preceded the hadronization time in the evolution of the Universe. In order to reach the QGP state, high temperature and/or net baryon density are required; the high-temperature condition is attained through relativistic heavy-ion collision experiments [1][2][3].

Experiments such as the Super Proton Synchrotron (SPS) at CERN and the Relativistic Heavy Ion Collider (RHIC) were pioneers in the research of the QGP [1]. In fact, RHIC, using gold-gold collisions with 200 GeV center of mass energy per nucleon, was the first experiment able to recreate the QGP state [2]. At Run-1 ALICE (A Large Ion Collider Experiment) using lead-lead collisions and at 2.76 TeV center of mass energy per nucleon, confirmed results which were found from previous experiments about the QGP [3].

The Large Hadron Collider planned several updates for the third data-taking period, called Run 3. It expects an increase in luminosity in Pb-Pb to 6 nb^{-1} ($1\text{b} = 10^{-24} \text{cm}^2$). This upgrade includes renovating some ALICE detectors with a more efficient reading system. One of them uses new silicon sensor technology, called ALPIDE (Alice Pixel Detector).

According to the ALICE upgrade program, a new detector called Muon Forward

Tracker (MFT) was installed on December 2021 to improve the capability of the muon arm to identify the primary vertex. The MFT is implemented with ALPIDE sensor [4].

The first objective of this thesis is to characterize one of the versions of the ALPIDE family, that is, the pALPIDE-2, which was the only one compatible with the available data acquisition board. This study included digital, threshold, and analog tests. Also, we studied the sensor's response when it was exposed to a radioactive source. Besides, and still related to our contributions to the MFT, two geometrical parts of the MFT were incorporated into the new simulation and data-taking system: O2.

The second objective is to implement an affordable system to characterize laser beams with a commercial CMOS sensor in the process of studying the response of a single-pixel with an infrared pulsed laser.

This work is organized in chapters. In the second chapter, we describe the physics of the strong interaction and the ALICE detector with its upgrade program. The third chapter is focused on the new MFT detector. The fourth chapter describes the pixel sensor which is the active part of the MFT, characterization tests made on the pALPIDE-2 and the response of the pALPIDE-2 when it is exposed to a radioactive source of X-rays. The fifth chapter describes the use of a CMOS sensor to characterize a laser beam. Finally, we give our conclusions.

Chapter 1

Heavy Ions Physics Collider

1.1 Physics of the strong interaction

The world that we know could begin at the Big Bang approximately 13.7 billion years ago when all the universe was concentrated at a point with a temperature of $T = 10^{32}$ K ($T \simeq 10^{19}$ GeV). Then It started to expand and cool. A few microseconds after and at a temperature of about $T > 10^{22}$ K [5], the quarks and gluons were moving freely, known as the Quark Gluon Plasma. Subsequently, the hadronization made its part, forming protons and neutrons, then atoms were formed up to create massive elements, as we see in the sky. The universe's evolutions are shown in Fig. 1.1. The theory used to study the interaction and properties of the QGP is Quantum chromodynamics.

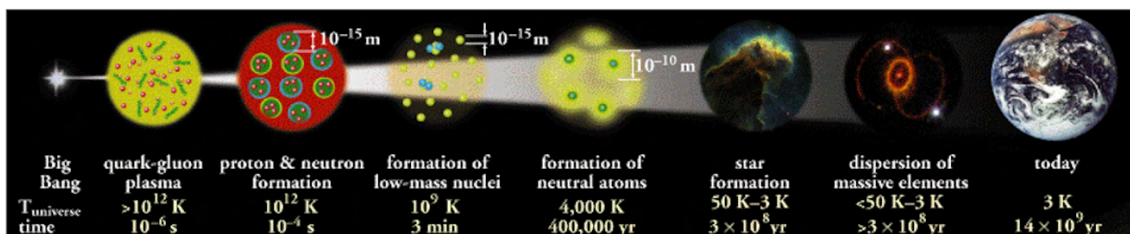


Figure 1.1: Represent the universe's evolution, since the Big Bang up to present era. Image obtained from [6].

1.1.1 Quantum Chromodynamics

The Standard Model(SM) describes three fundamental forces (except gravity): the strong (responsible for confining quarks in protons and neutrons, also binds proton and neutron on the nuclei), the weak (responsible for the radioactive decay), and the electromagnetic (without it, atoms and molecules would never form). It also explains most experimental data; nevertheless, it cannot explain some issues, such as the origin of neutrinos masses, dark matter, and dark energy [7].

The SM classifies particles into two types according to their spin, such as fermions and bosons, which are represented by half-integer and integer spin, respectively, as shown in Fig 1.2. Fermions include the leptons and quarks. On the other hand, bosons are force carriers [8]. Quantum Chromodynamics (QCD) is a gauge field theory that describes the strong force between quarks and mediated by gluons, which are the force carriers. Its Lagrangian is expressed by:

$$L_{QCD} = -\frac{1}{4}F_{\mu\nu}^a F_a^{\mu\nu} + \sum_q i\bar{\psi}\gamma^\mu(\partial_\mu - ig_s\frac{\lambda^a}{2}A_\mu^a)\psi - \sum_q m\bar{\psi}\psi \quad (1.1)$$

where $F_{\mu\nu}^a$ represents the gluon field strength tensor:

$$F_{\mu\nu}^{(a)} = \partial_\mu A_\nu^a - \partial_\nu A_\mu^a + g_s f_{abc} A_\mu^b A_\nu^c \quad (1.2)$$

ψ correspond to the fermionic field, g_s is the strength of the strong interaction, A_ν^a represent the eight gluon field with a running from 1 to 8 (kind of gluons), q for a quark flavor, λ_a are the eight SU(3) group generator, the γ^μ are the Dirac γ -matrices, the f_{abc} are the structure constant of the SU(3) group.

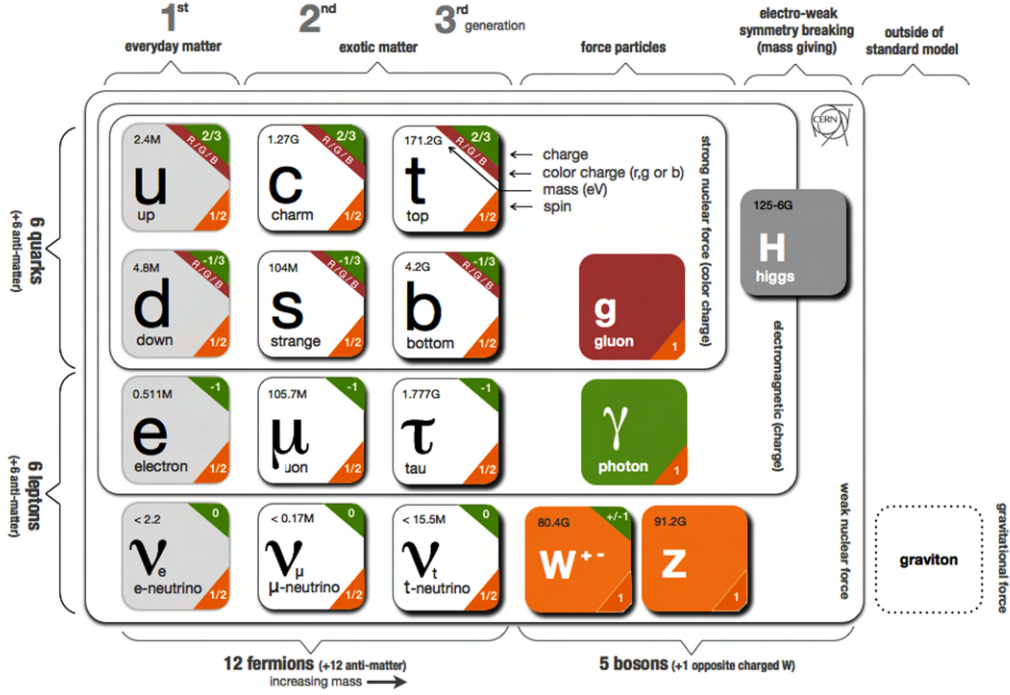


Figure 1.2: The Standard model particle classification. Image obtained from [9]

1.1.2 QCD Phases

In this world we are part of, the partons (quarks and gluons) are confined in protons and neutrons, and which are color-singlets (color neutral). The confinement is a consequence of the large strong coupling constant (α_s); this value depends on the momentum transfer as expressed in the following equation [10],

$$\alpha_s(Q^2) = \frac{12\pi}{(11n - 2N_f) \ln \frac{Q^2}{\Lambda_{QCD}^2}} \quad (1.3)$$

where n is the number of colors, N_f is the number of quark flavors, Q^2 is the momentum transfer in the process, and Λ_{QCD} is the limit of the perturbative approach. At a considerable distance (Fermi distance: $1 \text{ fm} = 1 \times 10^{-15} \text{ m}$), the α_s value is large (small momentum transfer); in contrast, at a small distance, the α_s is low (high momentum

transfer), which is known as asymptotic freedom, as shown in Fig 1.3. Consequently, the quarks are deconfined and can move freely.

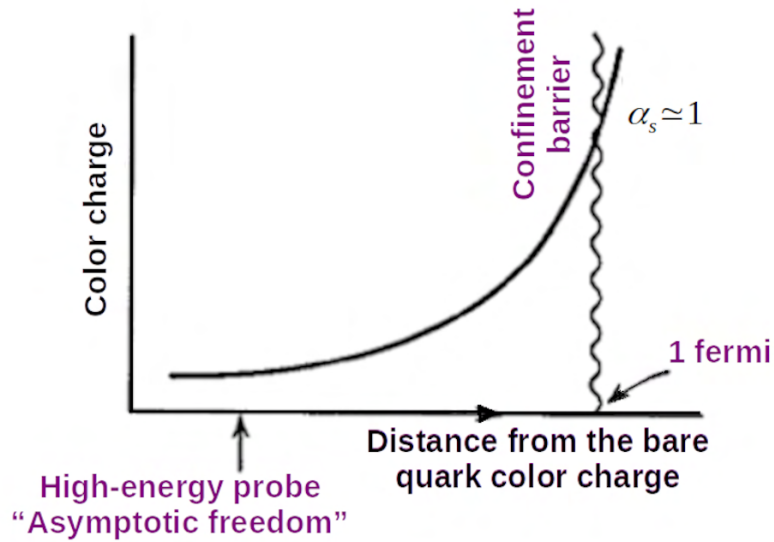


Figure 1.3: Representation of the change in the strength of the strong constant with respect to quark distance. Image obtained from [12]

Both confinement and deconfinement can be considered as different states of hadron matter. This change of state is analyzed from variations in the energy density. The energy density inside the nucleon is about $\varepsilon \simeq 0.13 \text{ GeV}/\text{fm}^3$. Increasing the temperature gives a chance to create new particles, therefore, an increment in the energy density. When ε exceeds $1 \text{ GeV}/\text{fm}^3$ partons are deconfined. A transition between confined and deconfined is shown in the Fig. 1.4 ε/T^4 vs T/T_c , where T_c is the critical temperature at which both states become indistinguishable from one another.

Also, confined and deconfined partons can be established as two different QCD phases: *hadronic matter*, in case partons are confined, and *Quark Gluon Plasma* when, partons can move freely. In fact, the QGP can be established by its energy density, baryon number density, and volume. One important aspect of confined and deconfined states is that, the phase transition limits them. The QCD phase diagram can express the phase transition

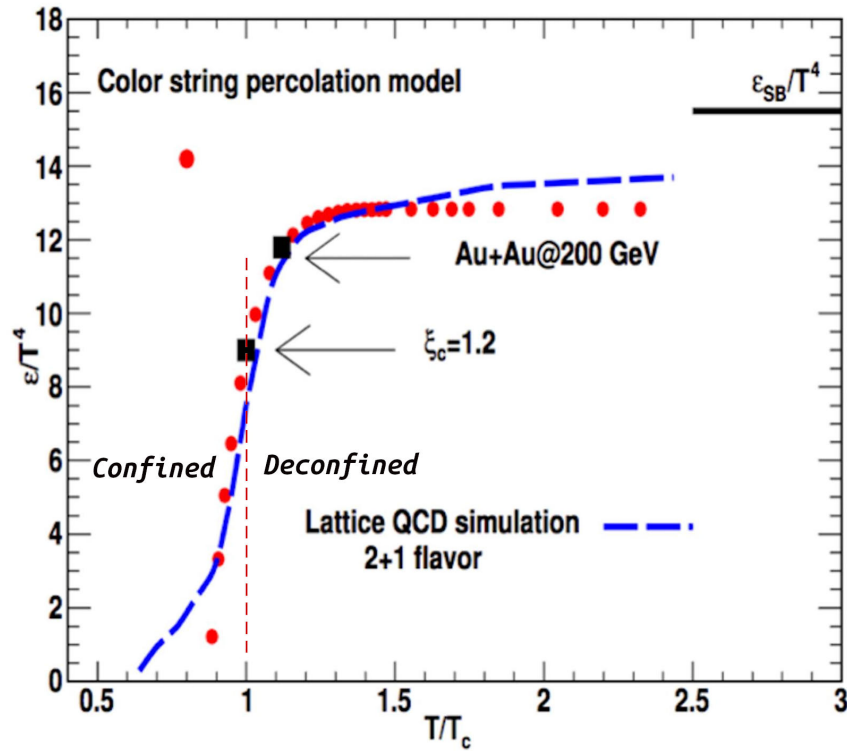


Figure 1.4: Representation of transition from confined to deconfined state according to lattice QCD, from energy density scaled by T^4 vs T/T_c . Image obtained from [13].

as shown in the Fig.1.5. This phase diagram is represented through the relation between temperature and chemical potential. This is because the nuclear behavior is expressed according to its temperature and the baryon-chemical potential (μ_B) or baryon-number density. In the transition phase from deconfined to confined state, the chiral symmetry is broken, and an order parameter associated with this is the chiral condensate [14].

In this picture of the QCD phases, the origin of the coordinates represents the vacuum. The low black point corresponds to ordinary nuclear matter and is located at temperatures around 10^{10} K (~ 1 MeV) and chemical potential $\mu_B \sim 1$ GeV (nuclear density or baryonic density $n_B = 0.14/fm^3$). From this point, increasing the temperature or compressing the nuclear matter must change the state of matter.

Maintaining at low temperatures and enhancing the baryonic density to high values result in a phenomenon similar to the core of neutron stars, which originated from grav-

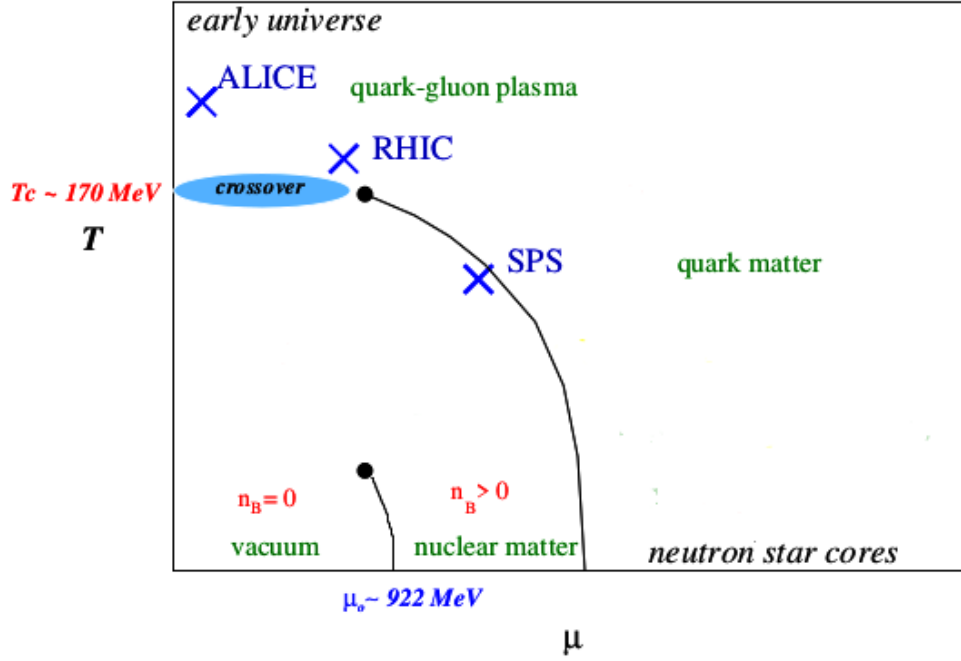


Figure 1.5: Schematic representation of QGP phase, Temperature vs chemical potential. Image obtained from [15].

izational collapse [16]. The QGP state can be achieved by increasing temperature and chemical potential to undergo a phase transition from the hadron gas to the unbound state quarks and gluons. This change in the state is known as the first-order transition, as shown in Fig. 1.5 by the curve under the critical point. On the other hand, at high temperatures and low chemical potential ($\mu = 0$), the QGP is formed under the crossover which limits with the critical point.

As we mentioned, in a confined state (α_s large), the QCD cannot be explained by perturbative theory (as Feynman Diagrams) at low energies ($E \ll 1$ GeV). however, phenomenological models can be applied, for example, the lattice QCD. In the case of asymptotic freedom, the QCD can be studied by perturbative theory. This allows experimental tests of QCD through high energy processes [10].

1.1.3 Lattice

QCD can explain the strong interaction, for example, the variation in the constant coupling value (α_s), the hadron masses, the hadron structures, etc. [10]. However, when the strong coupling constant takes large values (hadronic matter), the perturbation theory is useless for predicting the strong interaction. For this reason, many alternative hadronic models have been designed. One of the models is the lattice QCD calculation. The lattice QCD is a complex non-perturbative method to solve QCD equations. Based on the discretization of space-time on finite numbers of points. The lattice has become an essential tool thanks to computational progress in software and hardware. For example, it provided precise values of α_s , hadron masses, and critical temperature ($T_c = 170 MeV$) [17].

1.1.4 Heavy ion collisions

A heavy ion collider at relativistic energy creates a medium that achieves high temperature and energy density. This medium shows a collective behavior of hot and dense strongly interacting matter called QGP, which behaves almost like a perfect fluid (gas of quarks and gluons). For these characteristics, heavy ion collision is an excellent tool to study QGP formation, and this technique has been used since the eighties. Simulations and theoretical results are contrasted with experimental data to improve our knowledge of high energy physics. In most cases the identification of experimental observables and the experimental setup are very complex. In the high energy field, the unique experimental method for studying characteristics of the QGP formation is made by heavy ion collisions such as RHIC [1] [2] and LHC [3]. These collisions guarantee the scenario to create the QGP at high temperatures and low baryon densities with an energy density greater than $1 \text{ GeV}/\text{fm}^3$ [18]. The space and time where the QGP is created must be large enough to manage the system with macroscopic variables under thermal equilibrium. In the case of spatial extension, it should be greater than the strong interaction scale ($\sim 1 \text{ fm}$). Also the expected time duration of the QGP should be ($\sim 10^{-23} \text{ s}$) $\tau \gg 1 \text{ fm} / c$.

The Glauber Model

Some models were developed to understand the process involved in the QGP creating through ions collision; one of these models was proposed by Roy Glauber. Based on the geometrical configuration, this model evaluates geometric quantities, which can not be directly measured such as the impact parameter b (distance between the center of two nuclei in the transverse plane of the collision) as shown in Fig. 1.6, the number of nucleons participating (N_{part}) that represents nucleons that have been impacted, and the number of binary nucleon-nucleon collisions (N_{coll}) [20] shown in Fig. 1.7.

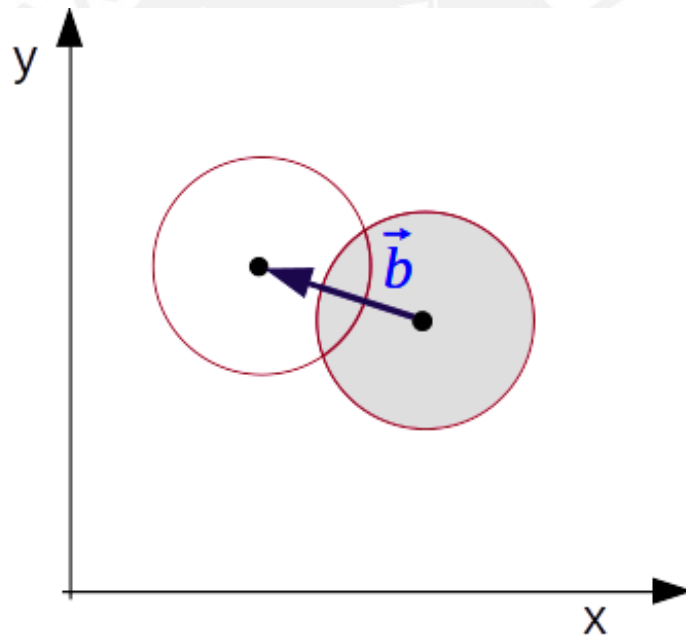


Figure 1.6: Representation of vector impact parameter on the transverse side.

The impact parameter is related to the centrality of the collision in two different situations. *Central collision*: When the impact parameter is small, many collisions between nucleons occur, or an immense N_{part} occur. *Peripheral collision*: The case when b is large, and few nucleons are involved in the collision or few N_{part} .

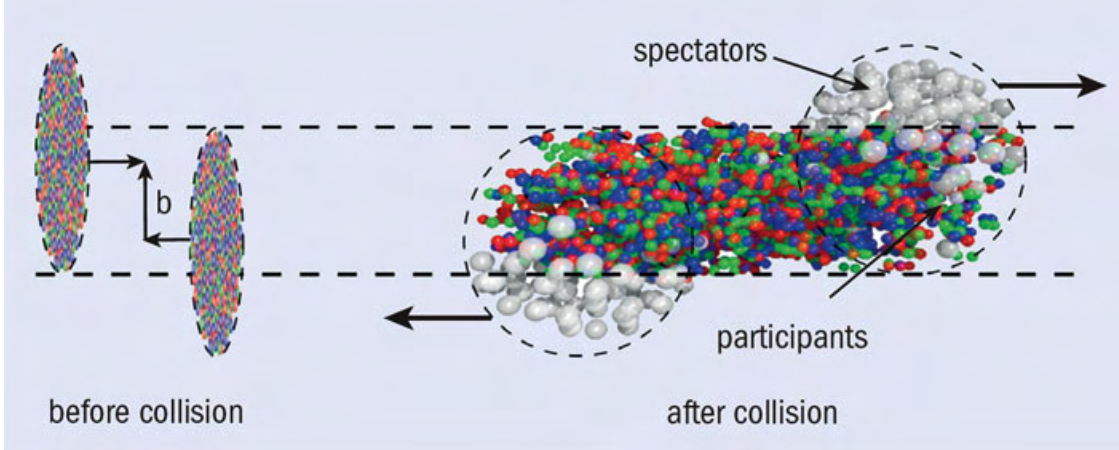


Figure 1.7: Schematic representation number of participant and spectator. Image obtained from [21].

1.1.5 Space-time evolution of the ion collision

This space-time can be divided into stages. First, before the collision, the two nuclei can be considered as two thin disks according to the effect of the Lorentz contraction. The following stages start at a collision time $= \tau_0$ s, and all the energy is concentrated in the central region; this time is known as pre-equilibrium. Then, in the next stage, for a time $t < 0.1 - 0.3$ fm/c, it is considered the time formation of the QGP; this stage is called Thermalization. The next step is hadronization which starts at a lower temperature of T_{cr} , and quarks and gluons begin to return to a confined state. In the chemical freeze-out, the inelastic interactions stopped, and the relative hadron abundances are fixed. Finally, the kinetic freeze out, where no more elastic interaction occurs [22]. All these stages can be summarized in Fig. 1.8.

1.1.6 Signature or observables of QGP

The QGP cannot be measured and observed directly due to its short lifetime [23]. However, indirect observables should give us information about the QGP formation. These observables are:

Particle multiplicity

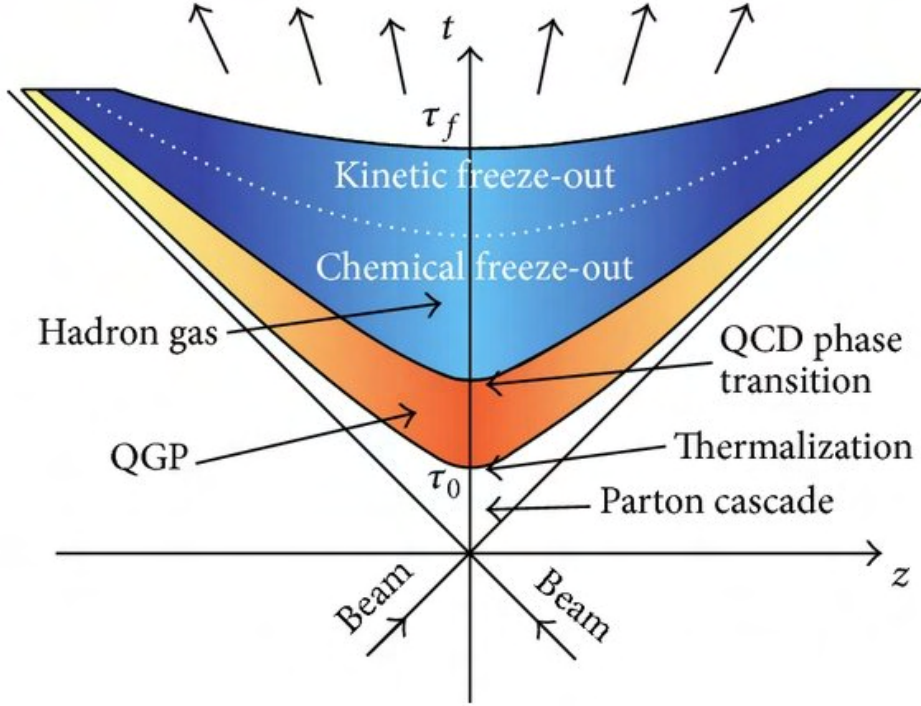


Figure 1.8: Schematic representation space-time evolution of the heavy ion collisions. Image obtained from [22].

The particle multiplicity is a tool to estimate the energy density of the QGP. Bjorken proposed an equation [24] to calculate the energy density achieved in the QGP from the transverse energy density in rapidity.

$$\varepsilon = \frac{1}{\tau_0 A} \frac{dE_T}{dy} \quad (1.4)$$

Where τ_0 is the formation time for the QGP, A is the transverse area in the collision (related to the centrality; small area for peripheral collisions), E_T is the transverse energy, and y is the rapidity.

The multiplicity can be characterized by the rapidity and the pseudo-rapidity density distributions of primary charged particles. The rapidity and the pseudo-rapidity (η) give information on emitted particles. The pseudo-rapidity is expressed by the polar angle θ with respect to the axis beam from the interaction vertex. The pseudo-rapidity is given

by:

$$\eta = -\ln\left(\tan\frac{\theta}{2}\right) = \frac{1}{2}\ln\left(\frac{|p|+p_z}{|p|-p_z}\right) \quad (1.5)$$

where p is the total momentum and p_z is the longitudinal momentum of the emitted particle.

The rapidity is expressed as:

$$y = \frac{1}{2}\ln\left(\tan\frac{E+p_z}{E-p_z}\right) \quad (1.6)$$

where E represents the total energy of the emitted particle. For simplicity, it is convenient to measure the pseudo-rapidity, because it only needs angular information instead of particle identification as is the case for the rapidity [25]. At mid-rapidity, the energy density was evaluated after primary interaction in ALICE, and a result $\varepsilon \sim 16 \text{ GeV}/\text{fm}^3$ showed evidence in the formation of QGP [18].

Photons

The photons produced in the ion collisions are classified according to their source as direct and decay photons. The *direct photons* are subdivided into *prompt photons* and *thermal photons*. The prompt photons are created in the collision of incoming partons and on the parton fragmentation. Their multiplicity is directly related with the number of binary collisions. The thermal photons $q\bar{q} \rightarrow \gamma g$ (annihilation) and $gq \rightarrow \gamma q$ (Compton scattering) are irradiated from the QGP according to the Maxwell-Boltzmann exponential rate [19]. The number of photons emitted per unit time per unit volume is called photon emission rate. The decay photons are produced at the secondary vertices, for example, $\pi^0 \rightarrow \gamma + \gamma$. The P_T spectra is used to distinguish the source of photons. Prompt photons' momentum is greater than thermal photons' momentum, and decay photons carry the lowest momentum [26].

Nuclear modification factor

The nuclear modification factor (R_{AA}) is an observable to compare the heavy-ion collisions with pp collisions. In Pb–Pb collisions there is a suppression of high- p_T particles with

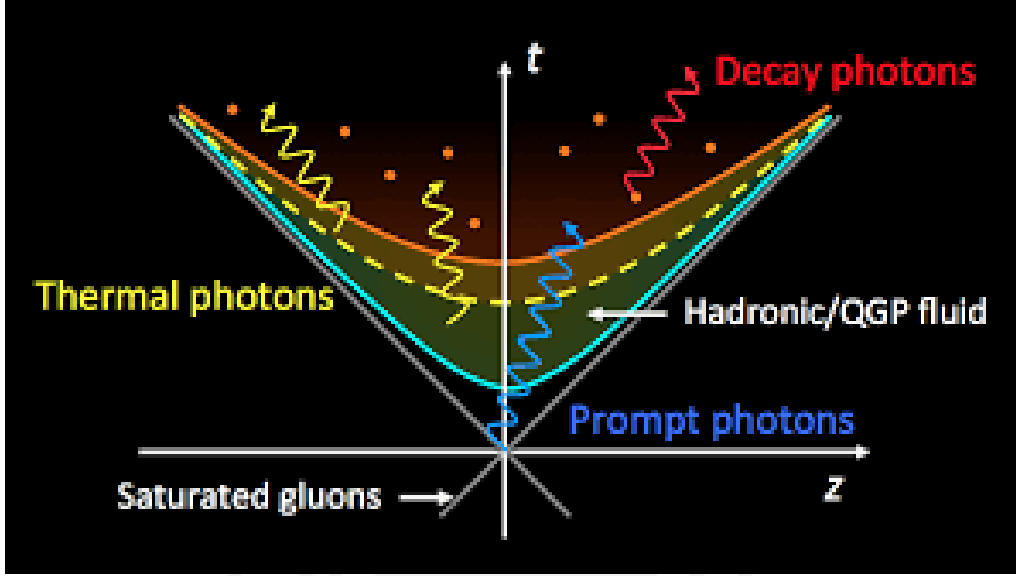


Figure 1.9: Schematic representation of different photons created in each step after ions collision. Image obtained from [27].

respect to the number of hadrons expected. It is given by [28]:

$$R_{AA} = \frac{d^2 N_{AA}/dydp_T}{\langle T_{AA} \rangle d^2 \sigma_{pp}^{INEL}/dydp_T} \quad (1.7)$$

where N_{AA} is the particle yield in Pb-Pb collisions, σ_{pp}^{INEL} is the inelastic cross-section for pp collisions and the $\langle T_{AA} \rangle$ is the nuclear overlap function ($\langle T_{AA} \rangle = \langle N_{coll} \rangle / \sigma_{pp}^{INEL}$) and N_{coll} represents the number of binary collisions between nucleons, which can be obtained by the Glauber model [20]. When the QGP is created, R_{AA} is different from one.

Charmonium suppression

The charmonium is a bound state of a quark c , and an antiquark \bar{c} referred to J/ψ meson and its excited states ($\Psi(2S)$ and $\Psi(3S)$). Charmonium suppression was proposed as a probe of the QGP formation [29]. In a deconfined state, the color charge affects the interaction between c and \bar{c} by screening, as shown in Fig. 1.10. Also, the recombination mechanism was proposed as a probe of asymptotic freedom, where the displacement of charm quarks over significant distances would be a clear signal for the presence of a deconfined parton [30].

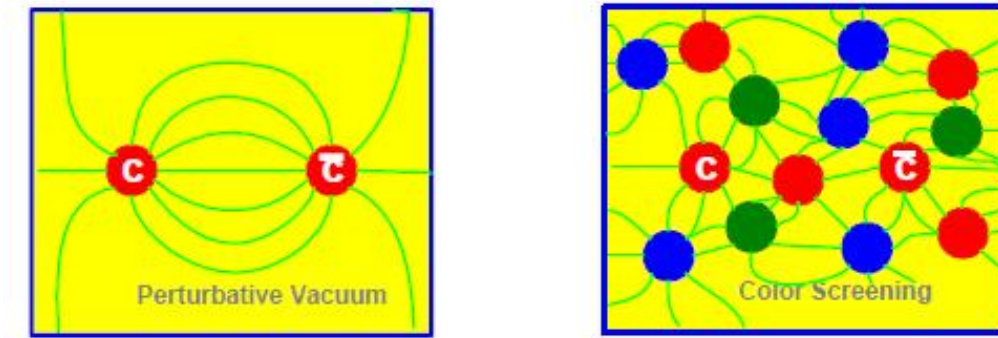


Figure 1.10: Charmonium state in QGP. At left, charmonium formed without the presence of other quarks and gluons, and at right, charmonium formation is screened by free quarks and gluons. Image obtained from [19].

According to experimental results, charmonium suppression can be described with the Cornell potential model [31].

$$V(r) = -\frac{\alpha_s}{r} + kr \quad (1.8)$$

where α_s and k are phenomenological constants of the model, the first term $-\alpha_s/r$ is like the Coulomb potential, and the second term is associated with confinement. In a deconfined state, the color attraction between q and \bar{q} is screened by deconfined quarks and gluons; also, the confining term is vanished. The Yukawa potential describes the q and \bar{q} bound as the following equation:

$$V(r) = -\frac{\alpha}{r} e^{-r/\lambda_D} \quad (1.9)$$

where λ_D is the Debye screening length, related to the maximum distance between two quarks convenient to form a bound state.

The charmonium suppression is related to the charmonium potential which is screened by the deconfined medium and the inelastic scatterings dissociate the charmonium-bound states with neighboring [29]. Many experiments and detectors studied the QGP, for example, the SPS at CERN, RICH at BNL, and ALICE for Runs 1 and 2. In the next section, we are going to describe more about it.

1.1.7 Elliptic Flow

In no-central collisions, a higher pressure gradient along the direction of the collisions is generated. From this gradient an anisotropic momentum distribution on the transverse plane can be obtained. The impact parameter induces an ideal line direction in the transverse plane, and the reaction plane (Ψ_P) is formed with the ideal line (impact parameter) with the Z axes as is shown in Fig 1.11. This anisotropy is obtained by the coefficients of the Fourier expansion of the final state particle distribution in the azimuthal angles relative to a reaction plane Ψ_P [32].

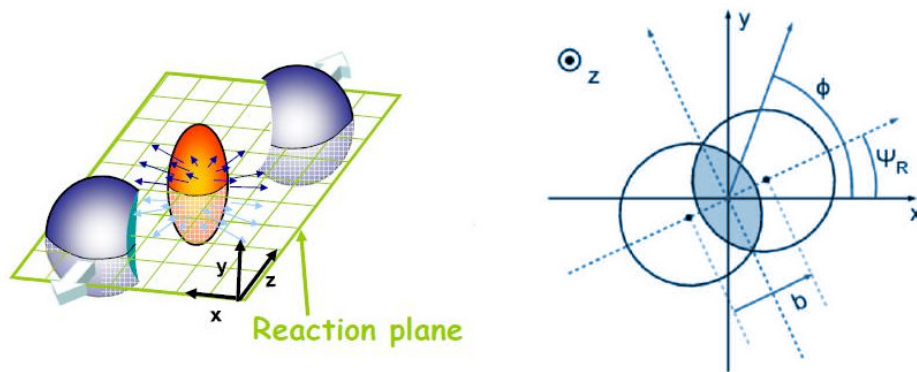


Figure 1.11: Anisotropic flow representation in the transverse plane. Image obtained from [19]

$$\frac{dN}{d(\phi - \Psi_{RP})} = \frac{N_0}{2\pi} (1 + 2v_1 \cos(\phi - \Psi_P) + 2v_2 \cos(2(\phi - \Psi_P)) + \dots) \quad (1.10)$$

The first harmonic coefficient, v_1 is called directed flow, and v_2 the second harmonic coefficient, is called elliptic flow $v_2(y, p_T)$. This v_2 represent the elliptic distribution of particles in the transverse plane [19]. If $v_1 \neq 0$ and $v_2 = 0$, it is called direct flow. On the other hand, $v_1 = 0$ and $v_2 \neq 0$, it is called the elliptic flow.

1.2 The ALICE experiment

The Large Hadron Collider (LHC) covers a 26.7 km long circular tunnel underground built at the border between France and Switzerland [33]. It is currently the highest energy particle collider, in which the collisions of beams take place at four different points on the ring, one experiment in each point (as ALICE, ATLAS, CMS and LHCb) as shown in Fig. 1.12. The LHC is designed to accelerate protons (p) and lead ions (isotope Pb-208) to achieve a center-of-mass energy $\sqrt{s} = 14$ TeV for pp collision and $\sqrt{s_{NN}} = 5.52$ TeV for Pb-Pb collision [34]. Additionally, the Xe-Xe collision was planned.

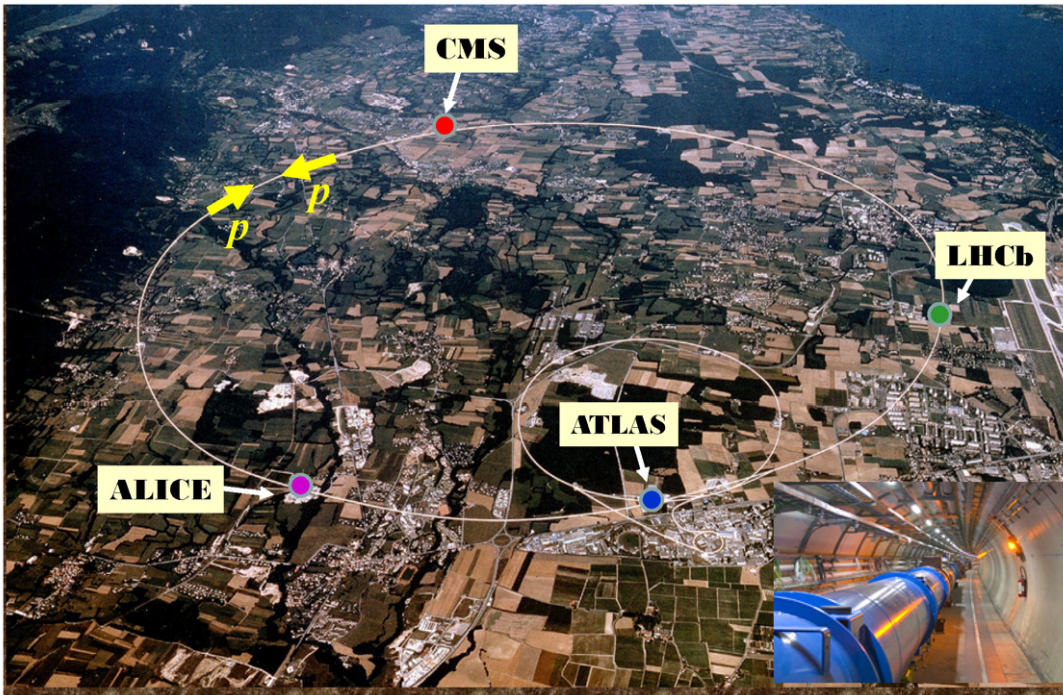


Figure 1.12: Schematic view of the Large Hadron Collider and the four major experiments. Image obtained from [35].

At point two of the LHC is located the ALICE experiment, and we describe it in the next section.

ALICE is an experiment focused on the study of heavy-ion collision [36]. ALICE is one of the four major experiments of the Large Hadron Collider (LHC).

After finishing the Run 2 in 2018, the level of the center-of-mass energy planned was

not achieved. It only reached $\sqrt{s} = 13$ TeV for pp, $\sqrt{s_{NN}} = 8.16$ TeV for p-Pb, and $\sqrt{s_{NN}} = 5.02$ TeV for Pb-Pb collisions. In the case of Xe-Xe, it achieved $\sqrt{s_{NN}} = 5.44$ TeV [4].

In 2019 and 2020, the LHC took a scheduled prolonged shutdown and technical stop to prepare for the Run 3, which started operations in mid-2021. For Run 3 and 4, LHC plans to increase the instantaneous luminosity (\mathcal{L}) to $\mathcal{L}_{pp} = 2 \times 10^{34} \text{cm}^{-2} \text{s}^{-1}$ and $\mathcal{L}_{PbPb} = 6 \times 10^{27} \text{cm}^{-2} \text{s}^{-1}$. This high \mathcal{L} conduces the Pb-Pb interaction rate at 50 kHz. The centre of mass energy for pp could increase up to 13.6 TeV and 5.44 TeV for Pb-Pb [37].

1.2.1 ALICE detector

ALICE focus on the study of heavy-ion physics by tracking particles of very high multiplicity events generated in the ion-ion collision with a precise particle identification system. It was designed to investigate the strongly interacting matter at extreme energy densities by experimental observables, which are related to the QGP formation such as was mentioned before in the section 1.1.6.

ALICE dimensions are $16 \times 16 \times 26 \text{ m}^3$ with a total weight of $\sim 10000 \text{ t}$ [36]. According to its position and functionality, the ALICE detector is divided into two parts: the central barrel and the muon arm. The global reference framework establishes the positive z-axis is parallel to the beam with opposite direction of the muon arm. The central barrel can detect from 45° to 135° in polar angles and covers the full azimuth, and it is surrounded by a large solenoid magnet generating an intense magnetic field of 0.5 T on parallel directions to the beam axis.

The detectors of the central barrel can track and identify particles according to their mass and particle type. In the central part, detectors from the inner part to the outer part are: the Inner Tracking System (ITS), a cylindrical Time-Projection Chamber (TPC) which is the main tracking detector. The three particle identification systems are: the

Time-of-Flight (TOF), the High-Momentum Particle Identification Detector (HMPID) and the Transition Radiation Detector (TRD). Finally the two electromagnetic calorimeters (PHOS and EMCal). Fig. 1.13 shows a perpendicular view of the central barrel of the ALICE detector. The muon arm covers a pseudorapidity acceptance between $-2.5 < \eta < -4.0$. The detectors which are part of ALICE are shown in Fig. 1.14 [36].

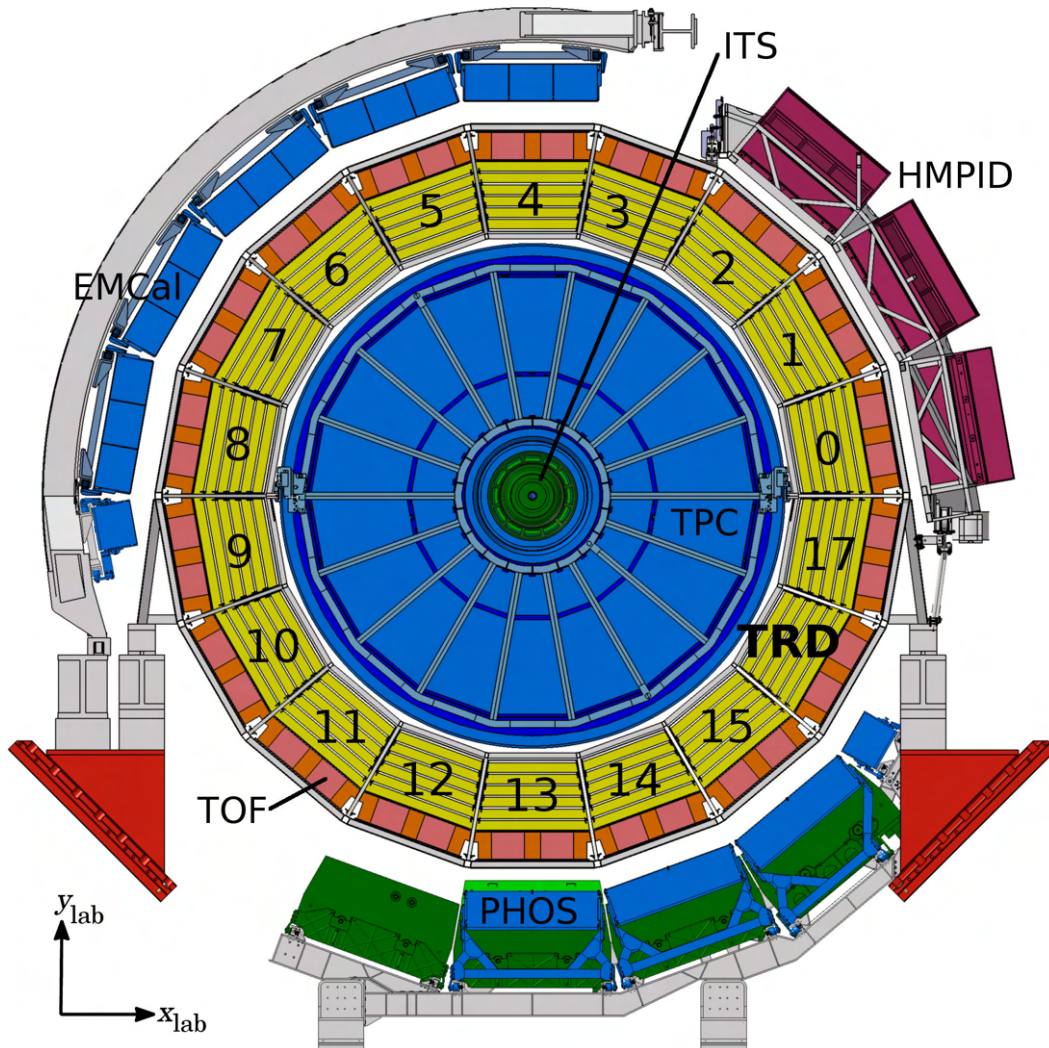


Figure 1.13: Perpendicular view of detectors on ALICE. Image obtained from [38].

To have the capability to manage the high multiplicity originated at high instantaneous luminosity for the Run 3, the ALICE experiment has planned the installation of an upgraded experimental apparatus to improve the track and the readout of Pb-Pb inter-

actions. The Muon Forward Tracker is a new detector, which was installed on December 2021. In the next part, we will describe the main detectors of ALICE. The MFT will be described with more detail in the chapter 3.

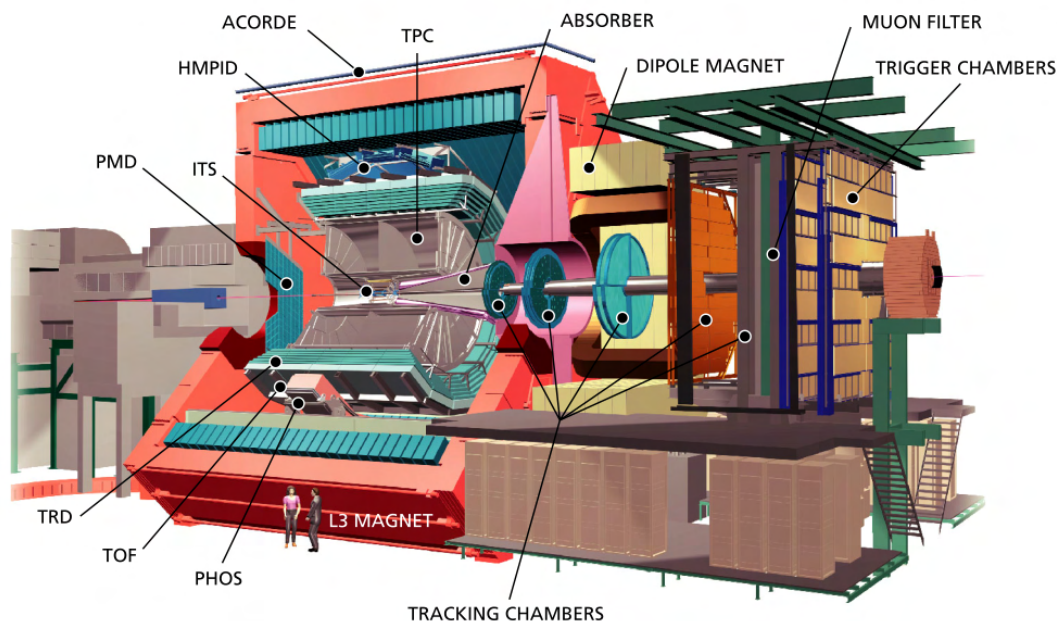


Figure 1.14: Schematic view of the ALICE detector. Image obtained from [36].

1.2.2 The Inner Tracking System

The principal functions of the ITS are: to determine the primary vertex and the track, then identify particles and secondary vertexes too. According to the ITS upgrade plan [39], it is composed of seven concentric layers instead of six, which were used for Run 2. Three layers are located in the inner barrel, two in the middle, and two layers in the outer barrel. A transverse view of the ITS is shown in Fig. 1.15. The radius of the innermost and outermost layers are 22 mm and 400 mm, respectively. The layers are azimuthally divided by staves, which are composed of an array of sensors. The staves in the inner barrel consist of 9 sensors, covering a length of 270 mm and a width of 15mm. On the other side, staves in the middle and outer barrels have a different configuration. The sensors are grouped into modules. Each module is composed of fourteen sensors, which

are distributed in two rows of seven sensors each. Modules are assembled in half-staves. For the middle layers with four modules, and seven modules in the outer layers in the row configuration. In the middle layers, the half-staves have a length of 843 mm, and in the outer half-staves, the length layer is 1475 mm [39].

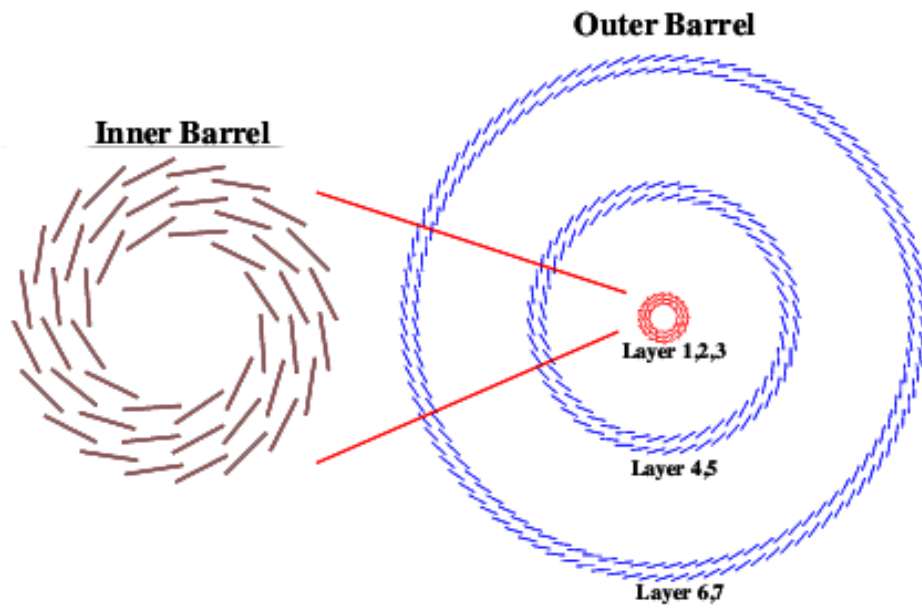


Figure 1.15: A Schematic representation of a transverse view of the seven-layer of the ITS configured in three barrels. Image obtained from [40].

The upgrade in the ITS covers an acceptance of $|\eta| < 1.22$, which was implemented with a new sensor, which is a monolithic active pixel sensor (MAPS). Each sensor is an array of pixels covering 15 mm x 30 mm. This new implementation cannot measure energy loss, only giving information of the particle crossing or not a sensor. Fig. 1.16 shows the position's stave forming the seven layers of ITS and the inner layer closer to the beam pipe. We describe the new sensor with more details in the Chapter 3.

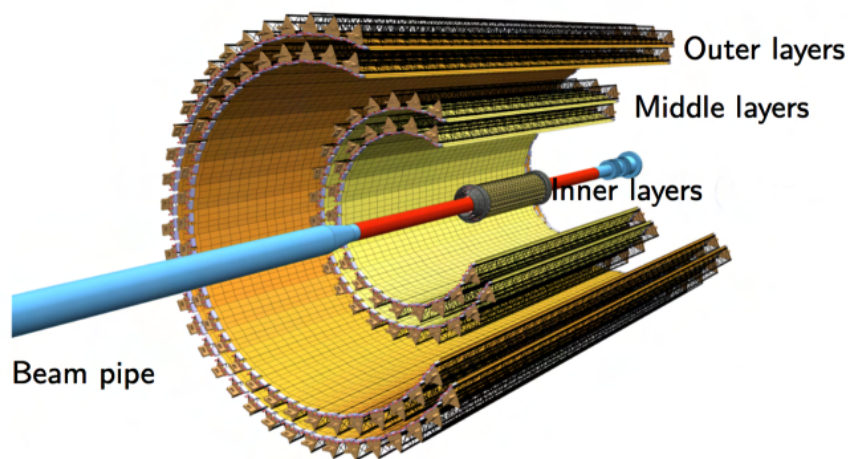


Figure 1.16: Position' stave forming the layers for the upgraded ITS. Image obtained from [39].

1.2.3 Time Projection Chamber (TPC)

The TPC is the main charged particle tracking, particle identification and vertex determination system of all the ALICE detectors [36]. The TPC is implemented as a cylindrical drift electric field cage with two readout planes located on its base, which are distributed into 18 trapezoidal sectors, as is shown in the Fig. 1.17. The active volume is within a radius of 87 cm and 247 cm, and a length of $-250 \text{ cm} < z < 250 \text{ cm}$. At $z=0 \text{ cm}$, the high voltage electrode is located, providing the electric drift field of 400 V/cm and dividing the active drift volume into two halves. The TPC is filled with a 90 m^3 gas mixture of 90% Ne and 10% CO_2 . When charged particles cross the TPC volume, they ionize the gas along their path. The electrons generated can drift by the electric field to the end plates of the cylinder for the readout process [41].

The planned upgrade of the TPC for a Pb–Pb collision, which rate can achieve up to 50 kHz, required a replacement of the Multi-Wire Pad Chamber (MWPC) readout to

Gain Electron Multiplier (GEM) detectors let continuous operation and read out. More details about can be found in [40].

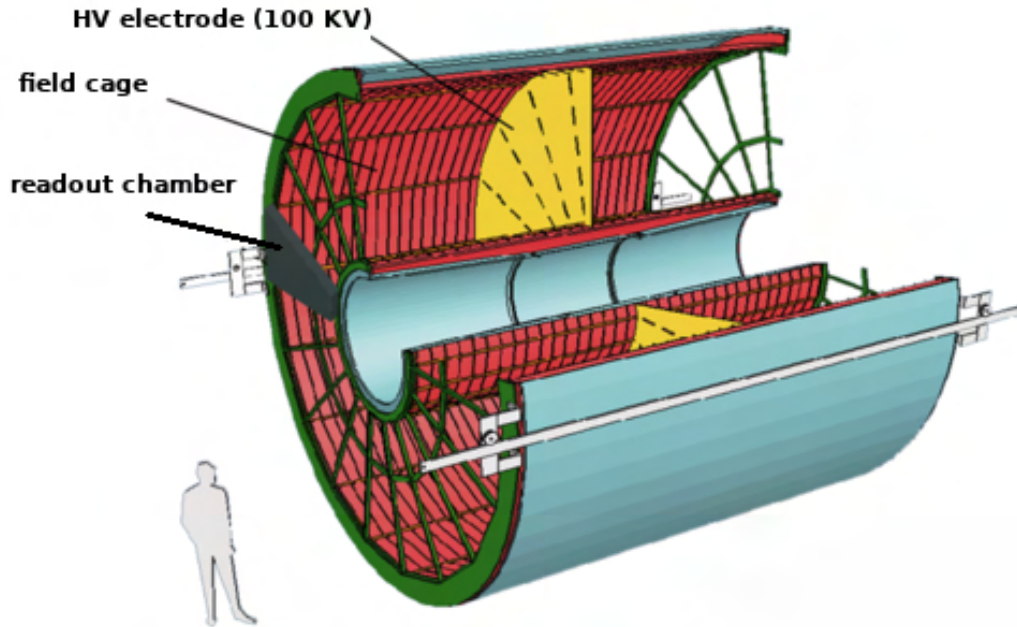


Figure 1.17: View of the TPC shape compared with a man, including the two plates segmented to readout and the electrode. Image obtained from [42].

1.2.4 Fast Interaction Trigger (FIT)

According to the ALICE upgrade, the two detectors V0 and T0, have been replaced by a single trigger detector, the Fast Interaction Trigger (FIT) [43]. The system is going to give triggers for the whole experiment. The FIT can also send information about: the beam luminosity, charged particle, vertex location, multiplicity and azimuthal distribution. The FIT will be composed of V0+ and T0+. The T0+ is organized in two (T0A+ and T0C+) arrays of modules. Each module is segmented into quartz radiators joined directly to a micro channel plate-PMT (MCP-PMT). The T0C+ array is located on side C with 28 modules at $z=-820$ mm covering $-3.3 < \eta < -2.2$. The T0A+ is located on A side with 24 modules at $z=3200$ mm and acceptance of $3.8 < \eta < 5.1$. A geometrical design of FIT is shown in Fig. 1.18.

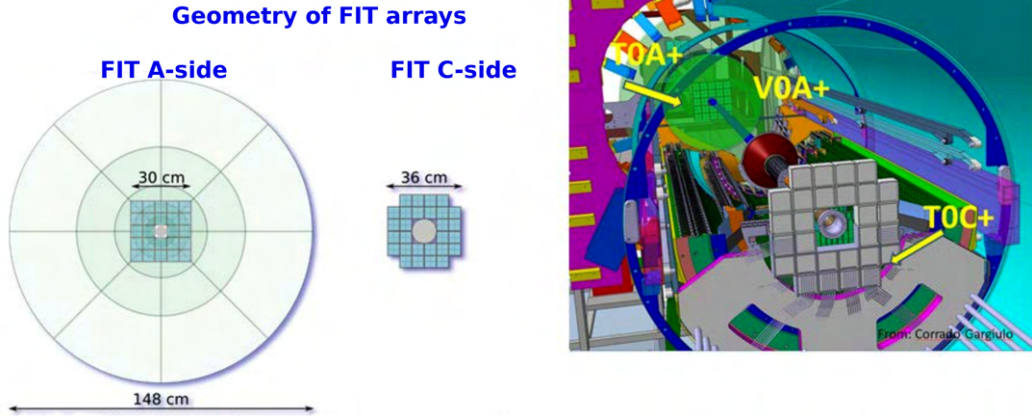


Figure 1.18: Schematic view of size and geometry of the FIT, including the location with respect to other detectors. Image obtained from [43].

The V0+ is a set of scintillators (4cm of thickness) of five rings, which are segmented into eight sections. The inner and outer diameters are 8 cm and 148 cm respectively.

The FIT detectors are going to produce the signal with a latency of 425 ns. This time is inside the range for timing readout in other detectors. For more details see [43].

1.2.5 Muon spectrometer

The muon detection helps to study the quarkonia, the heavy-quark, and vector meson production. In ALICE, the muon detection is done by the muon arm, covering $-4 < \eta < -2.5$, and is composed of five elements which are: a hadron absorber, a dipole magnet, a set of tracking stations, an iron wall, and the muon trigger system, see Fig. 1.19. All the systems permit to select di muons coming from prompt J/ψ production instead of coming from a displaced J/ψ originated by a B meson.

A hadron absorber

The absorber is made of carbon and concrete to reduce the flux of primary hadrons and low-energy electrons. It is located inside the solenoid magnet between z 0.9 m and $z=5.03$ m. This thickness corresponds to ten hadronic interaction lengths.

A muon dipole magnet

It is generated by a dipole to determine the muon momenta by tracking muons. It

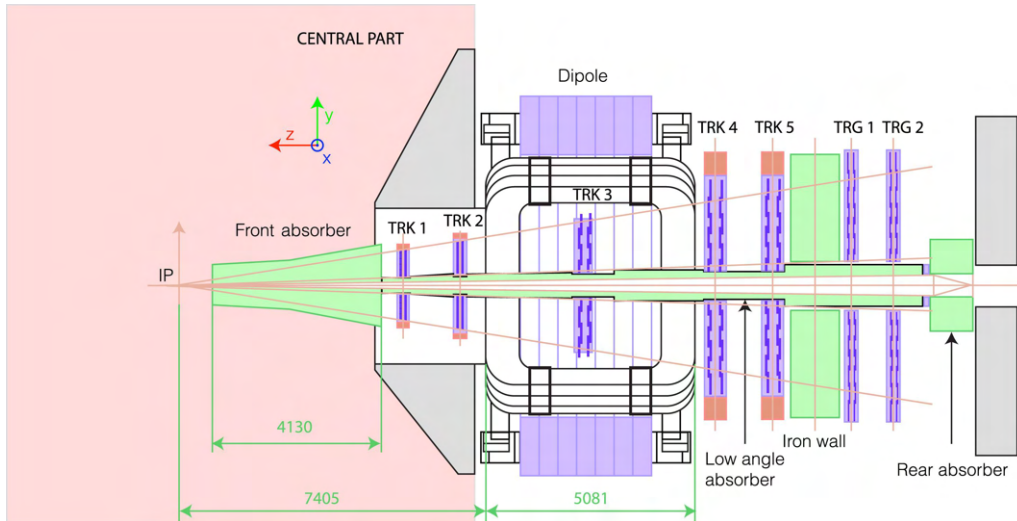


Figure 1.19: The ALICE muon spectrometer. Image obtained from [4]

generates a magnetic field of up to 0.7 T.

Tracking stations

The system is composed of five tracking stations, of which two are between the absorber and dipole, one inside and two after the dipole. Each station carries two cathode pad chambers, which are designed to achieve a spatial resolution of about $100 \mu\text{m}$. The thickness of the chamber is below 3% radiation lengths to avoid multiple scattering and degradation of spatial resolution.

The iron wall

This block absorbs residual secondary hadrons like pions and low momentum muons by its length of 1.2 m, which corresponds to 7.2 hadronic interaction lengths. It is located behind the tracking system [44].

Muon trigger system

Its goal is to avoid low- p_t muon signals, which come from the background, like muons decay. The Muon trigger system is composed of two detector stations located at 16 m and 17 m respectively, from the interaction point. Each station is implemented with two resistive plate chambers (RPC) planes. Each plane consists of 18 RPC modules.

The existing Muon arm has given good results on vertex identification. However, the

muons suffer multi-scattering, and the location away from the IP limits the vertex precision. One new detector has been proposed to improve the primary vertex identification; this is the MFT. In the next chapter, we describe the MFT.



Chapter 2

The Muon Forward Tracker

The existing Muon Spectrometer has provided good results, but its limitations do not allow to take advantage of the full potential of muon measurements in ALICE. To improve the efficiency of the muon arm the inclusion of a new detector close to the interaction point was proposed. This is the Muon Forward Tracker [4].

The MFT is a new silicon tracker detector which has recently been installed the last December during the LHC Long Shutdown 2, for the Run 3 according to the ALICE muon physics program. MFT is designed to evaluate the medium temperature, study charmonium dissociation and recombination via measurements of prompt J/ψ and ψ' production and elliptic flow by detecting and tracking charge particles, specially muons, which will allow discrimination between the decay of the prompt and non-prompt J/ψ (from b-hadron decay) to have more information about the QGP formation. One important aspect is the increase of the signal-to-background into 5-6 factor [45].

Fig 2.1 shows the schematics standalone of the MFT. Its main goal is to improve the vertex capabilities of the muon spectrometer. The MFT is positioned between the inner barrel and the muon absorber. It is surrounded by the outer barrel as shown in Fig. 2.2. It has an acceptance of $(-3.6 < \eta < -2.45)$, covering a forward pseudorapidity region, which is not explored by any of the other detectors in LHC making the measurements unique and complementary to the mid-rapidity [46]. The heart of the MFT is the Monolithic

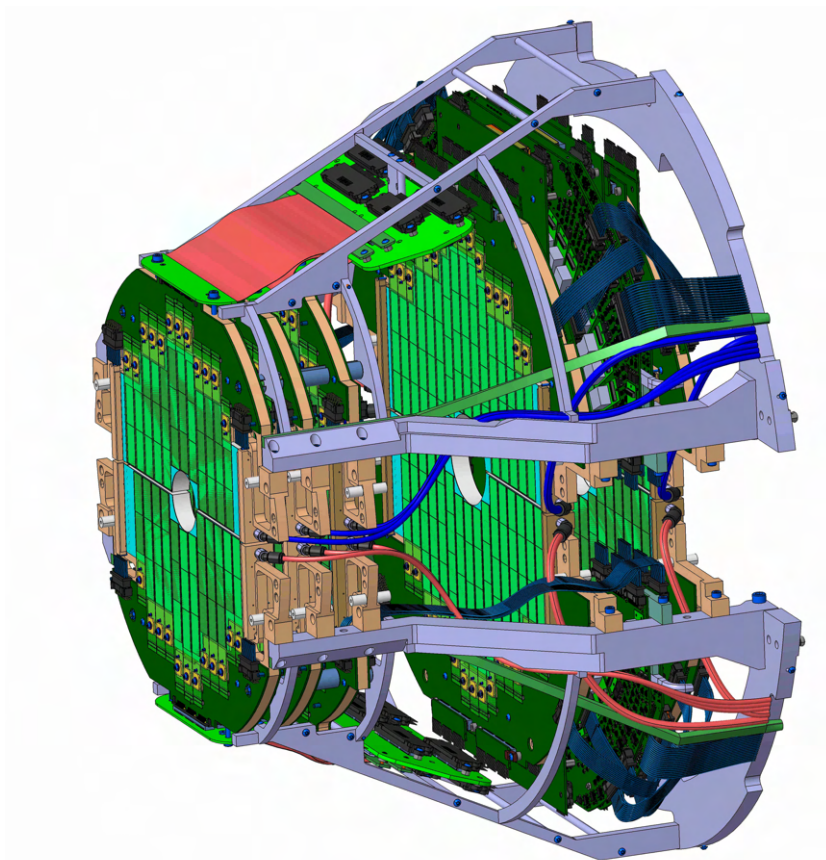


Figure 2.1: Schematic representation of the MFT detector. Image obtained from [4].

Active Pixel Sensor [4], which is the same sensor used for the ITS update, and will be described with more detail in the next chapter.

The MFT is a detector divided into two half-MFT parts surrounding the beam pipe. Each half-MFT is composed of five half-disks located along the beam axis from the interaction point at $z = -460, -493, -531, -687, -768$ mm. The half-disks are positioned over the half-cone that acts as a support. In Fig 2.3 a half-cone is shown. Each half-disk is mainly composed by ladders.

2.1 The Ladder

The ladder is a structure to carry the pixel sensors. Ladders are classified according to the number of sensors that they carry, as it is shown in Fig 2.4. The ladder is divided

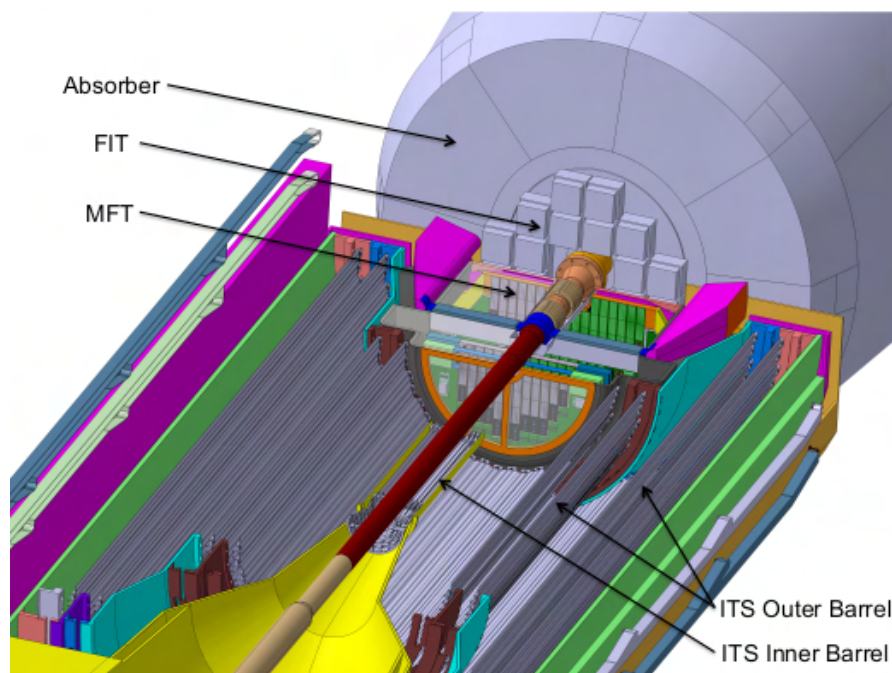


Figure 2.2: View of half-MFT located between the inner barrel and the absorber. Image obtained from [4].

into three parts: the first, is the stiffener which acts as a mechanical support and is made of carbon fiber, the second element is the silicon pixel sensor, and the last element is the Flexible Printed Circuit (FPC) which powers and controls the sensors. A junction between sensor and FPC is made by Hybrid Integrated Circuit (HIC) which is a laser-soldering [4].

2.2 The half-disk

The half-disk is divided into four elements: the ladders, Printed Circuit Board (PCB), heat exchange, and half-disk support. The ladders are glued to the half-disk. A couple of PCBs are used to power and control sensors. An equipped heat exchange works by a water cooling system and cold plates. It additionally maintains the rigidity of the ladders. The last element is the half-disk support, which carries all the components. Fig.2.5 shows the elements of a half-disk. The five half-disks are identified by their location, such as

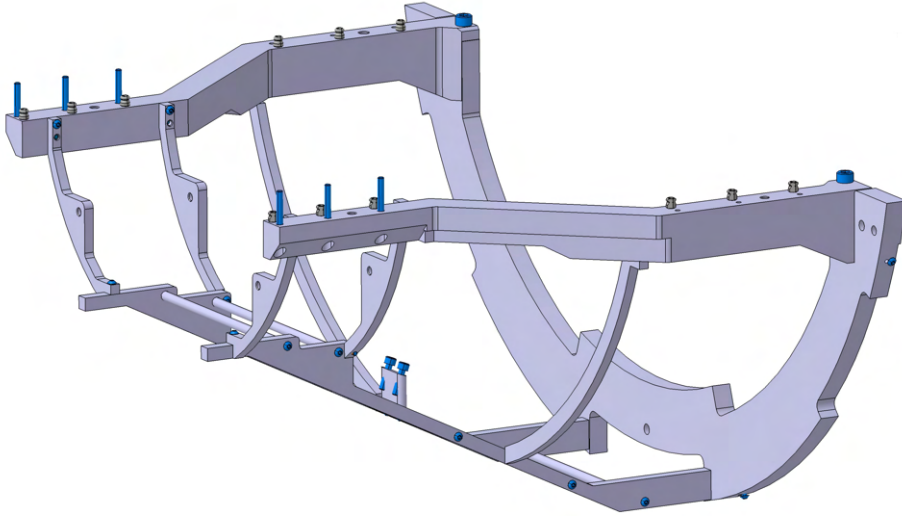


Figure 2.3: Schematic representation of the half-cone. Image obtained from [47].

half-disk-0 to half-disk-4. The half-disk-0 is close to the interaction point. All the half-disk are similar, but their radius are different, the large radius corresponds to half-disk-4, and the half-disk-0 and half-disk-1 have an equal radius.

The ladders are arranged in the shape of detection planes of sensors. Each half-disk has two detection planes that are located at the front and back of the half-disk. A ladder position, acceptance, dimension, and shape of the front of a half-disk-0 are shown in Fig 2.6. The number of sensors in each half-disk varies according to the half-disk location. The half-disk-0 and the half-disk-1 carry 64 sensors on each one, and on the other side the half-disk-2/3/4 have 76, 112, and 132 sensors, respectively. The ladder and sensor distribution in each half-disk is summarized in Table 2.1.

2.3 MFT half-barrel

The barrel is a cylindrical structure to support the MFT and also is divided into two half-barrel. It carries wires of power, input/output cables and cooling pipes (services). The half-barrel is composed of four elements: the patch panel, the inner shell, the outer shell and the wheels. A patch panel is located on the back part to distribute cables between

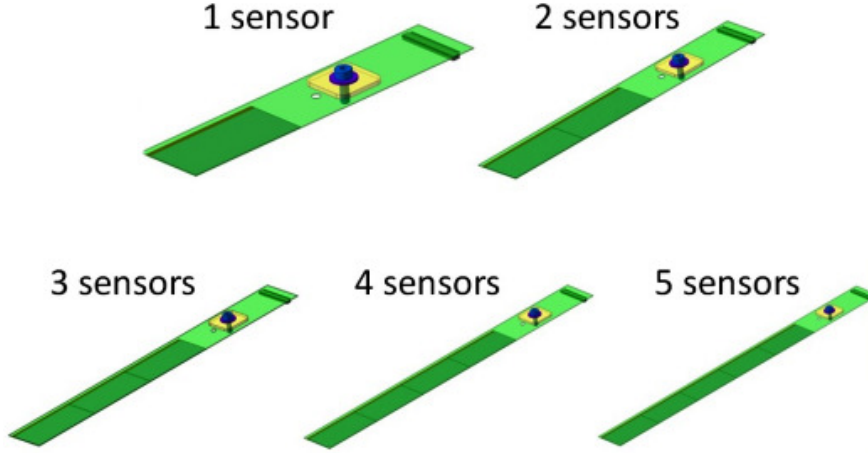


Figure 2.4: Ladders with different numbers of sensors. Image obtained from [4].

Table 2.1: Number of sensors and ladders distribution in each Half-Disk and in the full MFT [4]

Half-disk	0	1	2	3	4	Full MFT
z-position (mm)	-460	-493	-531	-687	-768	-
N sensor	64	64	76	112	132	896
n. ladders with						
1 sensor	2	2	2	2	0	16
2 sensor	4	4	4	2	4	36
3 sensor	18	18	14	6	4	120
4 sensor	0	0	6	22	18	92
5 sensor	0	0	0	0	8	16
No ladders	24	24	26	32	34	280

the inner and outsides of MFT. The inner shell with a radius 50.3 cm, this element let fix and center a patch panel. The outer shell is a conical shape to carry services to the inner barrel. And finally the wheels, which during the insertion procedure let to position and fix the half-MFT in its place. A Fig 2.7 shows the half-barrel.

2.4 Online-offline computing system

For Run 1 and Run 2, AliRoot was a software to manage the simulation, calibration, reconstruction and analysis (offline system) [48]. On the other hand, the online system

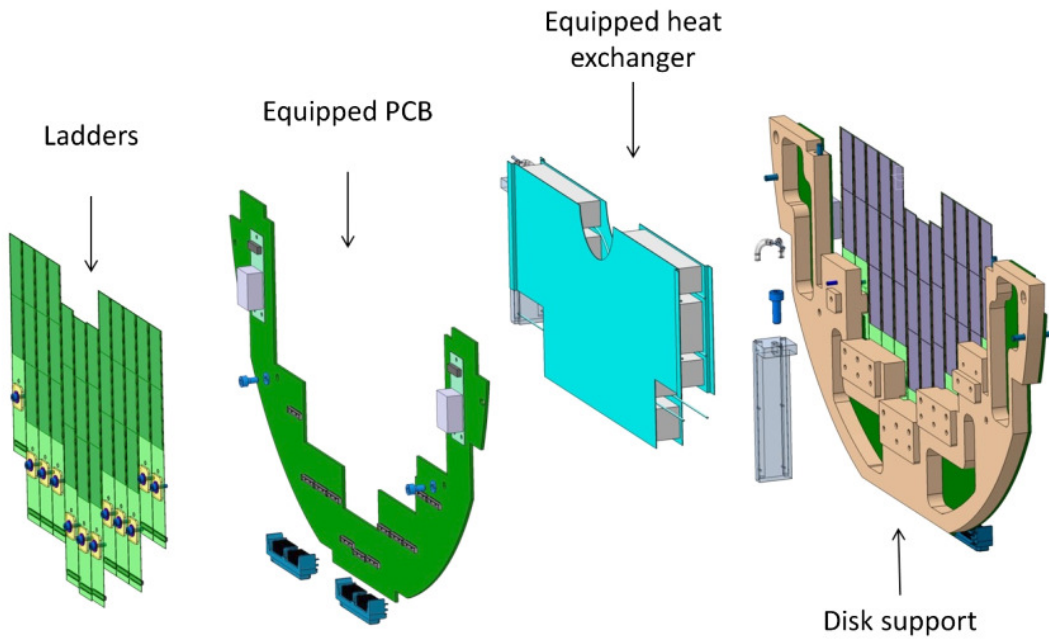


Figure 2.5: Elements of a half-disk. Image obtained from [4].

was in charge of readout, controlling, configuring and monitoring the different detectors. Both online and offline worked independently.

For Run 3 a new software has been implemented, this is the online-offline (O^2) system. It is a new software designed exclusively to perform detector calibration, data taking, reconstruction and physic's simulations for Run 3 and 4 [49]. The simulation on O^2 is based on virtual Monte Carlo, which allows running with different Monte Carlo codes.

One part of our work was the implementation of two not sensitive elements of the MFT geometry. They are the *half-cone* and the *patch-panel*, which are shown in Fig. 2.8 and Fig. 2.9. Both elements were implemented in O^2 geometry according to their blueprint and materials. The placement of both elements has to be precise to avoid overlaps with other elements of MFT.

The last version of the *half-cone* had two previous versions, and we implemented the second and the final version. The authentic physical design was in charge of Subatech [50]. A Few variations between the second and third versions are shown in Fig. 2.10.

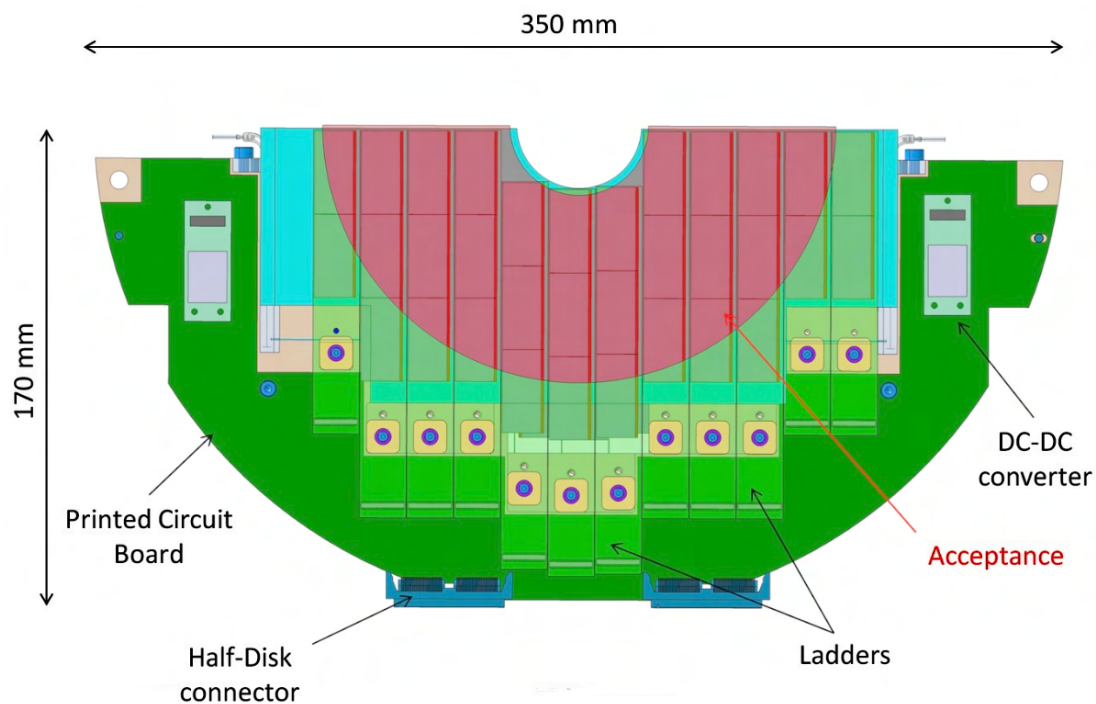


Figure 2.6: Frontal view of half-disk-0. Image obtained from [4].

The *half-cone*, *patch-panel*, and half-disks together form the main geometry part of the MFT in O^2 are shown in Fig. 2.11.

In the next chapter, we describe the pixel sensor which is used to implement the MFT and ITS detectors.

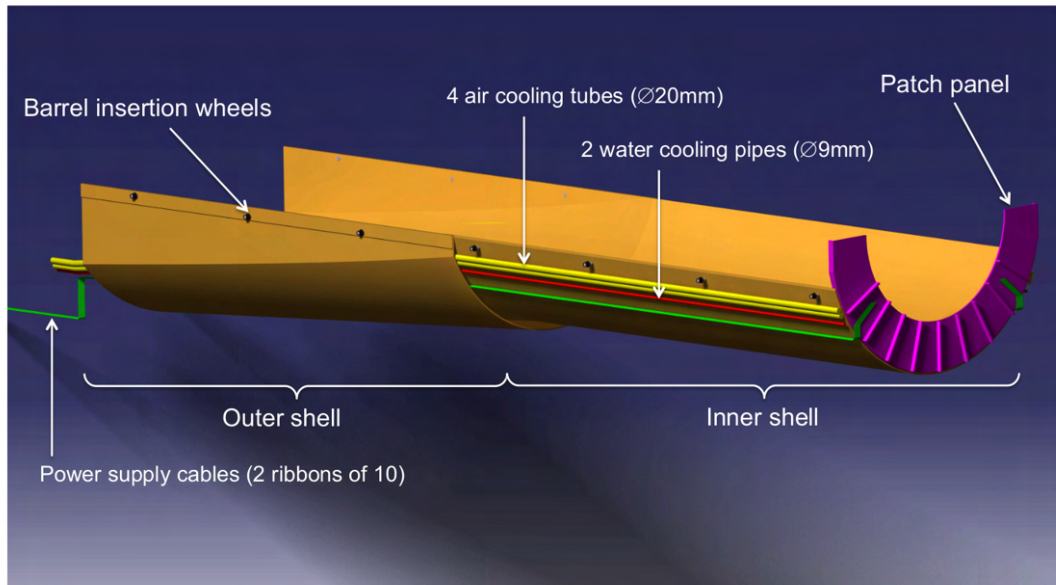


Figure 2.7: Schematic view of the half-barrel. Image obtained from [4]

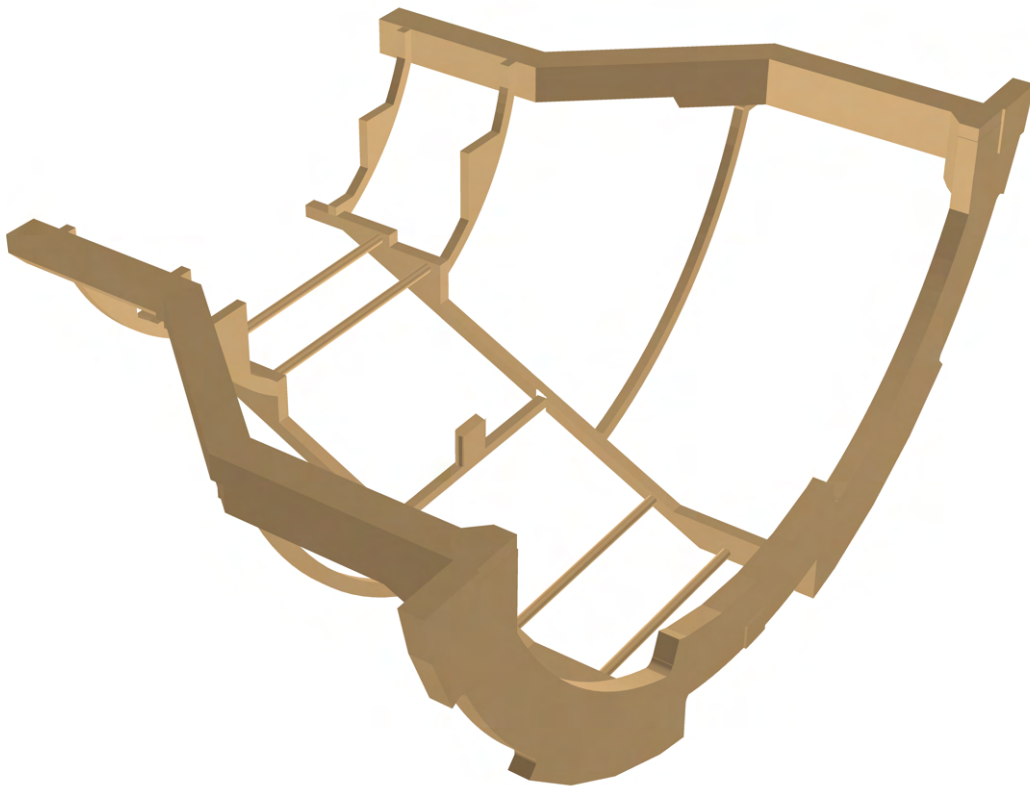


Figure 2.8: Half-cone geometry implemented in O2 geometry.

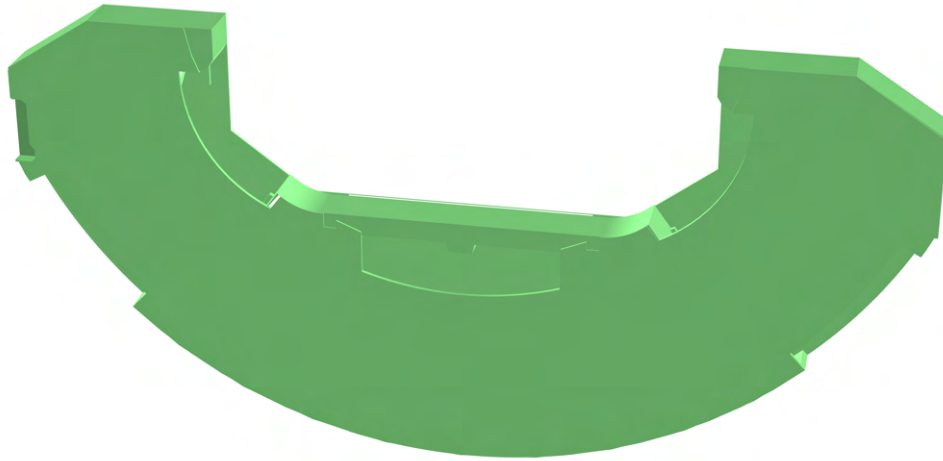


Figure 2.9: Patch-panel geometry implemented in O2 geometry.

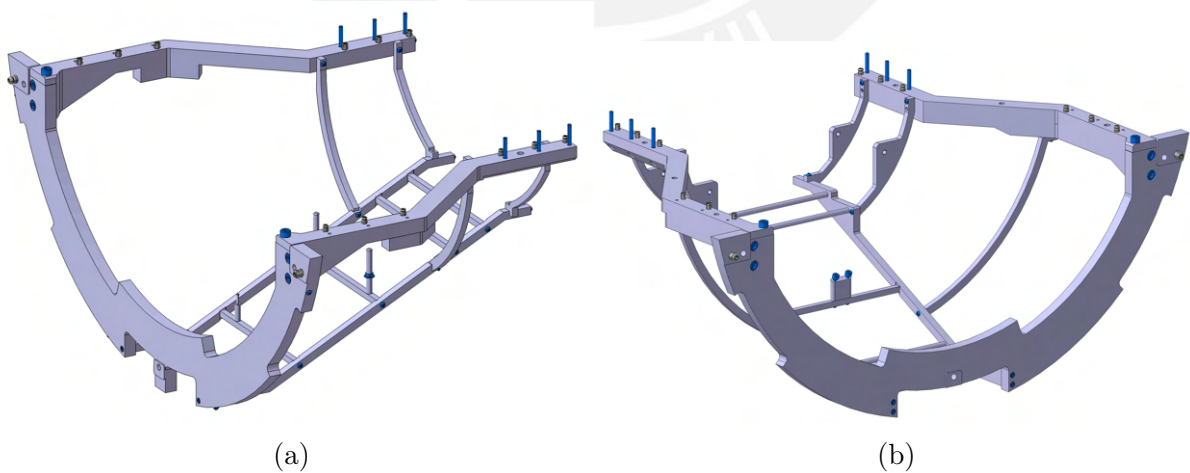


Figure 2.10: The a represent the second version and b is the final version of *half-cone*

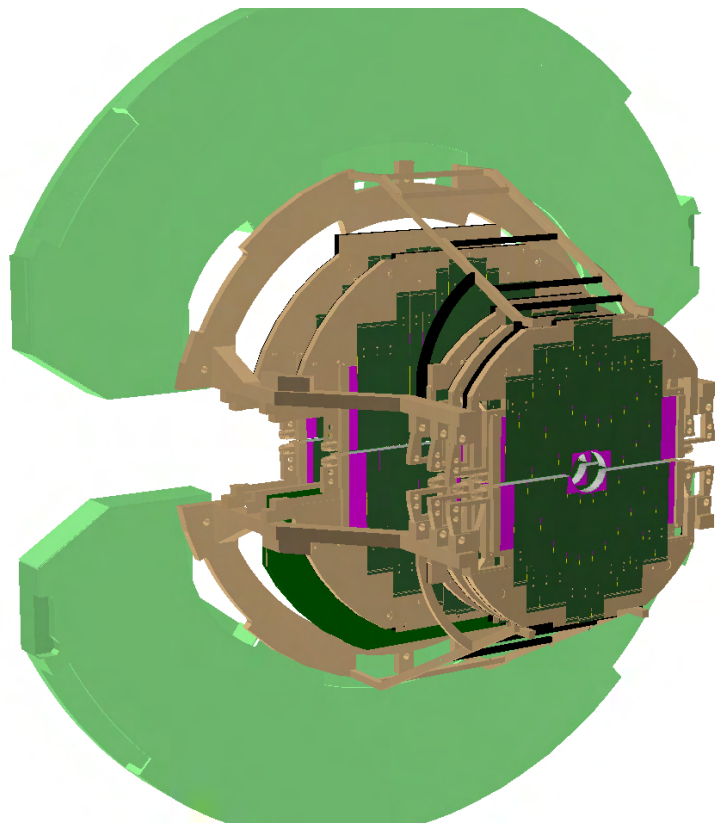


Figure 2.11: The main part of MFT geometry, which was implemented in O2 geometry.

Chapter 3

Monolithic Active Pixel Sensors

In this chapter, we focus on the physics behind silicon pixel detectors. We describe the interaction of the particles and radiation on the sensor, including the carrier generation and charge collection.

The Monolithic Active Pixel Sensor (MAPS) in the Complementary Metal Oxide Semiconductor (CMOS) was invented in the early 1990s for the detection of visible light [56]. It was used at the beginning in specific applications like webcams. Continuous progress in technology, reduction in the dark current, and improvement signal-to-noise ratio have led the CMOS sensor to become a dominant image sensing device. CMOS sensors are widely used in commercial digital cameras and scientific applications [51]. The concept underlying the use of CMOS sensors for the detection of charged particles was proposed in 2003 and demonstrated on small prototypes [51].

3.1 Charge Generation and Collection in MAPS

Semiconductor detectors are based on the detection of charged particles by interaction with a sensor. The interaction mechanism depends on the charge and energy of the particles traversing the sensor. The generation and collection charge mechanism depends on the material properties, such as the resistivity, doping level, bias configuration, and

geometry. The geometry is related with the thickness of sensitive material and pixel pitch.

3.1.1 Energy loss of charged particles

The principle of silicon detectors is based on the energy loss of traversing charged particles and radiation in the sensor. Energy loss for charged particles is due to the ionization in the material and the scattering process with electrons of the medium. The Bethe-Bloch formula describes these processes [52]:

$$-\frac{1}{\rho} \left\langle \frac{dE}{dx} \right\rangle = 4\pi N_A r_e^2 m_e c^2 z^2 \frac{Z}{A} \frac{1}{\beta} \left(\frac{1}{2} \ln \left(\frac{2m_e c^2 \beta^2 \gamma^2 T_{max}}{I^2} \right) - \beta^2 \right) \quad (3.1)$$

where:

N_A : Avogadro's number;

z : charge of the traversing particle in terms of unit charge;

Z : atomic number of the absorption medium (14 for silicon)

A : atomic mass of the absorption medium (28.08 g/mol for silicon)

$m_e c^2$: rest energy of the electron;

r_e : classical electron radius;

β : velocity of the traversing particle in units of c ;

γ : Lorentz factor $1/\sqrt{1-\beta^2}$;

I : mean excitation energy (137 eV for silicon)

$T_{max} = \frac{2m_e c^2 \beta^2 \gamma^2}{1+2\gamma m_e/M+(m_e/M)^2}$: maximum energy loss for a particle with mass M

This equation describes the average energy loss per mass surface density. Additional corrections were taken into account as the density correction for high particle energies [52], for electrons and positrons due to their low mass while interacting with identical particles traversing the medium and the Bremsstahlung mechanism. For non-relativistic energies or low energies, the dE/dx is dominated by $1/\beta^2$ and decreases with increasing velocity until $\beta \approx 0.96$ ($\beta\gamma \approx 3$), where a minimum is reached. Particles at this point are known as minimum ionization particles (MIPs). The minimum value of the dE/dx is very similar for all particles of the same charge. At more considerable energies beyond this point, the factor $1/\beta^2$ becomes almost constant and the dE/dx rises again due to

the logarithmic dependence of the Equation. Nevertheless, this relativistic rise is almost flattened by the density leading to a plateau [52]. The Bethe-Bloch equation describes only the average energy loss by charged particles passing through the medium, not including its fluctuations. These fluctuations arise for thinner materials. For the thickness of about 300 μm silicon, fluctuations around the mean value are well described by a Landau distribution [53], and for thicknesses between 20 μm and 30 μm , the energy loss is more accurately described by the Bichsel model [54]

3.1.2 Energy loss of electromagnetic radiation

The interaction of electromagnetic radiation with matter is different than charged particles. Photons interact with material mainly via three processes: photoelectric effect, Compton effect, and pair production [55]. The three processes mentioned above remove photons from the beam in the interaction, including absorption and scattering. However, photons that do not interact can pass through the material retaining their original energy. A photon beam that passes a layer of material does not modify its energy; however, it is attenuated in its intensity and can be expressed as 3.2: [11].

$$I(x) = I_0 e^{-x/\lambda} \quad (3.2)$$

Where I_0 is the incident beam intensity, I is the beam intensity after traversing thickness x of the absorber, λ is the attenuation length which is a characteristic of the material and also depends on the photon energy [11].

The photoelectric effect is an electromagnetic interaction between photons and electrons, where an atomic electron absorbs the photon energy, and as a consequence, it is ejected from the atom. This effect dominates up to a few tens of keV. The Compton effect dominates around 1 MeV, and the pair production process occurs when the energy of the photon is larger than 1.02 MeV [57]. Below 100 keV for silicon, the photoelectric effect is dominant, and the electron emitted after a photoelectric absorption will generate

further electron-hole pairs along its path. The average energy necessary to produce a single electron-hole pair is $w = 3.6$ eV in silicon, and the average number of electron-hole pairs N_{e-h} generated by a photon with energy E_{ph} can be obtained as:

$$N_{e-h} = \frac{E_{ph}}{w} \quad (3.3)$$

This expression is useful when a silicon pixel detector is radiated with an X-ray source characterized like Fe^{55} for calibration and test.

3.1.3 Collection diode

The basic building block of a CMOS MAPS is a reversely biased silicon diode p-n junction, where a depletion layer is formed, which originates an electric field to allow the collection of charges and suppresses the leakage current [58].

In the p-n junction for MAPS, the effective concentration of the acceptor is $N_A \approx 1 \times 10^{12} \text{ cm}^{-3}$, and the effective concentration of the donor number is $N_D \approx 1 \times 10^{17} \text{ cm}^{-3}$. These different concentration levels originate a carrier diffusion into some of the differently doped sides. A region formed around the junction is named the depletion region, where the acceptor and donor are left. This charged region causes an electrical field. At thermal equilibrium, the electrical field in the depletion region can be characterized by the *built-in voltage* V_{bi} [58].

$$V_{bi} = \frac{k_B T}{q} \ln\left(\frac{N_D N_A}{n_i^2}\right) \quad (3.4)$$

where n_i is the intrinsic carrier concentration, k_B is the Boltzmann constant, q is the unit charge, and T is the temperature. The N_A and N_D were mentioned before. The width of the depletion region (d) depends on the doped concentration on both sides of the junction $d = d_n + d_p$ and also on the *reverse bias voltage* V_{RB} ; from these, a width depletion region can be expressed as:

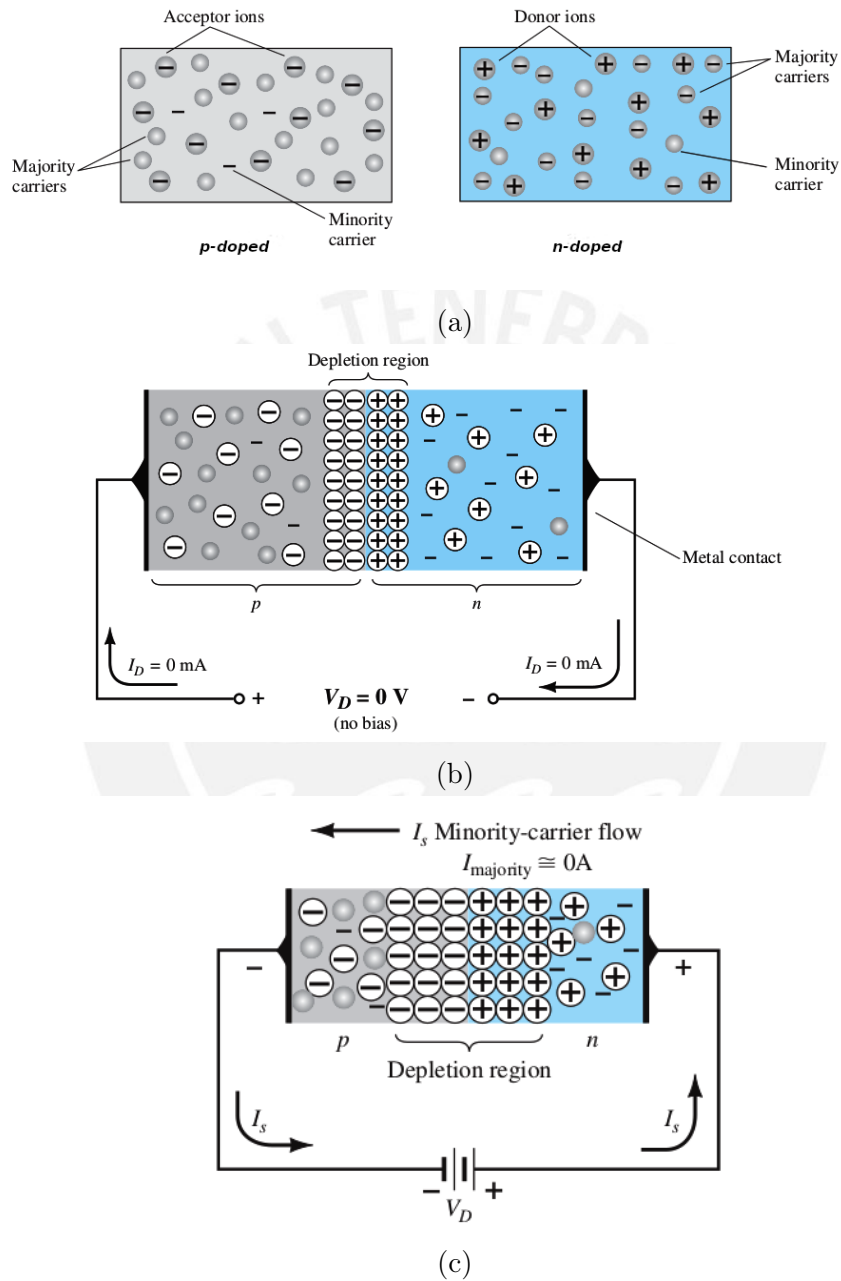


Figure 3.1: p-n junction process. a: Type n and p doped, b: Depletion formation, and c: internal distribution of charge under reverse-bias conditions. Image obtained from [60]

$$\begin{aligned}
d &= d_n + d_p \\
&= \sqrt{\frac{2\varepsilon_0\varepsilon_{Si}}{q} \left(\frac{1}{N_A} + \frac{1}{N_D} \right) (V_{bi} - V_{RB})}
\end{aligned} \tag{3.5}$$

where ε_0 and ε_{Si} are the dielectric constant in vacuum and silicon respectively. According to the doping concentration in MAPS $N_D \gg N_A$, we can consider in equation 3.5 the factor $(1/N_A + 1/N_D) \approx 1/N_A$, and then re-write it as:

$$d \approx \sqrt{\frac{2\varepsilon}{q} \frac{1}{N_A} (V_{bi} - V_{RB})} \tag{3.6}$$

An increase in the value of the reverse bias voltage leads to an increase in the size of the d . The capacitance in planar junction is estimated according to a parallel plate capacitor by:

$$C = \varepsilon \frac{A}{d} \tag{3.7}$$

where A is the planar area, ε is the electric permittivity of the material, and d is the separation distance. We can re-write C using the d of the previous equation as:

$$C = \varepsilon A \sqrt{\frac{qN_A}{2\varepsilon(V_{bi} - V_{RB})}} = A \sqrt{\frac{\varepsilon q N_A}{2(V_{bi} - V_{RB})}} \tag{3.8}$$

The capacitance value depends on the junction of area A and the width depletion region. Indeed, according to equation 3.8, the increase in the value of the d leads to a decrease in the capacitance value [58].

3.2 Principles of Operation of MAPS

A monolithic active pixel sensor developed as a detector of high-energy particles is made up of three layers, as is shown in Fig. 3.2 [59]. The first layer is a highly p-doped (p^{++}) substrate with $\sim 50\mu\text{m}$ used as mechanical support. The second layer, the epitaxial layer, is used as a sensitive layer with a thickness between 10 and $40\mu\text{m}$ to guarantee maximum charged collection [57], and the last layer is called the wells $\sim 1\mu\text{m}$, where the n-well and

$$i = eE_w \cdot v \quad (3.9)$$

where E_w is called *weighting field*. By comparison, the electric field E inside the sensor which caused the drift velocity v , the *weighting field* E_w describes the coupling of the induced current to the electrode. A way to calculate the charge Q collected at electrode is the integral of the induced current.

$$Q = \int_{t_1}^{t_2} i(t) dt = e(\phi(x_1) - \phi(x_2)) \quad (3.10)$$

where ϕ is the *weighting potential*, which is obtained by setting the electrode to unit potential, and all other to zero, after that solving the Poisson equation [58].

3.2.2 Spatial resolution

The spatial resolution is determined by pixel pitch p , the readout type analogue or single threshold binary and the charge sharing between pixels. The pixel pitch is defined as the axial distance between the centers of two adjacent pixels.

Binary readout

For a single threshold binary readout, the theoretical spatial resolution is calculated with pitch centered around position zero. Additionally assuming the tracked particle only activates one threshold per pixel, and only particles hitting the detector between $-p/2$ to $p/2$, the spatial resolution calculated is given by [58]:

$$\sigma_p = 0.28 \times p \quad (3.11)$$

Analogue readout

The analogue readout can give us an additional improvement of the spatial resolution, that provides a signal proportional to the collected charge in each pixel. In the case of two adjacent pixels collected signal, the appropriate aspect is to assume the charge sharing is linearly dependent. To improve the technique it is better to use an elaborate

interpolation method called η -function [66] which related the signal to noise ratio of the analogue signal [58].

3.3 Radiation damage effects

A sensor is degraded in its capacity to collect signal due to high particle fluence related to high collision rates and track densities. The radiation induces effects (radiation damage) which are divided into bulk and surface defects.

The Bulk damage

It is caused by the inelastic displacement of nuclei in the sensor due to interaction with high-energy particles. The interaction of the incident particles with the nuclei of the lattice atoms can generate imperfections in the crystal structure, which create additional energy levels within the silicon band-gap and consequently variation in the electrical properties of the material. To remove a silicon atom from its lattice position, it is necessary a certain minimum energy, for example, electrons require the energy of 260 keV, while protons and neutrons need only 190 eV [58]. The deterioration effects depend on the particle type, energy and fluence (the number of arriving particles). To compare the damages that sensors suffer one universal damage parameter is established, which is known as non-ionization energy loss (NIEL), and it represents the damage generated by 1 MeV equivalent neutron fluence, which is used as a reference. The defects related to the bulk damage are leakage current, effective doping concentration, and charge trapping. An increase in the leakage current conduce to need more charged particles to hit a pixel, changes in the effective doping concentration may change the dimension of the depletion region, and effecting the collection of the charged particle [58].

Surface damage

At the top of the sensor there is SiO_2 , which acts as an isolator layer of MOSFET. The structure of SiO_2 is highly irregular, and the displacement of atoms due to radiation might not lead to macroscopic changes. However, ionization in the oxide layer may cause

permanent changes in interface properties. It creates electron-hole pairs, most of them recombine immediately, and the others take another way. For example, electrons are collected by any positive electrode, and the holes are trapped in the interface region, which originates a shift of the threshold voltage and increases the noise [57] .

3.4 Small scale prototypes

The ALPIDE (ALice PIxel DEtector) is a silicon pixel detector based on a CMOS monolithic active pixel sensor, which is developed for the Muon Forward Tracker and the upgrade program of the Inner Tracking System in the ALICE experiment at CERN.

To arrive to the final version of the ALPIDE different previous prototypes were developed and tested, by studying their efficiency in relation to the pixel size, the size of the collection electrode, the pixel reset system after readout, the integration time, radiation hardness, etc [57] [61].

In 2012 started the development of different ALPIDE versions for the test to optimize the sensor. Explore-0 and Explore-1 were the first small-scale prototypes composed of two matrices of pixels [62].

The first matrix on the left side of the chip arranged in 90 columns and 90 rows contained pixels with a size of $20\mu\text{m} \times 20\mu\text{m}$, while the matrix on the right contained pixels pitch of $30\mu\text{m} \times 30\mu\text{m}$ arranged in 60 columns and 60 rows. Also, each matrix was sub-divided into nine sectors and each one with different sizes in the diode collection electrode geometry and the space between n-well and surrounding p-well. The results of the tests confirmed that the lateral spacing between n-well and p-well determined the capacitance and, as expected, the signal charge increased with increasing the epitaxial layer thickness.

A second small-scale prototype was the pALPIDEss arranged with 512 rows and 64 columns, and area per pixel of $22\mu\text{m} \times 22\mu\text{m}$. It was used to characterize the low power front-end, the hit-driven readout circuit, also, studies of noise and threshold distributions

[62].

3.5 pALPIDE-1 sensor

The first-full scale prototype was the pALPIDEfs (pALPIDE-1) arranged with 512 rows and 1024 columns and a pitch of $28 \mu\text{m}$. The chip measured $15 \text{ mm} \times 30 \text{ mm}$ to start the study of system level and integration aspects. It was designed with a low power consumption of the front-end and the sparsified readout architecture according to the ALPIDE design. The total thickness of the chip was $\sim 50 \mu\text{m}$ composed by substrate, epitaxial layer, n-well, and p-well as is illustrated in Fig. 3.3. The pixel matrix was subdivided into four sectors of 512×256 as shown in Fig. 3.4. Each sector was built with a different pixel type. The details are shown in Table 3.1 [57]. Over the top 72 power pads are placed to be connected with power lines to ensure the power distribution. However, this version did not implement the final interface, the high-speed output link, and the n-pixel multi-event buffer [57].

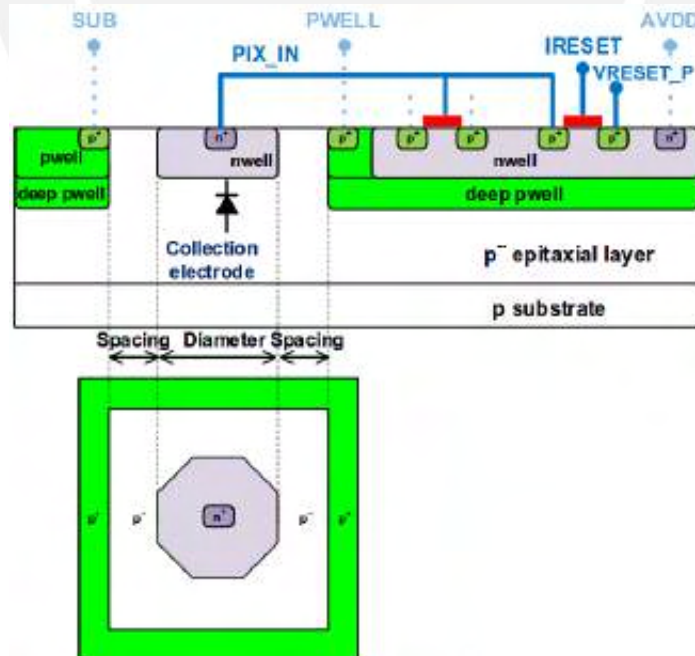


Figure 3.3: View of the cross-section pixel pALPIDE, and top view of the charge collector. Image obtained from [63].

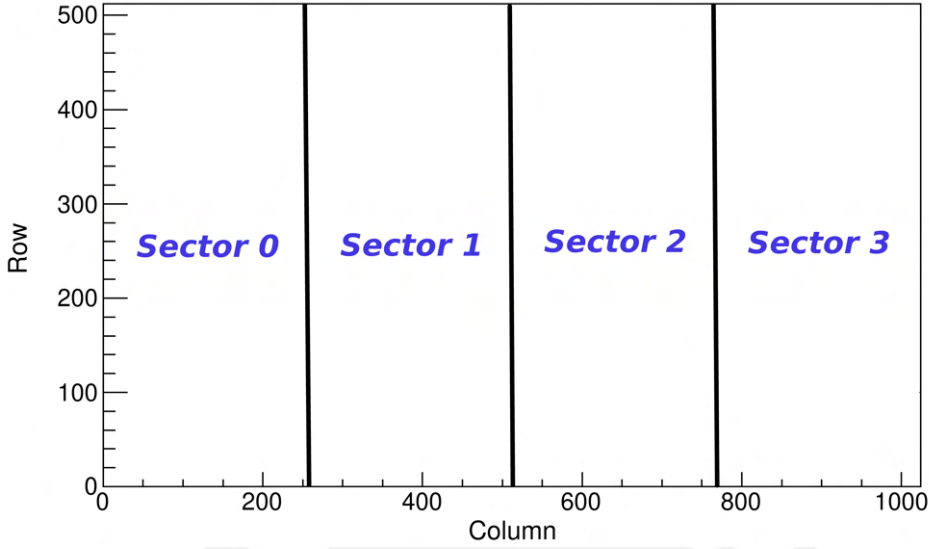


Figure 3.4: Position of the four sectors in the pALPIDE-1 and pALPIDE-2.

Table 3.1: Characteristics of the four different pixel types of the pALPIDE-1

Sector	Columns	N-well diameter	Spacing	p-well opening	Reset type
0	0 - 255	2 μm	1 μm	4 μm	PMOS
1	256 - 511	2 μm	2 μm	6 μm	PMOS
2	512 - 767	2 μm	2 μm	6 μm	Diode
3	768 - 1023	2 μm	4 μm	10 μm	PMOS

3.6 pALPIDE-2 sensor

The pALPIDE-2 is the second full-scale prototype with a dimension of 30 mm \times 15 mm arranged in 1024 \times 512 pixels with a pitch of 28 μm . As part of our work, we use this version of ALPIDE to characterize. The pixel matrix is grouped into 32 regions. Each region contains 16 double columns. One of its main features is a mask register per pixel and a single in-pixel hit buffer per pixel. The Address Encoder Reset Decoder (AERD) is an asynchronous circuit that manages the readout of the pixel matrix circuitry of pALPIDE, which is implemented using a full-custom logic to save space and routing resources within the matrix.

This sensor was implemented with the final version of the interface, however, its speed output is only 40 Mbit/s. The high-speed serialiser is not integrated into pALPIDE-2. The power consumption per pixel in the front-end is 40 nW leading to a power density of 4.7 mW/cm². The front end in both pALPIDE-1 and pALPIDE-2 are similar, in addition, both of them have four sectors, nevertheless, with different lengths in p-well opening and spacing. Also, the diode reset is at sector S3 and PMOS reset on the other sectors. Table 3.2 shows the detailed characteristics for the four sectors of the pALPIDE-2.

The charge collection diode is obtained by implementing the n-well in the epitaxial layer. With an octagonal shape for the deep n-well, but a square shape for the deep p-well to minimize couplings between them, and in contrast to maximize the ratio between collected charge and input capacitance (Q/C) [19].

Table 3.2: Characteristics of the four different pixel types of the pALPIDE-2

Sector	Columns	N-well diameter	Spacing	p-well opening	Reset type
0	0 - 255	2 μm	2 μm	4 μm	PMOS
1	256 - 511	2 μm	2 μm	6 μm	PMOS
2	512 - 767	2 μm	4 μm	6 μm	PMOS
3	768 - 1023	2 μm	4 μm	10 μm	Diode

In the ALPIDE family design only the information whether a pixel was hit is readout. The hit discrimination is implemented at the pixel level, while the threshold settings for the discriminators are provided globally [57]. The digital pixel outputs are connected to a digital circuit, called AERD [64], which is arranged in the center of a pair of columns, the schematic design of the matrix layout can be seen in Fig. 3.5 [65]. Following a structural priority, this circuit sequentially provides the addresses of hit pixels to the digital periphery of the chip. This circuit is implemented to register hits of the respective pixel and then reset it after the read operation, whereupon the AERD moves to the next hit pixel. This procedure is iterated until all hit pixels within a double-column are readout. The data regions are taken by a region readout unit (RRU), which buffers the hit data. The top readout unit (TRU) combines the data of the 32 RRU and transmits it through an 8 bit

wide CMOS data port at 40 MHz. The top-level control block, interfaced by Joint Test Action Group (JTAG) enables access to the control and status registers in the periphery.

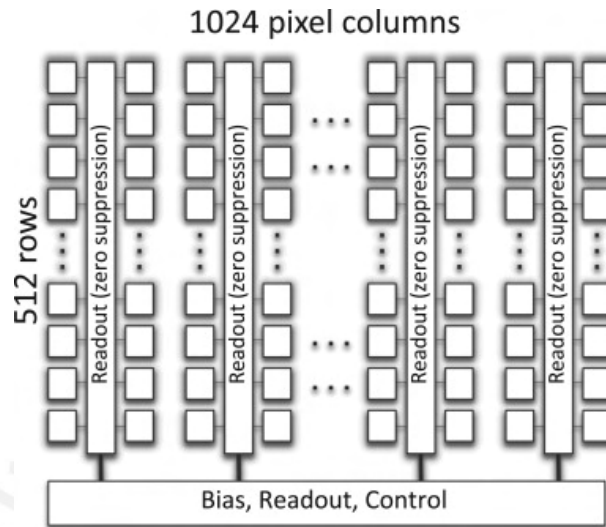


Figure 3.5: The pixel matrix is organized in double-columns and each of them shares a priority encoder. One double-column carries 1024 pixels. Image obtained from [57].

3.6.1 Pixel matrix

The pixel matrix is divided into four sub-matrices of 256×512 pixels, also they are called sectors: S0, S1, S2 and S3. They are similar to pALPIDE-1, which is shown in Fig. 3.4. Each sector is composed of different pixels types. The four types of pixels differ by the geometry of the collection diode and the implementation of the reset mechanism for the sensing node. The details are shown in Table 3.2 [67]. Two reset mechanisms are implemented in the pALPIDE-2, the reset via PMOS transistor and reset via diode as is shown in Fig. 3.6 [19]. In both cases, the collection diode is continuously reset.

3.6.2 Front-end circuit

The front-end circuitry of the pALPIDE-2 consists of an analogue and digital part where the analogue signal is shaped and discriminated, and a digital part containing the hit register and additional logic for testing and disabling by masking the pixel. The func-

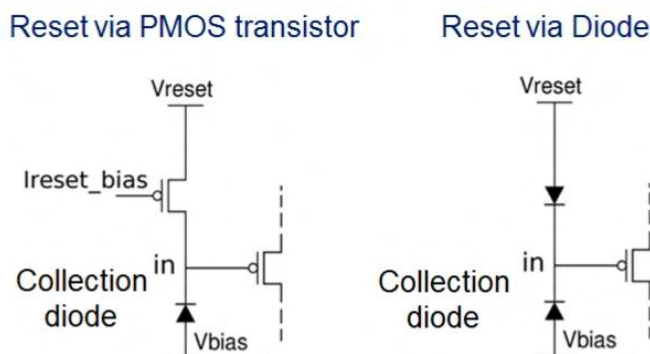


Figure 3.6: The pALPIDEfs-2 reset mechanisms: reset via PMOS transistor (left) and reset via Diode (right). Image obtained from [19].

tionality of the chip depends on the voltages and currents applied to its elements, namely V_{RESET} , I_{THR} , V_{CASN} and I_{DB} . The details are presented next [19].

Analogue part

The analogue front-end circuit is shown in Fig. 3.7 which is subdivided into two stages: the first stage, also referred to as the gain stage, consists of two branches related to the current sources I_{BIAS} and I_{THR} . The second stage is also referred to as the discrimination stage, which is related to the current source I_{DB} . In the absence of perturbations, the potential at the SOURCE node can be defined by the equilibrium potential at the sensing node. When charged particles cross the sensor the sensing node potential drops within $4\mu\text{s}$ [61] due to the collection of charge generated in the sensor, and as a consequence the V_{gs} of the PMOS input transistor will be increased. Subsequently, this leads to an additional current I_{s} through M2 and M3. For this additional current to be allowed to pass M4, the voltage at its gate, that is the CURFEED node, would have to adjust, the current I_{s} will charge the OUT node, creating a positive voltage pulse. After the onset of the pulse, the OUT node is restored to its baseline. On the stage for the discrimination, the pix out node is connected to the gate of transistor M5. At this time the pulse amplitude at the pix out node exceeds a certain critical voltage $V_{\text{c},\text{M5}}$ forcing an NMOS transistor into conduction. Consequently, if the current through M9(M5) surpasses I_{DB} , the node

PIX_OUT_B will be driven low. When the pulse at node pix out returns to the baseline and below V_c , M5, then transistor M9 stops conducting and the node PIX_OUT_B becomes high again [57].

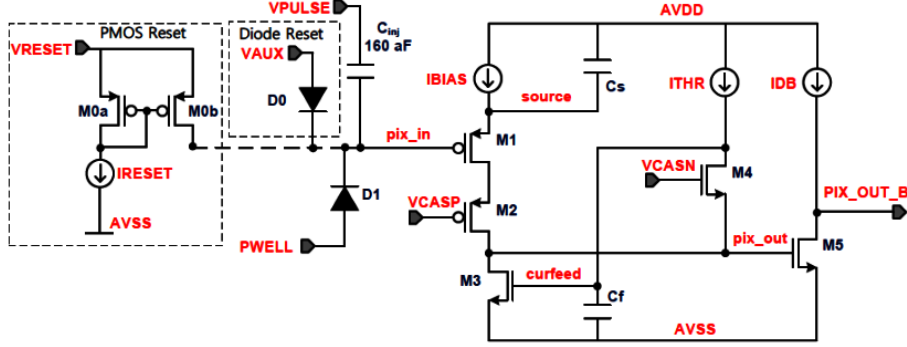


Figure 3.7: Schematic view of analogue front-end for pALPIDE-2. Image obtained from [19].

The peak height and the pulse width for the circuit presented are larger for greater amounts of collected charge.

Digital part

The digital part of the front-end circuit is shown in Fig. 3.8. Each connection and functionality is described in Table 3.3 [68]. The digital part has three registers, from top to bottom; Pulse, Mask, and State register also two demultiplexers and four logic gates. The pulse register enables the possibility to access each pixel for testing of the front-end response and the functionality of the state register, PULSE_TYPE input and PULSE_EN control the APULSE, and DPULSE, analogue pulse for PULSE_TYPE=1 and digital pulse for PULSE_TYPE=0 through demultiplexer. In digital testing, the digital pulsing gives a high signal or hit information to the state register bypassing the analogue front-end and the STROBE_B signal, also the pixel is not masked. In the case of analogue testing, the analogue pulsing allows the injection of a test charge Q_{inj} into the sensing node by the capacitance C_{inj} . The effective charge injected is defined by

$$(VPLSE_HIGH - VPLSE_LOW) \times C_{inj}.$$

The state register manages the hit information when the PIX_OUT_B signal from the analogue front-end is asserted simultaneously with the STROBE_B signal generated by the digital periphery of the chip. This register is reset by a PIX_RESET pulse generated by the priority encoder during the readout or either by a global PRST pulse.

The mask register sets a MASK_EN in high, the STATE output is 0, allowing the readout not to be loaded due to malfunctioning. The set in low value provides normal functionality.

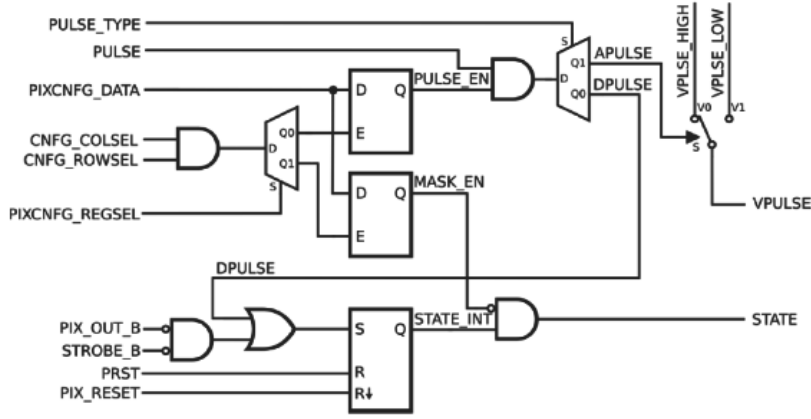


Figure 3.8: The digital part at the front-end for pALPIDE-2. Image obtained from [19]

3.7 pALPIDE-3

The pALPIDE-3 is the third full-scale prototype and it is divided into 8 sectors of 512×128 pixels, for this version the pixel size is $29.24 \mu\text{m} \times 26.88 \mu\text{m}$ [69]. Each sector implements a different front-end flavour, as reported in Table 3.4. In each sector, the collection n-well has an octagonal shape with $2 \mu\text{m}$ of diameter. All sectors have $2 \mu\text{m}$ spacing, except sector 5 which has $3 \mu\text{m}$ [70]. The front-end circuits in pALPIDE-3 are based on the pALPIDE-1/2 front-end circuit with step-by-step modifications in order to trace the effects on performance. This version has the final interface with a high-speed output serial

Table 3.3: Signal of the pixel [68]

	Signal	Description	Logic level	
			0	1
INPUT	PULSETYPE	Pulse type selection	Enable DPULSE	Enable APULSE
	PULSE	CMOS pulse	DPULSE and APULSE	
	PIXCNFG_DATA	Configuration data	D-LATCH data line	
	PIXCNFG_COLSEL	Column selection	Disable	Enable
	PIXCNFG_ROWSEL	Row selection	Disable	Enable
	PIXCNFG_REGSEL	Register selection	Pulse reg.	Mask reg.
	PIX_OUT_B	Pixel front-end output	Active low	
	STROBE_B	Strobe window	Active low	
	PRST	State register reset (global)	Active high	
	PIX_RESET	State register reset from priority encoder	Effective on falling edge	
	VPLSE_HIGH	Analog pulse high level	Analog	
	VPLSE_LOW	Analog pulse low level	Analog	
	INTERNAL	PULSE_EN	Pulse enable	Active high
MASK_EN		State register mask enable	Active high	
STATE_INT		State register data	Active high	
APULSE		VPULSE voltage level selection	VPLSE_HIGH	VPLSE_LOW
DAPULSE		Digital Pulse	Hold STATE_INT	STATE_INT = 1
OUTPUT	VPULSE	Voltage step for test charge injection into pix_in	$Q_{inj} = \Delta(VPULSE) \cdot C_{inj}$	
	STATE	State register value to priority encoder (if MASK_EN = 0)	Active high	

link of 1.2 Gbit/s.

Table 3.4: Characteristics of the front end circuit of the pALPIDE-3

Sector	size(M3, M4, M6, M8)	V _{CASN2}	Clipping	M1 bulk	Reset	Spacing
0	optimized size	yes	diode con	AVDD	Diode	2 μ m
1	optimized size	no	diode con	AVDD	Diode	2 μ m
2	as in pALPIDE-1,2	no	diode con	AVDD	Diode	2 μ m
3	optimized size	yes	V _{clip}	AVDD	Diode	2 μ m
4	optimized size	yes	V _{clip}	Source	Diode	2 μ m
5	optimized size	yes	V _{clip}	Source	Diode	3 μ m
6	as in pALPIDE-1,2	no	diode con	AVDD	PMOS	2 μ m
7	optimized size	yes	V _{clip}	AVDD	PMOS	2 μ m

3.8 ALPIDE sensor

The MAPS ALPIDE is the final version of the sensor required for ITS and MFT based on the 180 nm CMOS technology of Towerjazz [71], in which the charge generated at the epitaxial layer by the ionizing particle is only collected by n-well. The p-well contain the

CMOS pixel electronics for the readout [62]. This technology uses up to 6 metal layers to build the CMOS circuitry ensuring low power consumption. ALPIDE contains a matrix of 512×1024 pixels with a size of $26.88 \mu\text{m} \times 29.24 \mu\text{m}$ and thickness of $50 \mu\text{m}$ [72] which is the same size pixel and flavor of the sector 5 of pALPIDE-3. Where the n-well diameter is $2 \mu\text{m}$, the spacing is $3 \mu\text{m}$, and the reset system is managed by the diode. Additionally minor modifications were introduced in the periphery.

Table 3.5: Differences between pALPIDE-2 and ALPIDE (final version) [67] [72]

Characteristic	pALPIDE-2	ALPIDE
Pitch size	$28 \mu\text{m} \times 28 \mu\text{m}$	$26.88 \mu\text{m} \times 29.24 \mu\text{m}$
Thickness epitaxial	$40 \mu\text{m}$	$50 \mu\text{m}$
n-well	$2 \mu\text{m}$	$2 \mu\text{m}$
spacing	$2-4 \mu\text{m}$	$3 \mu\text{m}$
Reset system	PMOS & Diode	Diode

3.8.1 Pixel ALPIDE Architecture

The ALPIDE architecture is focused on in-pixel hit discrimination and zero suppression readout circuit by priority encoding [64]. Each pixel cell contains a sensing diode, a front-end amplifier and shaping stage, a discriminator, and a digital section as is shown in Fig. 3.9 in a simplified block diagram and signal flow.

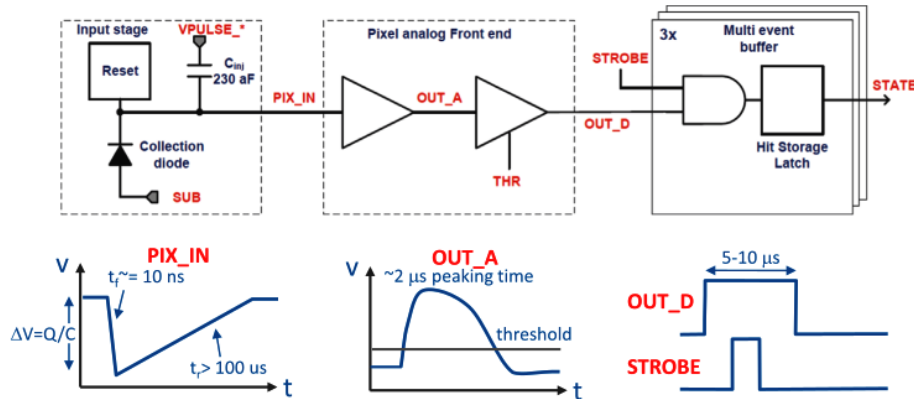


Figure 3.9: Schematic representation of the in-pixel circuitry implemented in ALPIDE sensor. Image obtained from [63]

The analogue stage, illustrated in Fig. 3.10, is composed of transistors (M) circuitry. When a particle hit is received and electrons arrived into the collection diode, the front end will increase the potential at the input of transistor M5 (pix_out), forcing it into conduction. If the current in M5 overcomes IDB, M5 will drive HIT_PIX_B low. The charge threshold of the pixel depends on the ITHR, VCASN and IDB. The effective charge threshold is increased by increasing ITHR or IDB. It is decreased by increasing VCASN. The active low PIX_OUT_B signal is applied to the digital section of the pixel.

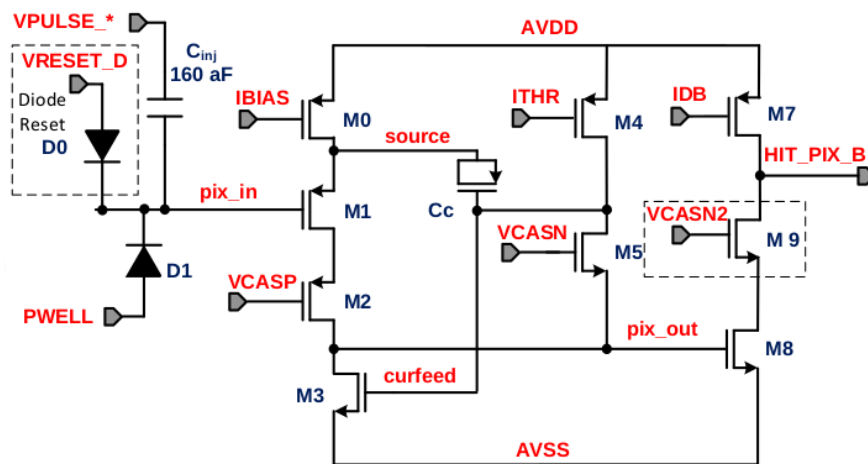


Figure 3.10: Analogue stage of the pixel ALPIDE [73]

The digital stage of the pixel is shown in Fig. 3.11. It is similar to pALPIDE-2/-3, and the main difference is in the STATE_IN, which for ALPIDE can buffer three states of hit information.

The High Energy Group at PUCP in Peru is a guest member of the MFT. The group was involved in the characterization of the ALPIDE-2. The first stage was done by Eric Endress and Sergio Best, where they analyzed the digital scan, analogue scan, source scan, and threshold scan tests varying temperature. In this thesis, we performed new characterization tests, which are shown in this Chapter.

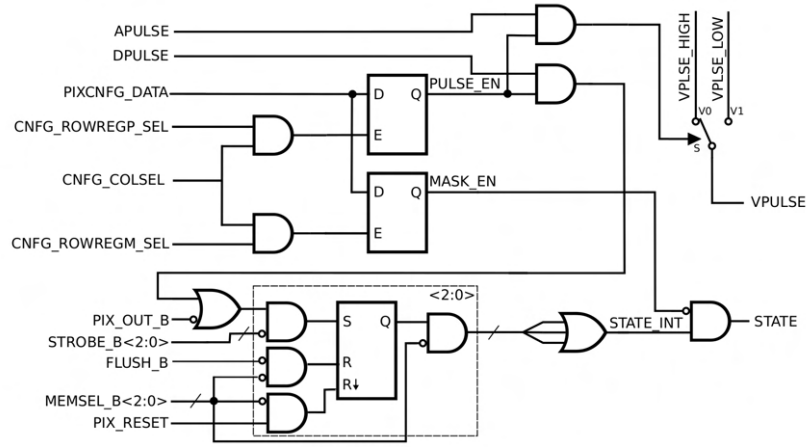


Figure 3.11: Functional diagram of the digital part for the pixel on ALPIDE. Image obtained from [73]

3.9 Digital Scan

The digital scan analyzes the response of the digital part pixel by pixel and reads the hits out by pulsing in the state register. It is run with the command `./runTest SCANDIGITAL PAR1 PAR2`, where `PAR1` represents the number of injections per pixel and `PAR2` is the number of mask stages (e.g. the number of pixels in each of the 32 regions). The digital scan gives the number of pixels that get a hit and their address. For our study, we run with `PAR1 = 60` (only to have more statistic) and `PAR2 = 16384` (whole pixel matrix). The results are shown in Fig. 3.12, which represents the distribution of hits for the tested pixels. For 60 injections per pixel, we can see in the upper plot of Fig. 3.12 that the majority of pixels achieve 60 hits. However, a few (around 200) pixels, which are located at 511 and 512 columns, do not work properly. They do not achieve 60 hits as is shown in the bottom plot of Fig. 3.12, which is a zoom. For this test we set `VCASN = 57 DAC`, `VBIAS = 0 DAC` and `ITH = 51 DAC` (default values).

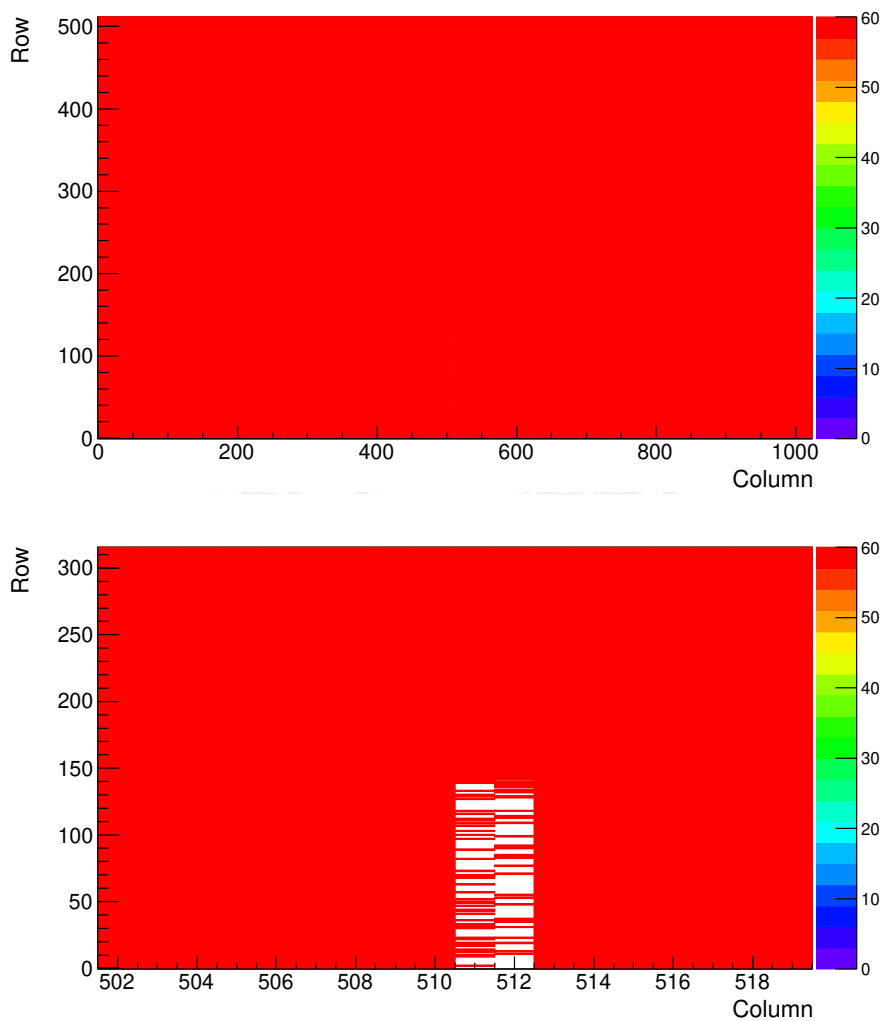


Figure 3.12: Hit map of the digital scan. Top: The pixel matrix tested for 60 injections per pixel. Bottom: Zoom of the hit map of a group of pixels at 511 and 512 columns, which do not properly respond.

3.10 Analogue Scan

The analogue scan works similar to the digital scan, however, instead of generating a digital pulse after the discriminator, a programmable charge is injected by VPULSE into the preamplifier to test the analogic part. The analogue scan test runs with the command `./runTest SCANANALOGUE PAR1 PAR2 PAR3`, where *PAR1* represents the charge in DAC units, *PAR2* is the number of injections per pixel and *PAR3* is the number of mask

stages. We set *PAR1* for 16 points (different values of ADC) from 0 to 150 DAC, 60 injections for each pixel, and analyzed the whole pixel matrix. We identified which pixels are working properly by finding 60 hits per pixel. Pixels that do not achieve 60 hits are called broken pixels. According to this procedure, we found about 300 pixels that do not respond properly or are broken, as shown in Fig. 3.13. For this test we set $VCASN = 57$ DAC, $VBIAS = 0$ DAC and $ITH = 51$ DAC.

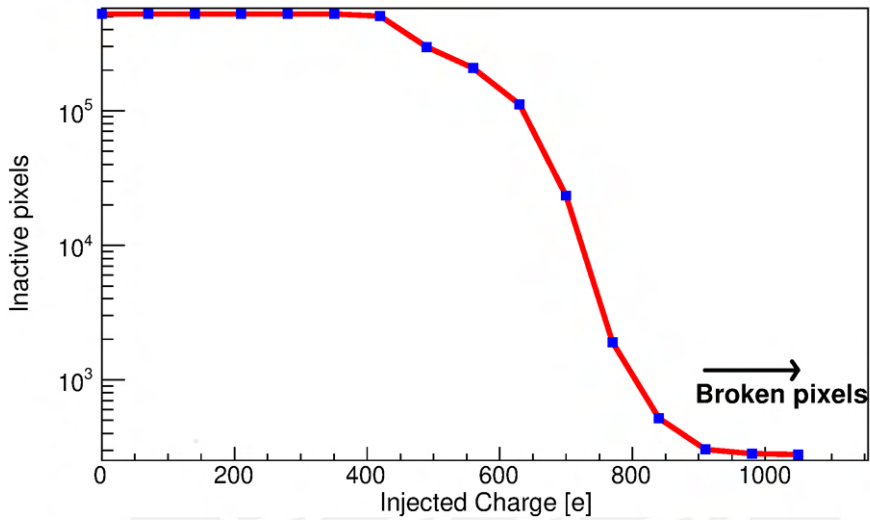


Figure 3.13: Analogue scan test responds to different injected charges. About 300 pixels are broken or do not respond properly.

3.11 Threshold Scan Studies

A difference to analogue scan, where threshold value was fixed in 51 ADC, the threshold scan test want to determine the threshold value for each pixel by performing analogue injections and looping over the charge. For each charge point, 50 injections are performed per pixel. The run command test is `./runTest THRESHOLD PAR1 PAR2 PAR3 [PAR4 PAR5]`, where *PAR1* is the mask stage, the charge loop is from *PAR2* to *PAR3* in DAC units. The output file contains the number of hits for each charge point and the pixel location. *PAR4* and *PAR5* are optional parameters to perform the test with a specific

set of VCASN and ITH, respectively.

To calculate the threshold value in a pixel; the normalized number of hits as a function of the charge injected is plotted in Fig. 3.14. The points are fitted with the following error function (red line).

$$f(x) = \frac{1}{2} \left[1 + \operatorname{erf} \left(\frac{x - \mu}{\sqrt{2}\sigma} \right) \right] \quad (3.12)$$

Where μ is the threshold value and σ is the noise of the pixel.

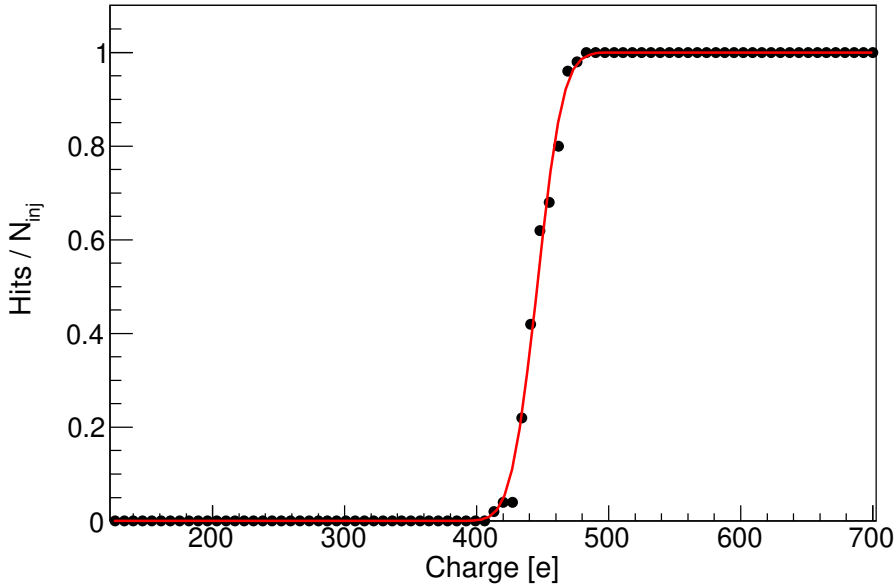


Figure 3.14: The $Hits/N_{inj}$ vs injected charge (black dots) fitted with an error function (red line) for threshold value and noise calculation.

We made threshold tests for the whole pixel matrix with default settings of VCASN = 57 DAC, ITH = 51 DAC, VBAIS=0 DAC, PAR1=0 and PAR2=120. In Fig. 3.15 we show the threshold map or the threshold value for each pixel. In sector 0 the majority of pixels have a threshold value around $419 e^-$, there are lower values with respect to other sectors, on the other hand, the higher values are around $642 e^-$, that are found in sector 3. Each sector can be identified by its mean threshold, which is associated with the color scale. The brilliant points show a high threshold level of the pixels originating from these

pads (connectors)[57].

Even though the four sectors are exposed at the same condition for the threshold test, the differences in the geometry of its collection diode, which is related to with pixel input capacitance, influenced the value of the threshold. Pixels with greater spacing between n-well and surrounding p-well showed higher levels of the threshold. The mean threshold value and its rms for each sector are shown in the Table 3.6, also similar behavior was found in [57].

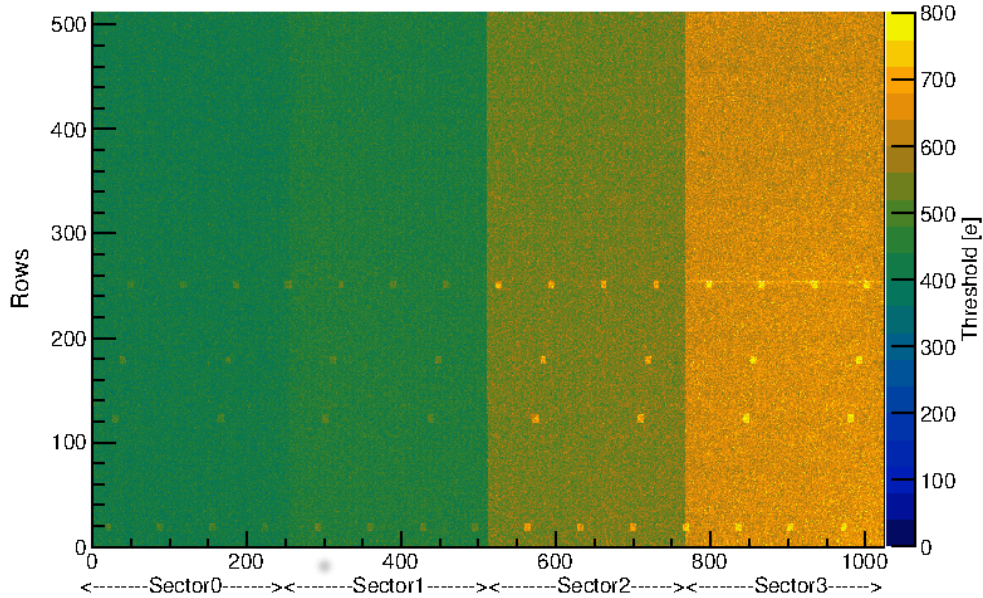


Figure 3.15: Threshold value per pixel for the whole pixel matrix with VCASN = 57 DAC, VBAIS = 0 DAC, and ITH 51 DAC.

The threshold distributions for all sectors are shown in Fig. 3.16. The distribution at sectors 0 and 1 are similar, however, the distribution at sectors 2 and 3 are very different. Distribution at sector 3 is less uniform and with a high rms value.

Additionally, we calculated the mean threshold value for each one of the 32 regions of the whole pixel matrix. Each region threshold has very close values as is shown in Fig. 3.17.

To verify the threshold variation as a function of the ITH, we keep VCASN = 57

Table 3.6: Mean threshold scan for the whole pixel matrix pALPIDE-2

Sector	Threshold (e^-)	rms-threshold (e^-)
0	419.9	24.7
1	442.4	25.3
2	541.5	31.7
3	642.3	39.9

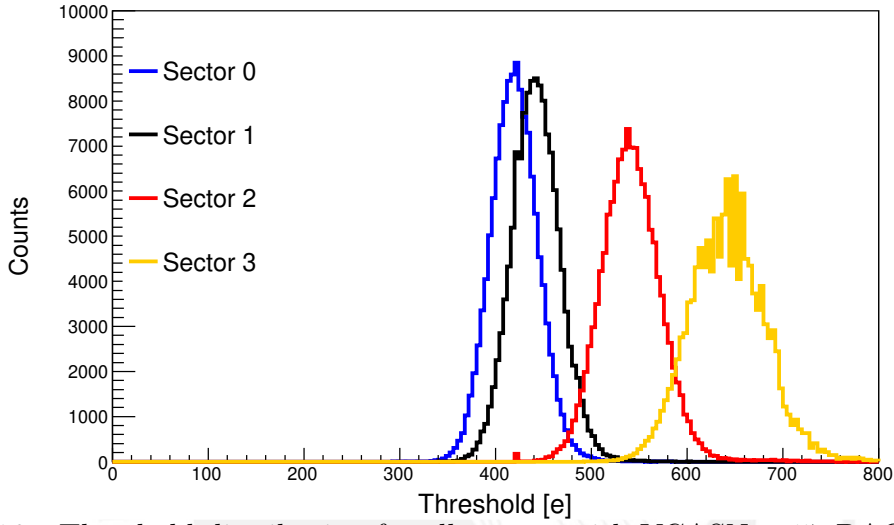


Figure 3.16: Threshold distribution for all sectors with VCASN = 57 DAC, VBAIS = 0 DAC and ITH 51 DAC.

DAC and VBIAS=0 DAC, with 60% of pixels scanned of the whole matrix, and vary ITH values for 51, 45, 40, 35 and 25 DAC. We found a decline in the threshold values when ITH decreases as is shown in Fig. 3.18 and the Table 3.7. Therefore, the threshold value is directly proportional to ITH.

Table 3.7: Mean threshold value sector for four different ITH

ITH (DAC)	25	35	40	45	51
S0 - TH	380.6	397.0	404.6	413.7	419.9
S1 - TH	400.7	418.3	426.5	435.9	442.4
S2 - TH	492.9	513.4	522.9	533.9	541.5
S3 - TH	584.5	609.2	617.8	633.8	642.3

Analyzing the behavior of the threshold distribution in each sector varying ITH, we found a displacement in the distribution for each ITH point as is shown in Fig. 3.19. For

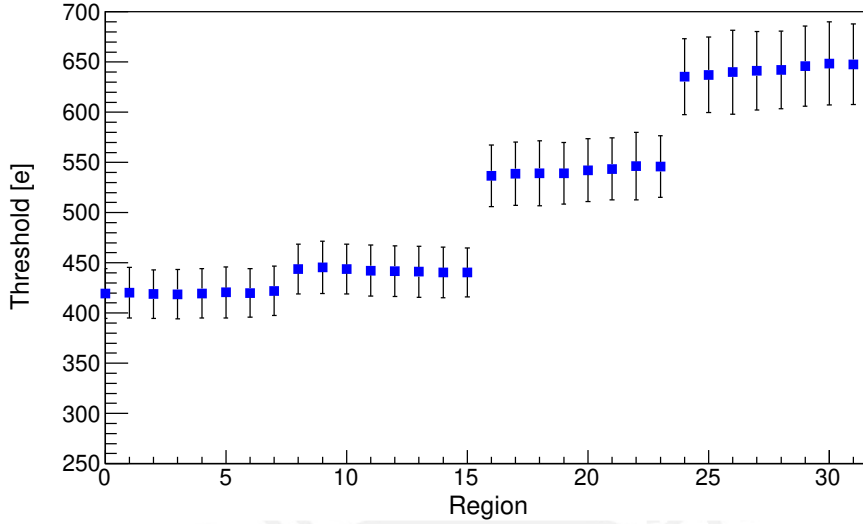


Figure 3.17: Mean threshold value in the 32 regions for VCASN = 57 DAC, VBAIS = 0 DAC and ITH = 51 DAC

sectors 0, 1 and 2, their displacement distributions are similar with varying ITH. However, sector 2 shows a seldom threshold value around 421 e. We checked the data and found that the pixels with this threshold value are not located in a specific region of the sector. In sector 3 the threshold distribution is wide and for ITH=45 DAC is not homogeneous.

3.12 Fake hit rate

The fake hit rate gives information about hits generated in absence of radiation source and ionization particles. A Fake hit is associated with noise fluctuation. The number of fake hits counted under the pixel matrix and the number of frames is called as fake hit rate. A higher rate is related to larger integration time and low threshold [57]. The way to analyze the fake hit is by the noise occupancy test. It sends random triggers and returns information of pixels which were hit. The fake hit rate for matrix pixels can be calculated by the equation:

$$R_{fh} = \frac{N_{fh}}{N_{pixel} \times N_{frames}} \quad (3.13)$$

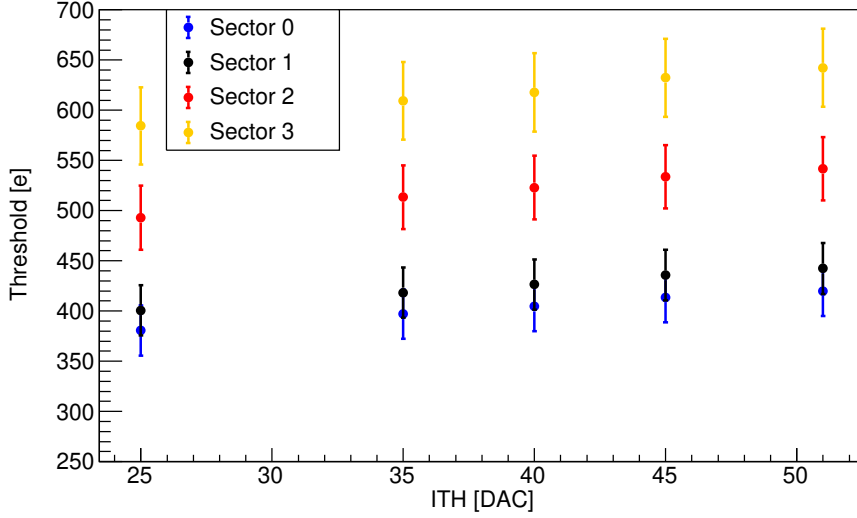


Figure 3.18: The threshold value varying ITH for each sector.

where N_{fh} is the number of fake hits, N_{pixel} is the number of pixels in the matrix, and N_{frames} is the number of frames or events.

For 1 million frames, ITH=51 ADC, VCASN 57 ADC, and VBB=0 ADC, we found that the fake hit rate for each sector is under the rate limit required for MFT (10^{-5} hits event $^{-1}$ pixel $^{-1}$). In sector 0 we found, the highest fake hit rate 0.236×10^{-5} , which is two orders of magnitude higher than other rates as is shown in Tab. 3.8.

Table 3.8: The fake hit rate for each sector of the pALPIDE-2

Sector	S0	S1	S2	S3
Fake hit 10^{-5}	0.236	0.003	0.070	0.046

One reason for the higher rate in sector 0 is its lower threshold value as found in the threshold test 3.11, however not only the threshold value influenced in the fake hit rate. Sector 3 showed the highest threshold value, but its fake hit rate is not the lowest, and it could be related to its high rms threshold.

Additional performance studies of the ALPIDE-2 at different temperatures were made in the lab of our university. These analysis, were made by Erick Endress and Sergio Best. They tested with 10, 24, 31, and 40 Celsius degrees.

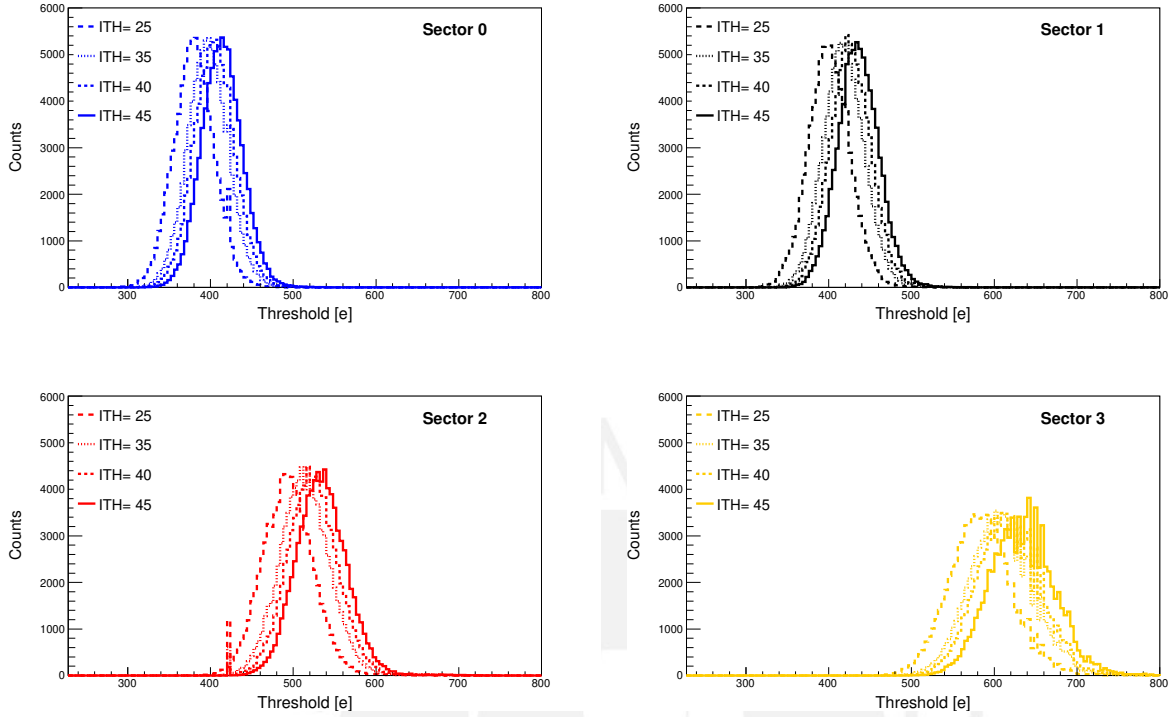


Figure 3.19: Threshold distribution for four different values of ITH for each sector.

In the analogue scan test, they found that pixels were more sensible to active at higher temperatures as is shown in Fig. 3.20, while temperature rise, electrons are released by thermal effect.

They also tested the threshold behavior for the four temperatures, and they found a slight decrease in the threshold value for increasing temperature and the rms decrease with increase of temperature as is shown in Fig. 3.21 and the Table 3.9. These tests showed an influence of the temperature in the threshold value.

Table 3.9: Mean threshold value by sector for four different ITH

Temperature	TH-S0	TH-S1	TH-S2	TH-S3
10°	237.97 ± 17.03	239.59 ± 16.38	296.92 ± 20.40	337.56 ± 23.62
24°	221.79 ± 16.33	224.37 ± 15.62	278.44 ± 19.43	316.82 ± 22.49
31°	214.16 ± 16.14	217.31 ± 15.39	269.96 ± 19.13	307.38 ± 22.12
40°	205.08 ± 16.03	208.91 ± 15.25	259.93 ± 18.93	297.23 ± 21.93

Jose Bazo and Jairo Rojas made another research to analyze neutron irradiation damage in semiconductors, in which they compared the emission spectrum between data and

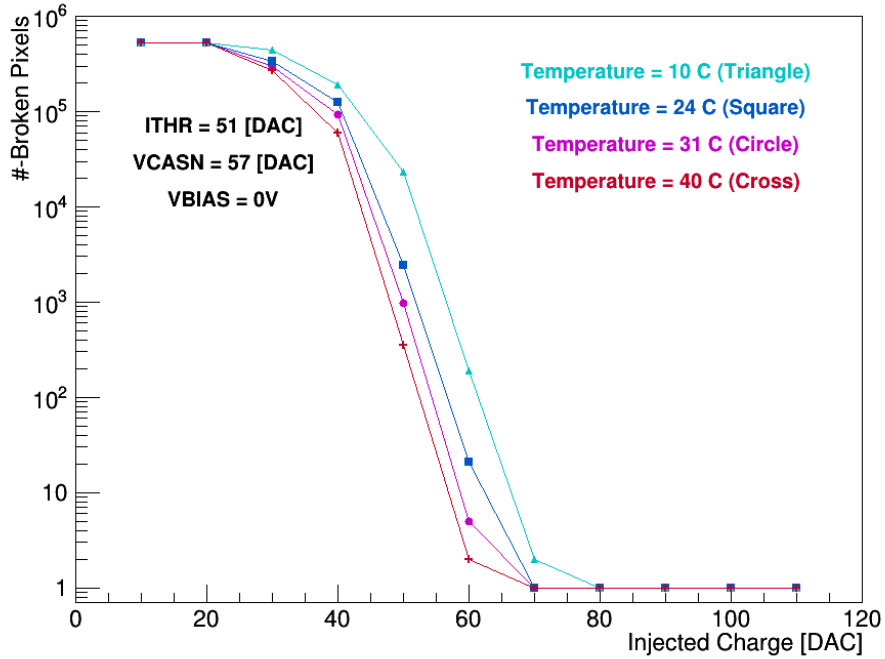


Figure 3.20: Hit response of pixels at different temperatures.

simulation of radionuclides samples, and they found a 13 % in agreement. Samples were Silicon and Germanium. Simulations were made with FLUKA. More information can be found in [74]

Radioactive sources are well identified and have been used as tools to research and characterize sensors. One of the most used is Iron-55 [75]. In this chapter, we analyzed the hits generated in the pALPIDE-2 by radiation of Iron-55.

3.13 Radioactive Source Iron-55

Radioactive sources are well identified and have been used as tools to research and characterize sensors. In this section, we analyzed the hits generated in the pALPIDE-2 by radiation of Iron-55.

Iron-55 (^{55}Fe) is an isotope of iron and a radioactive source which decays by K electron capture to Manganese 55 (^{55}Mn) with a half-life of $T_{1/2} = 2.747$ years. The vacancy in

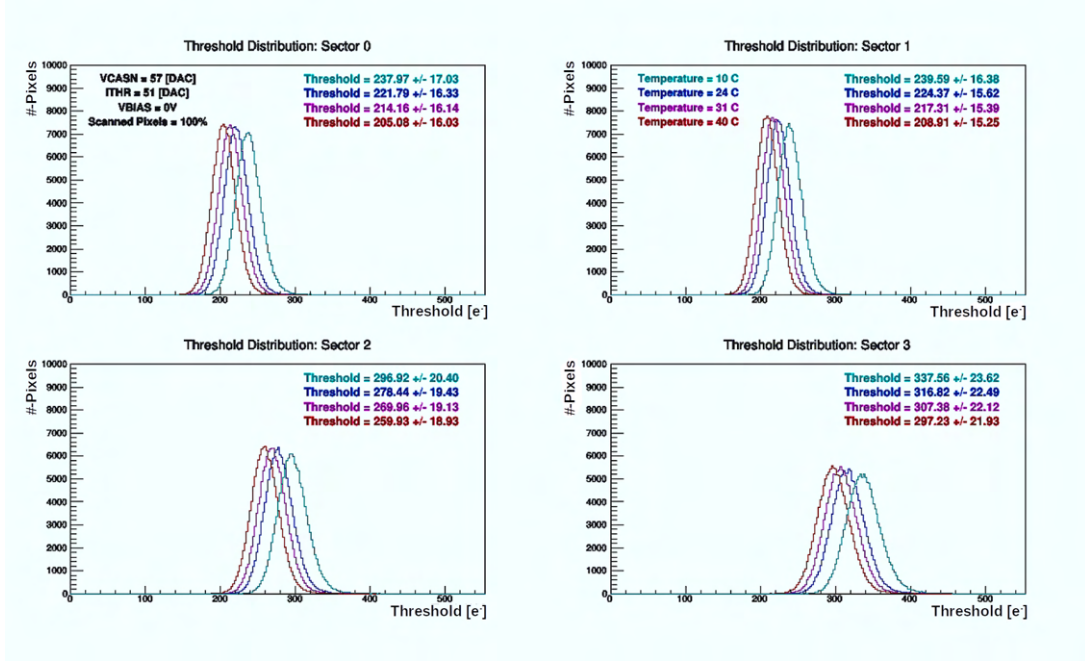


Figure 3.21: Hit response of pixels at different temperatures.

the level K generates a transition of an electron from the higher levels realising energy by emission of an Auger electron or X-rays with a probability of 60% and 28% respectively. The remaining fraction corresponds to lower-energy transitions.

The X-rays related with energies of the $K_{\alpha 1}$ and $K_{\alpha 2}$ are similar and are observed as mono-energetic 5.9 keV, which represents an emission probability of $\sim 25\%$. The remaining 3.4% corresponds to K_{β} with 6.5 keV [76]. The number of electrons, X-rays and gammas per 100 decays are shown in Table 3.10, according to [77].

Table 3.10: Emission channels after ^{55}Fe decays into ^{55}Mn per 100 decays [77]

	Energy (keV)	Emissions per 100 decays
Auger electrons	0.47 - 0.67	140.2
	4.95 - 0.67	60.1
X-rays	0.56 - 0.72	0.524
	5.888	8.45
	5.899	16.57
	6.490	3.40
γ	125.959	1.3×10^{-7}

For electrons with 10 keV their range in air at sea level is around 2.88×10^{-4} g/cm² [78]. Thus these electrons on average should not travel more than 0.24 cm. Consequently, electrons produced in ⁵⁵Fe are absorbed by the air for distances greater than 0.24 cm during their propagation. Therefore electrons between the ⁵⁵Fe-source and the detector are not taken into account in our analysis.

For distances greater than one centimeter only X-rays and gammas of the ⁵⁵Fe can reach the sensor, however their radiant flux decrease with the inverse-square of the distance. Also according to the Beer-Lambert law $I = I_0 e^{-(\mu/\rho)x}$ (μ/ρ is the mass attenuation coefficient and x is the thickness mass) for a higher value of μ/ρ , there is a greater suppression suffered in the intensity of a beam.

The mass attenuation coefficient depends on the energy of the photon and the medium. That is shown in Fig. 3.22 for energies from 1 to 100 keV of X-ray passing air [79]. The mass attenuation coefficient in the air for 5.9 and 5.6 keV is 23.7 and 17.7 cm²/g, respectively. That means they are slightly attenuated in few centimeters.

Varying distance on few centimeters between the ⁵⁵Fe-source and the detector, it is possible to identify the flux variation. To analyse the decrease of X-ray intensity, we use the ⁵⁵Fe-source and pALPIDE-2 for nine different distances (a range of 10cm). In each position, one million frames were taken.

3.13.1 Experimental setup

The source of X-rays is ⁵⁵Fe which is located in the base of a cylindrical copper cavern. A thin shell of Beryllium is used as a window. Fig 3.23 is a schematic representation of the X-ray encapsulation, where the high of the cylinder is 5 mm, and the red region corresponds to ⁵⁵Fe with a diameter of 10 mm.

To easily move the radioactive source; it was placed at the border of a PVC tube, which is held by a one direction movement structure. It can be moved by hand to locate it at the position indicated by a millimeter ruler. The X-rays which arrive at the pALPIDE-2 can

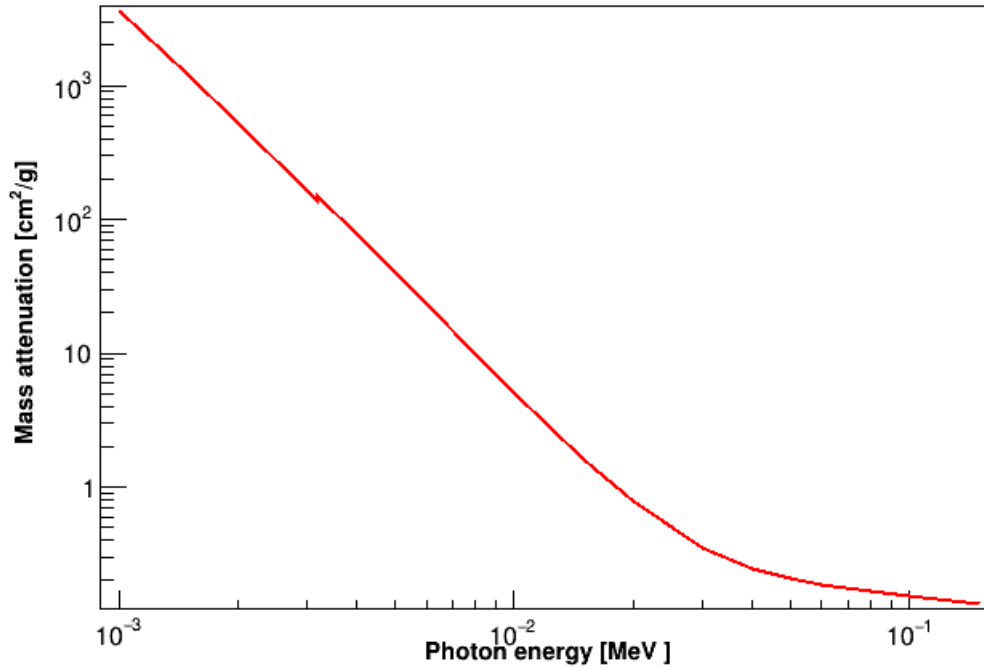


Figure 3.22: Mass attenuation coefficient of air as function of the photon energy. Image obtained from [79].

generate hits that are registered by the computer through the data acquisition system. Fig. 3.24 shows a schematic view of the setup.

The initial conditions configuration of the pALPIDE-2 sensor are ITH=51 ADC, VCASN=57 ADC and STROBELLENGTH = 10 CLK (0.25 μ s). The activity of the source at the time of the test was 28.7 MBq. The source can be moved along the z-axis and its projection crosses the center of the sensor. The movement covers nine positions (from 1 to 10 cm) between the source and the sensor.

3.13.2 Data taking and analysis

At each z position, the hit count was taken and by its pixel identification, we determined to which sector it belonged. For a million frames, the hit count shows that each sector responds differently. The cumulative hits for each position in the four sectors are shown in Fig. 3.25. Sectors S1 and S2 properly responded at the flux reduction according to

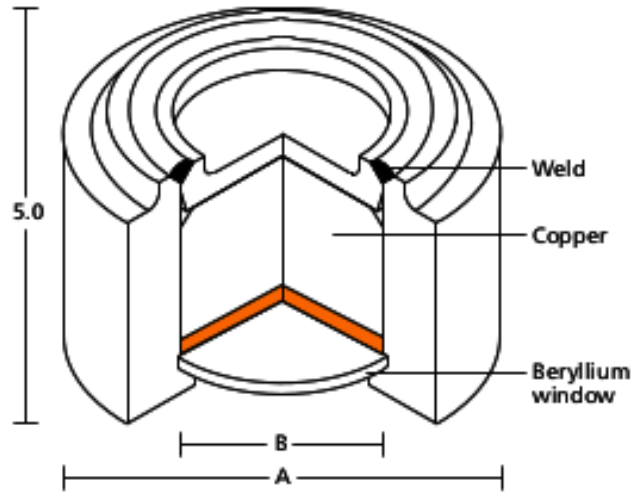


Figure 3.23: The geometry of the Fe^{55} source used for the test, image obtained from [80]

the inverse-square law with χ^2/dof : 11.51/7 and 11.48/7 respectively, using a $a + b/d^2$ fit, although their values do not represent a good fit. On the other hand, the S0 and S3 did not respond suitably. We found in sector 0 that the cumulative hits do not reduce significantly when the distance is increased. This characteristic could be associated with fake hits rate found in 3.12, whose rate is higher than in other sectors, as is found in [63] and also related with hot pixels. In case of sector 3, the fit function expresses a value of $\chi^2/dof = 27.4/7$, which does not represent a good fit. However, the hit count shows a decrease when the distance between source and sensor increases.

This test shows that despite the sensors have the same pitch, and the geometric difference in the collection region can induce different hit counts for x-rays energies of 5.9 keV.

After identifying and masking pixels, which active without any source (fake hits), we can guarantee the hits in each pixel are generated by X-rays. From these data in each sector, we re-plotted the cumulative hit and found a better fit for the inverse-square law. In sector 0, we found $x^2/ndf = 21.2/7$ instead of 144.4/7. Slightly improved fits were

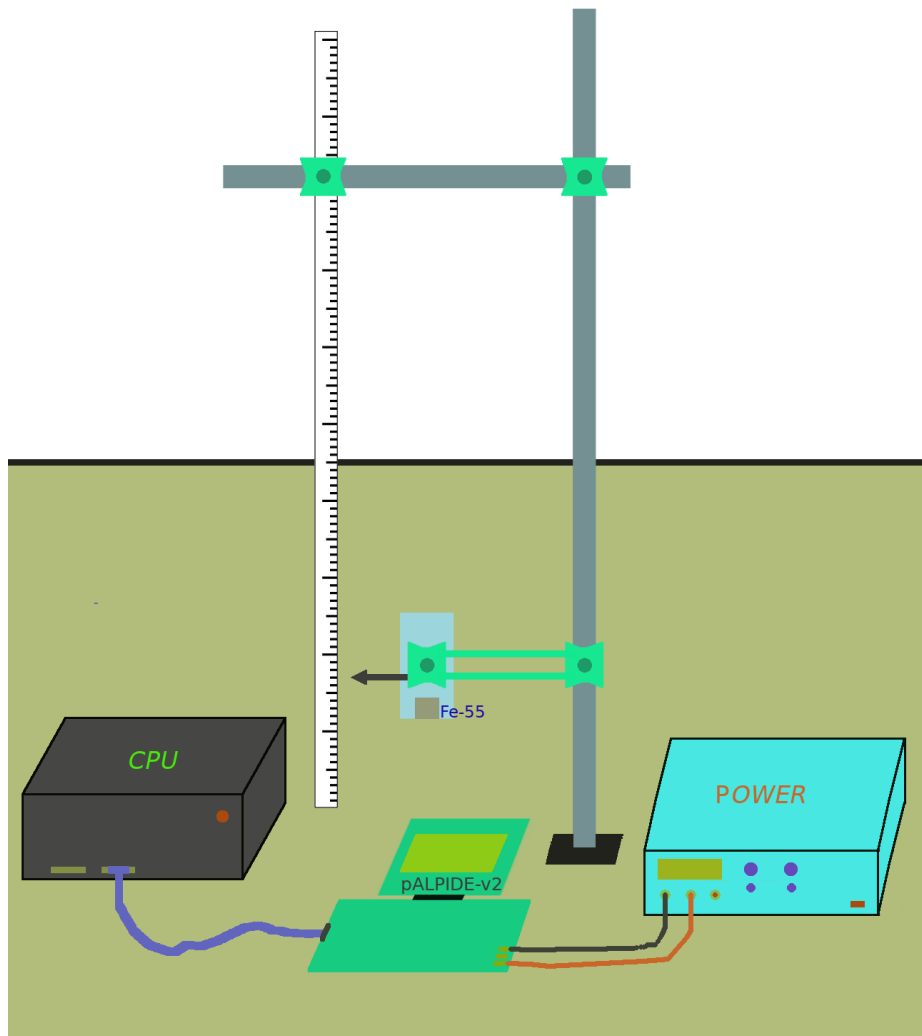


Figure 3.24: Experimental setup for the ^{55}Fe and the pALPIDE-2.

found for sectors 1 and 3, however not in sector 2, in which the counts show a small increase, as is shown in Fig. 3.26.

In order to compare the cumulative hits of the four sectors, normalization was done, as shown in Fig. 3.27, in which the four sectors showed a proper behavior. Also, sectors 1 and 2 had a similar response, indeed they had a better fit for the square inverse distance as is showed in 3.26. Sectors 0 and 3 showed fewer relative counts concerning other sectors when the distance is increased along the z -axis. Additionally, for a distance of 1 cm, sectors S0 and S3 did not receive the same amount of X-rays in comparison with S2 and

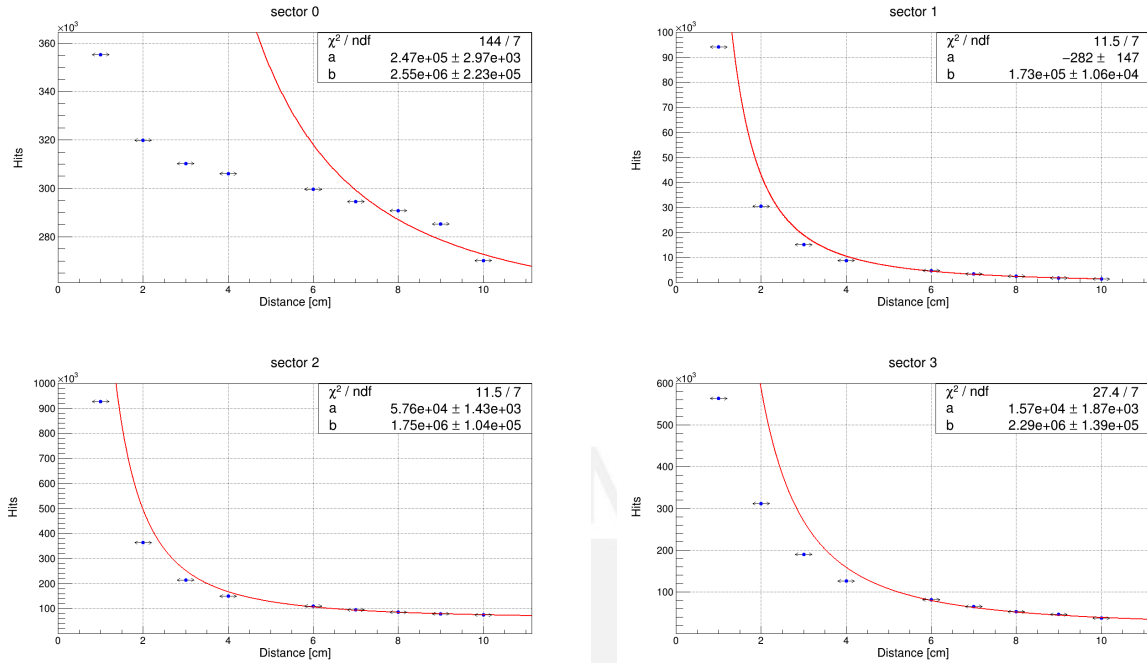


Figure 3.25: Cumulative hits generated by the X-ray source (^{55}Fe) for one million frames for different positions, and an inverse squared fit for the four sectors of pALPIDE-2.

S3. Indeed, the source is located at the projection center of the sensor, over S1 and S2.

In summary, this pALPIDE-2 has responded adequately to a different test. In digital and analogue scans, we found more than 200 pixels that did not respond appropriately. The mean threshold has a different value for each sector, greater for pixels with more spacing. The decrease in intensity of the x-ray with the square inverse was evidenced better by masking pixels with fake hits.

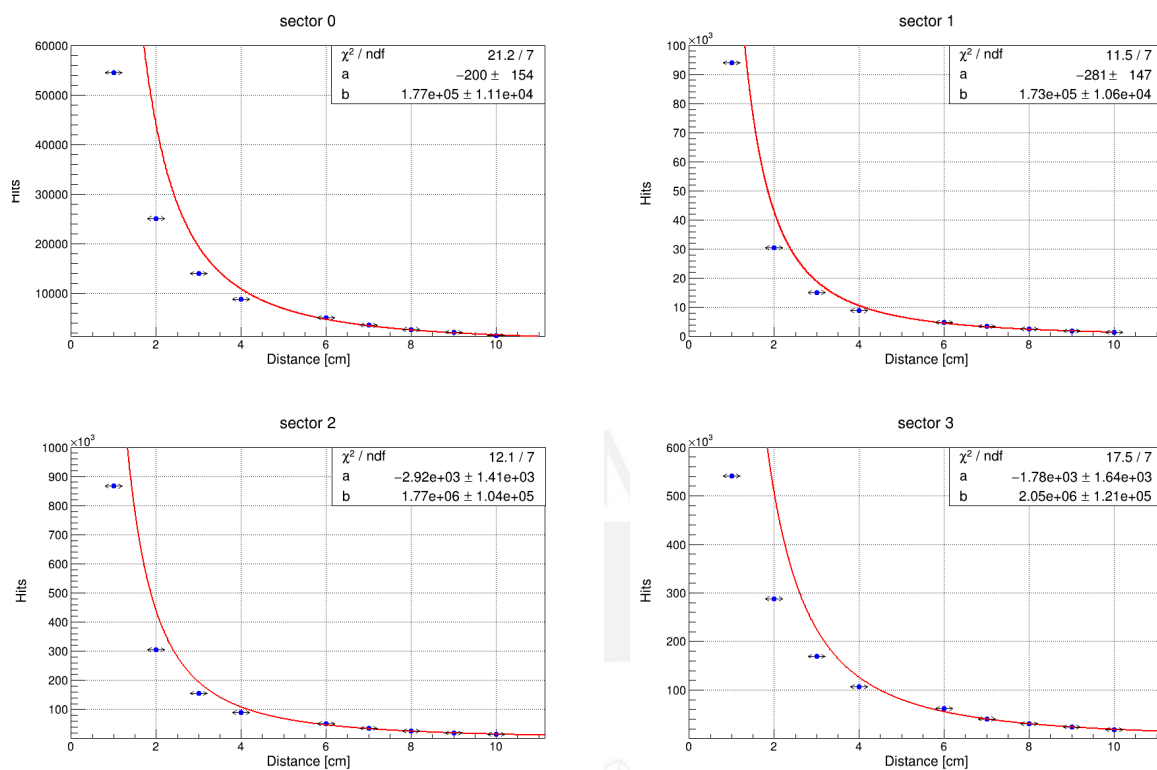


Figure 3.26: Cumulative hit generated by ^{55}Fe excluding hits generated by noise and hot pixels. An inverse squared fit for each sector of pALPIDE-2

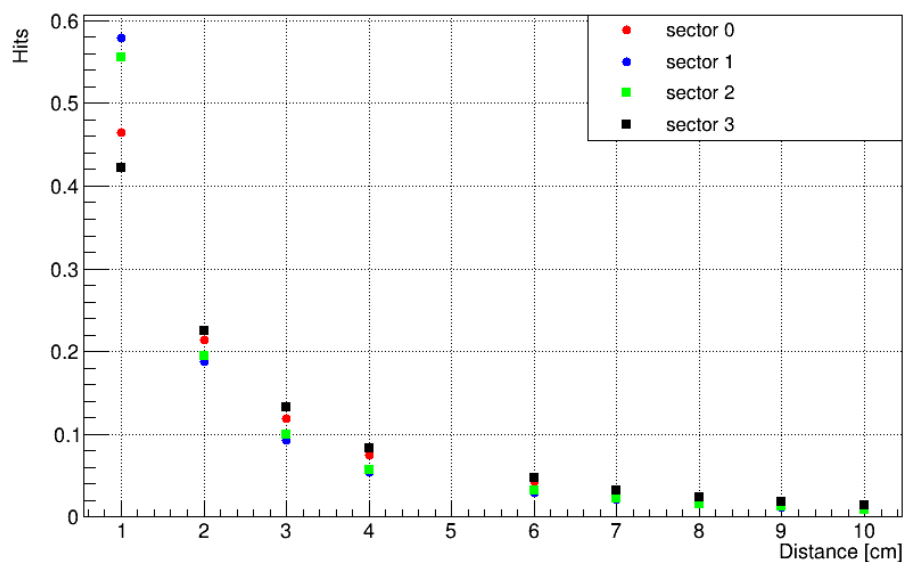


Figure 3.27: Cumulative hit normalized for the four sectors of pALPIDE-2 when exposed to a Fe-55 at different distances.

Chapter 4

Laser characterization with a CMOS sensor.

One of our goals was to study the response of individual pixels of the pALPIDE-2 when it is radiated by a pulsed laser, with a beam smaller than pixel pitch ($28\mu\text{m}$).

For that, we needed to set the beam diameter to less than $28\mu\text{m}$. Initially, we worked with a compact pulsed Nd:YAG laser of the Quantel CFR-200 family. The laser emits simultaneously at 532 nm and 1024 nm, green and infra-red, respectively with an energy range up to 200 mJ, and with beam diameter between 3 and 6 mm [81].

The next step was the reduction of the beam diameter up to less than $28\mu\text{m}$ by a optic system. To guarantee the reduced beam according to our requirement, we needed a device to characterize the beam size.

The costs of sensors to characterize laser beams are over \$ 2000. For this reason, we decided to implement an affordable tool to measure laser beams size, which guarantees high resolution with a commercial CMOS sensor (webcam). The cost of this tool is around \$ 308, and basically, it is based on a CMOS sensor and a Raspberry Pi 3B. All information about this tool can be found in this article [96]. We could measure the radii of a laser beam less than the pixel pitch of the pALPIDE-2 ($28\mu\text{m}$).

4.1 The laser

The laser (Light Amplification by Stimulated Emission of Radiation) is a source of radiation. There are different kinds of lasers. They can be classified according to the active medium as a gas in which helium-neon and CO₂ are more common, in solid state, neodymium-YAG (yttrium aluminum garnet), and semiconductor or diode laser. Lasers are also classified by their emission duration such as continuous and pulsed lasers. It is known that lasers have many applications in medicine [82], industry and science [83]. After laser invention, many techniques to analyze and characterize the beams have been developed [84].

In this section, we want to show a precise and affordable process for measuring the radius of a laser beam.

4.1.1 Transverse Electromagnetic Mode of a laser

The TEM (Transverse Electromagnetic Mode) is an electromagnetic field pattern in the transverse plane of propagation direction and describes the intensity distribution along the cross section beam. The lowest order of TEM is related to a Gaussian field distribution. Its transverse electric field can be expressed in cylindrical coordinates by [85]:

$$E(\rho, z) = E_0 \frac{w_0}{w(z)} e^{-\frac{\rho^2}{w^2(z)}} \quad (4.1)$$

where E_0 is the amplitude, ρ ($\rho = \sqrt{x^2 + y^2}$) is a radial distance in the transverse plane, $w(z)$ is the radius of the spot of the beam which varies along the propagation direction, and w_0 is the minimum radius, also is known as the radius of the waist¹ as is shown in Fig. 4.1.

¹The smallest diameter of the beam along its propagation.

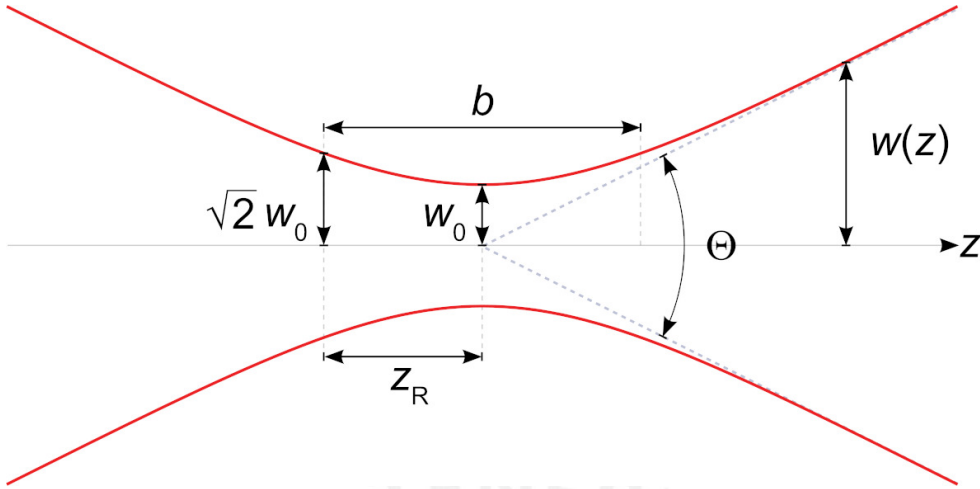


Figure 4.1: The width of the Gaussian beam varies according to the axial distance, and w_0 is the radius of the waist. Image obtained from [98].

Light sensors measure the intensity of a beam instead of the electric field. Since the intensity of a wave is proportional to its electric field squared, and the intensity at any arbitrary distance z' can be written as [85] :

$$I(\rho, z') = I_0 \frac{w_0^2}{w^2(z')} e^{-\frac{2\rho^2}{w^2(z')}} \quad (4.2)$$

where $I_0 = \frac{\epsilon_0 c E_0^2}{2}$ is the maximum intensity value, which generally takes place at the center of the beam. In the transverse plane, the intensity decreases from the center to edge of the beam.

As mentioned before, the laser beam and its spot size is a function of its propagation distance. The spot size of a Gaussian beam is defined as a fraction of the beam, where its radius $\rho(z) = w(z)$. At this point the intensity decreases up to $1/e^2$ of its maximum value. The spot of a Gaussian beam is shown in Fig. 4.2 for an arbitrary z' . The energy inside this circle of radius $w(z)$ (Gaussian radius) contains 86.5% of the total energy [86].

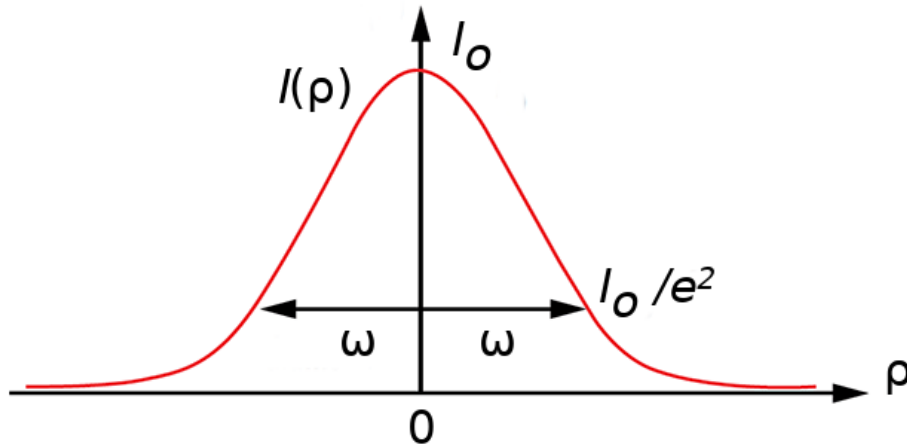


Figure 4.2: The Gaussian intensity profile of a laser beam.

The spot of the beam along its propagation can be expressed by [87]:

$$w(z) = w_0 \sqrt{1 + \left(\frac{z - z_0}{z_R}\right)^2} \quad (4.3)$$

where w_0 is the radius of the minimum spot of the beam which takes place at a position z_0 (the beam waist position), z_R is the Rayleigh length, at this length the radius of the spot increases up to $\sqrt{2}$ in its value ($w(z_R) = \sqrt{2}w_0$). Inside this range the spot does not suffer extreme changes, and it is expressed by [87]:

$$z_R = \frac{\pi w_0^2}{\lambda} \quad (4.4)$$

where λ is the wavelength of the light. For distances z greater than z_R the cross section of the beam increases linearly, which is known as the angular divergence of the beam and is expressed by [88]:

$$\theta_d = \frac{\lambda}{\pi w_0} \quad (4.5)$$

To characterize a Gaussian laser beam, first we have to measure the spot size in different z positions. Then the data obtained are compared to locate the waist of the

beam and the angular divergence.

4.2 Experimental Setup

We measured the spot size of two lasers with three different light sensors, which are a CMOS sensor, a photodiode, and a light dependent resistor (LDR) using two methods [96]. The first method is called the knife method [84] (it is an established technique to determine the profile of light beams) using two sensors: a photodiode and LDR. The second method is capturing frames (photos) with a CMOS sensor. Both methods measured the intensity of the light.

The laser is located at a fixed height, ensuring that the beam propagation was parallel to the z-axis. A movement system was implemented, which is driven by a stepper motor (it also acts as a support for the sensors). It can move the sensor along the y-axis with a minimum step of $10.10 \pm 5.05 \mu\text{m}$, which is guaranteed by a computer-controlled mechanical horizontal movement. To manage the vertical movement, we used a micrometer shifter which is manually controlled with a resolution of $10 \pm 5 \mu\text{m}$. In addition, we used an intensity attenuator to avoid the saturation of the sensors. The intensity was reduced to 0.1% of the incident beam. The attenuator is a rectangular step variable metallic neutral density filter, which provides a discrete range of optical densities. More information about the attenuator; can be found in [89]. Additionally, a pinhole located at a fixed position is used as an iris diaphragm in order to eliminate aberrations on the cross section beam. The data acquisition and the motor movement are managed with a Raspberry Pi 3B. The Fig. 4.3 represents the experimental setup.

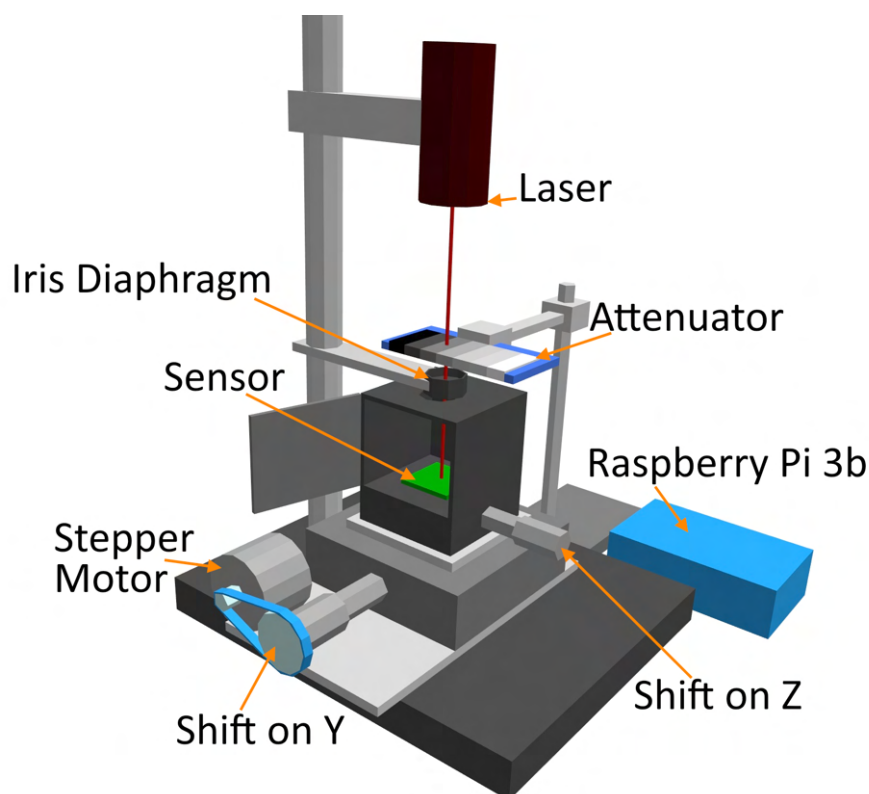


Figure 4.3: Schematic representation of the experimental setup. Image obtained from [96].

The following section describes the three sensors used in this characterization.

4.2.1 Photodiode

The photodiode is the First Sensor PIN PD PS100-5 THD, which is a square semiconductor light sensor that covers an active area of $10 \text{ mm} \times 10 \text{ mm}$ [90]. The active area works according to the photovoltaic effect [91]. The procedure to identify the beam profile is by measuring the beam intensity concerning the position of the active area. The transverse movement will cause the beam to stop covering the entire active area, and the electrical signal over the sensor is decreasing; this process is known as the knife method [84].

The photodiode is connected in series with a variable resistance and the generated electrical analog signal is digitized by an Analog-Digital-Convert ADS1115. This digital signal is registered by a Raspberry Pi 3B for each position.

4.2.2 The Raspberry Pi Camera

The Raspberry Pi camera is an image sensor, a commercial webcam Omnivision 5647 based on CMOS technology (CMOS sensor) [92]. It has a matrix of 2592×1944 pixels with a pixel pitch of $1.4 \mu\text{m}$. The camera covers around $25 \times 24 \times 9 \text{ mm}$. It was controlled by a Raspberry and configured with an exposure time of $16 \mu\text{s}$, ISO=0, analog and digital gain of 1 in order to guarantee low noise. The frame has a image format YUV (Y =1-byte: intensity, UV: color code). This configuration lets the frame be captured with full resolution.

4.2.3 Light Dependent Resistor

The Light Dependent Resistor (LDR) or commercially known as a photo-resistor is a light sensor that is a semiconductor [91]. Increasing intensity of light over its active area shows an increase in its conductivity or fall in its resistance [91] [93]. The method to measure the spot of the beam is the same as used with the photodiode.

Also, the Raspberry Pi 3b managed the webcam. It controlled the photodiode and LDR. Fig. 4.4 is a schematic representation of the Raspberry and the connections of the light sensors.

4.2.4 Laser Type

In the experiment, we used two kinds of laser, and both of them are Gaussian beam lasers according to their datasheets [94][95]. The first is a semiconductor green laser of 532 nm with power up to $\sim 5 \text{ mW}$ which can be manually regulated. It is made by the laserglow technology [94]. The second is a Helium-Neon gas laser manufactured by Lumentum that emits a fixed power $< 5 \text{ mW}$ with a wavelength of 632.8 nm (red). The divergence in this gas laser is 1.7 mrad that expresses low variation on the beam size through its propagation. More information and characteristic about this laser in [95].

We determined the spot size of both lasers. However, we only searched for the waist of

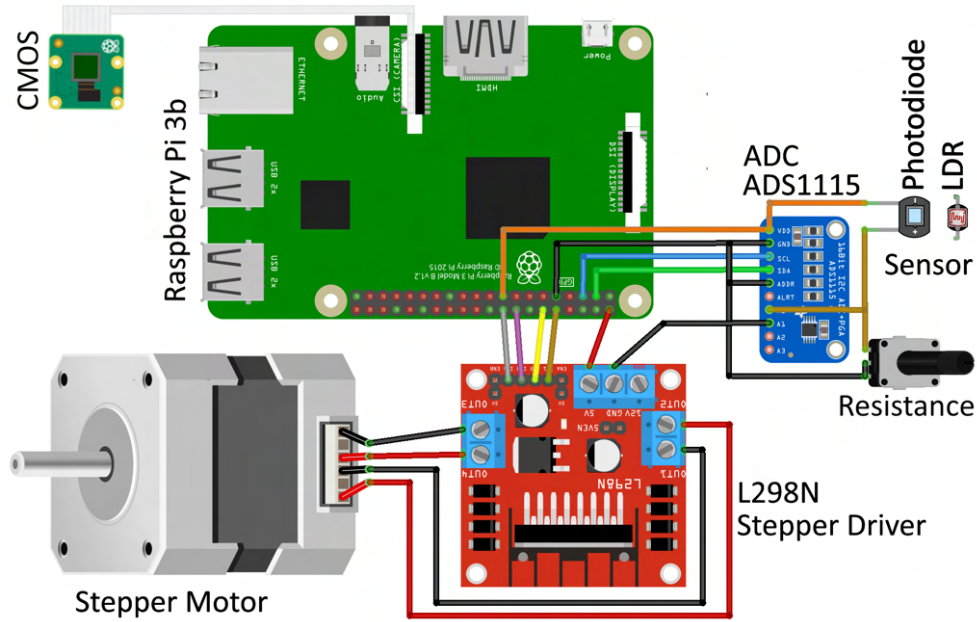


Figure 4.4: Raspberry board with electrical connection to the three light sensors: webcam, photodiode, and LDR. Image obtained from [96].

the semiconductor laser because it shows variation in its beam size. On the other hand, the quasi-stable beam (He-Ne gas laser) was used as a spot size patron to compare the measurements obtained with the three light sensors.

4.3 Measurements of the spot profile

After collecting the data from the three sensors, the data were fitted according to a Gaussian function. For the CMOS sensor, the pixels register information in ADC units, and the ADC is related to the intensity of the beam profile. One frame represents a 2D Gaussian intensity function. From this function, two projections are obtained, which are X and Y Gaussian intensity functions. In the case of the x projection, the equation used for the fitting is:

$$f(x) = \frac{A}{\sigma\sqrt{\pi}} e^{-\frac{(x-\mu)^2}{2\sigma^2}} + B \quad (4.6)$$

where A is a normalization value, and μ is the center position of the peak, B is the

background, and σ is the standard deviation. The radius of the spot is $w = 2\sigma$.

To find the waist of the green laser, we took ten frames in each one of the eleven different positions between the laser and the CMOS sensor in a range of 10 mm. From each position, we obtained an average radius ($w = 2\sigma$) of the spot. In this case, the total error for the radius is represented by: $\Delta_{total} = \sqrt{(\sum_i \Delta_i^2)/N}$ where $\Delta_i = \Delta\sigma_i + 0.5$, and $\Delta\sigma$ is the error from the Gaussian fit, the 0.5 represents the systematic error associated with number of pixels activated by the laser. N is the number of frames. Additionally, we converted the numbers of pixels aligned into length units by multiplying with $1.4 \mu\text{m}$ (pitch of the pixel).

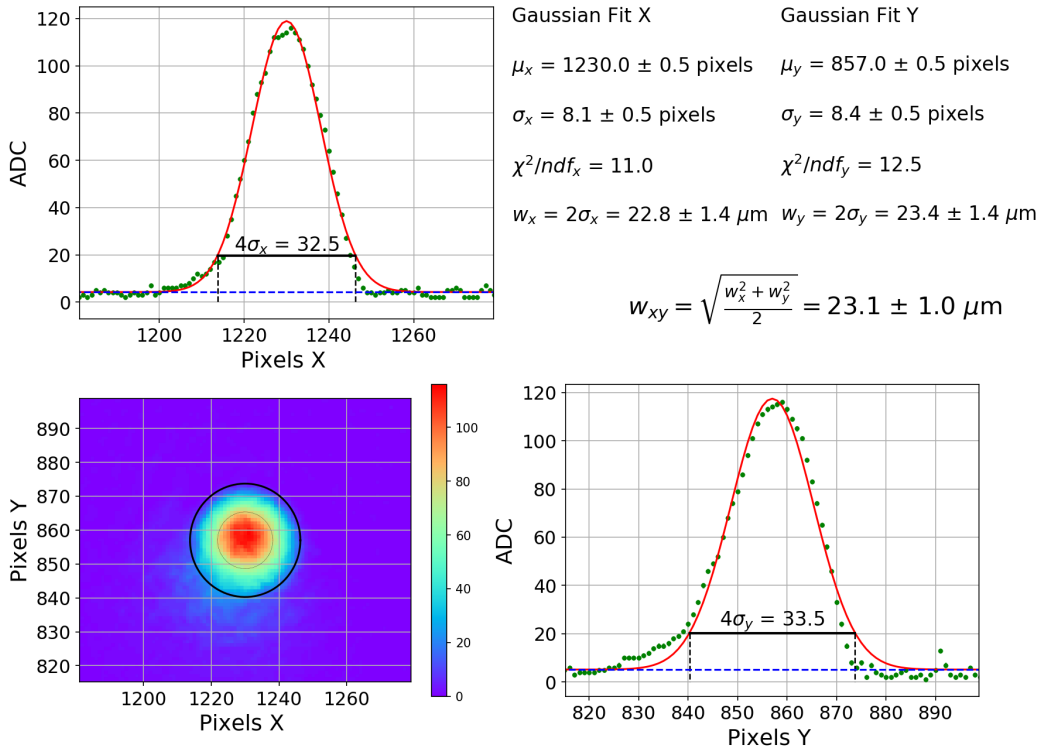


Figure 4.5: A frame of the laser beam, where the z-axis is the intensity in ADC units (bottom left), a Gaussian fit for the X-projection (top left), and a Gaussian fit for Y-projection (bottom right). Image obtained from [96].

For example, Fig. 4.5 is for one frame at the bottom leaf, in which a matrix of pixels with ADC unit is related to the beam intensity. From this, two Gaussian fits were made

for x and y projections at the top leaf and the bottom right, respectively. This fit gave the value of $\sigma_x = 8.1 \pm 0.5$ pixels and $\sigma_y = 8.4 \pm 0.5$ pixels ($\sigma = \sqrt{\sigma_x^2 + \sigma_y^2}$). Converting the number of pixels into units of distance, for this frame, the radius of the beam (w_{xy}) is $23.1 \pm 1.0 \mu\text{m}$.

From each z position, we obtained the average of ten measurements of the spot radius. The average of the radii (black dots) versus the z position is shown in Fig. 4.6 and 4.7 for the x and y axes, respectively. From these data, a quadratic fit was applied to obtain the waist of the beam propagation, independently for each axis. We found that, for the x-axis projection the radius at waist $w_{0x} = 20.7 \pm 0.6 \mu\text{m}$, a Rayleigh range $Z_{Rx} = 2415.3 \pm 117.4 \mu\text{m}$, and the angular divergence $\theta_x = 8.2 \pm 0.3$ mrad. For the y axis projection, we found the radius of the waist $w_{0y} = 23.7 \pm 0.9 \mu\text{m}$, a Rayleigh range $Z_{Ry} = 3583.3 \pm 291.1 \mu\text{m}$, with an angular divergence $\theta_y = 7.2 \pm 0.3$ mrad.

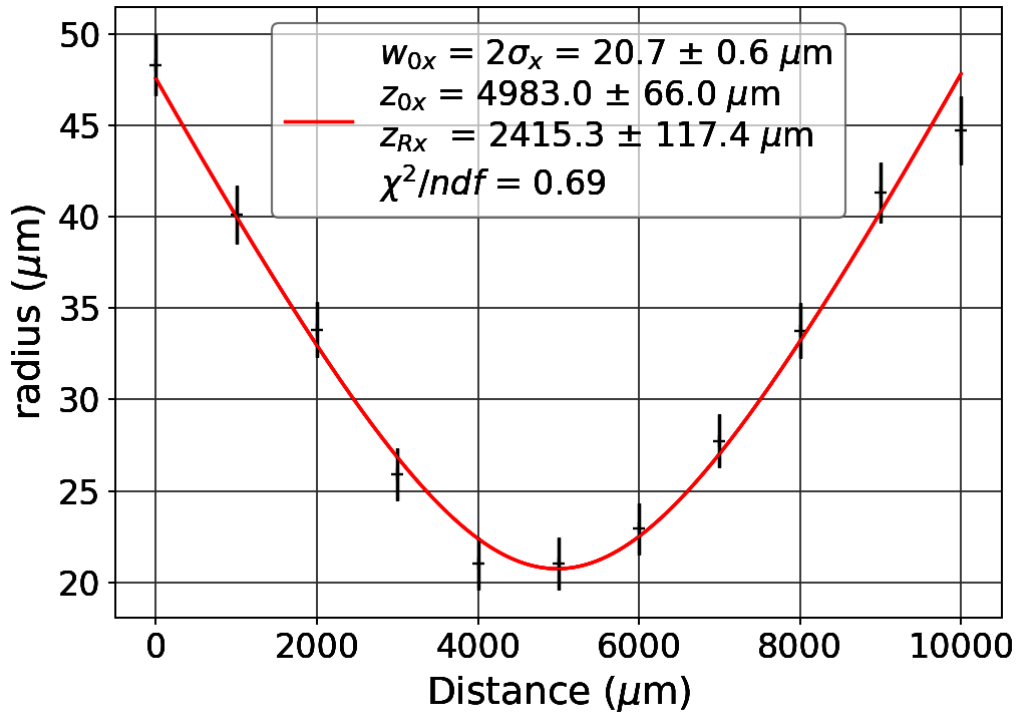


Figure 4.6: Variation of the x-radius beam in the function of axis propagation. Image obtained from [96].

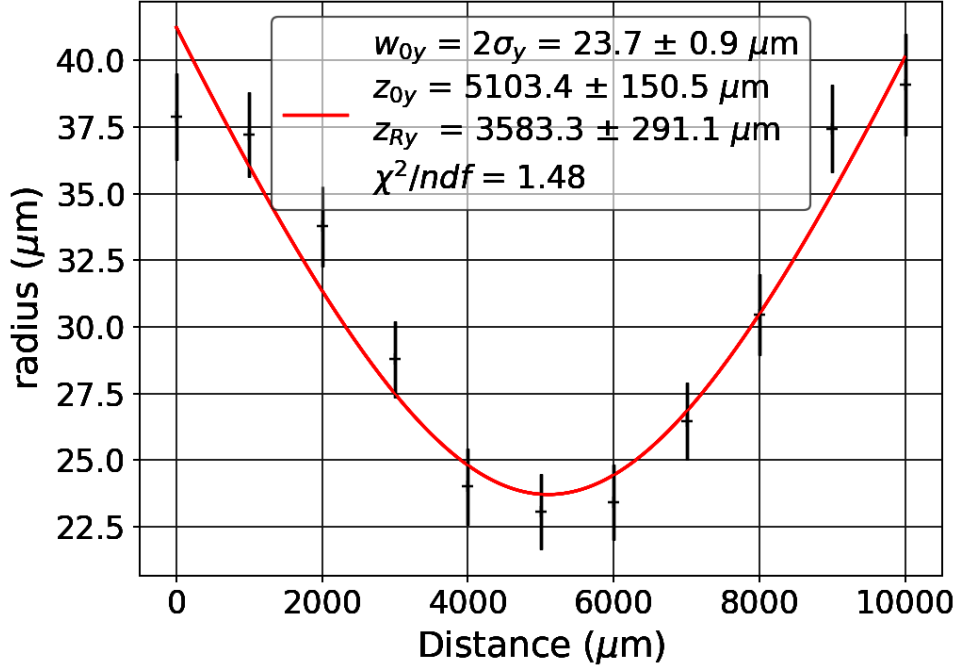


Figure 4.7: Variation of the y-radius beam in the function of axis propagation. Image obtained from [96].

There are few differences between the w_{ox} and w_{0y} , one reason for this is the rectangular cavity on the diode lasers [97]. However, it can be considered almost circular.

4.3.1 Measurements of the spot size using three different sensors

In this part, we compare the results of spot size measurement of the He-Ne gas laser obtained by three different sensors. They are CMOS, photodiode, and LDR. Keeping the same measurement condition for each sensor. The laser was located at a fixed position of 467.15 ± 0.05 mm above the sensors to avoid saturation. The intensity transmission selected was 0.1%.

The attenuator was fixed at an optical density equal to 3, which guarantees transmission of 0.1 % of the initial intensity, which allows the sensors to work properly, and avoid saturation on CMOS sensors. For this intensity, we took data and applied the same method (knife-technique) for the photodiode and LDR, where we use the minimum

transversal displacement along the y-axis was $10.1 \mu\text{m}$.

For the photodiode and LDR, we measured the output voltage. The procedure starts with the beam inside of the active area. Then, the sensor was moved step by step along the y-axis until the beam was out of the sensor. In each step position, ten voltage measurements were taken. From these voltages, their average value was saved.

The average voltages (amplitudes) versus position were plotted as shown in Fig. 4.8. A Gaussian cumulative distribution fit was made according to Eq. 4.7:

$$f(x) = \frac{A}{2} \left[1 + \operatorname{erf}\left(\frac{x - \mu}{\sigma\sqrt{2}}\right) \right] + B \quad (4.7)$$

where A is the maximum voltage which is related to the maximum intensity, μ is the position where the voltage is half of the maximum value, B is the background, erf is the standard error function, and σ the standard deviation ($w = 2\sigma$).

For the resistance of $2.2 \text{ k}\Omega$ (this value let to reduce errors in the measurement) in series with the photodiode, we obtained a spot radius of $w = 521.9 \pm 5.4 \mu\text{m}$. In addition, tests were done varying the distance between steps, in which the spot size did not show a significant variation in its value.

Similarly, we measured the radius of the spot with the LDR, and it did not show a significant variation in the size when the step length was changed. However, it showed a high variation in the spot size when the resistance value in the circuit was changed.

A disadvantage LDR sensor response to the laser beam is related to its small and zigzag active area, which can not contain the whole beam that will generate an error on the spot measurement of about 10%. For the resistance of 11.5Ω , which was connected in series to the LDR we found that the radius of the spot was $w = 486.9 \pm 54.1 \mu\text{m}$, which is near to the value obtained with the photodiode.

The measurement of the spot with the CMOS sensor using the method explained in 4.3.1 gave a radius of $w = 500.4 \pm 5.5 \mu\text{m}$.

To compare the measurements obtained from the three sensors, we selected the w_{CMOS}

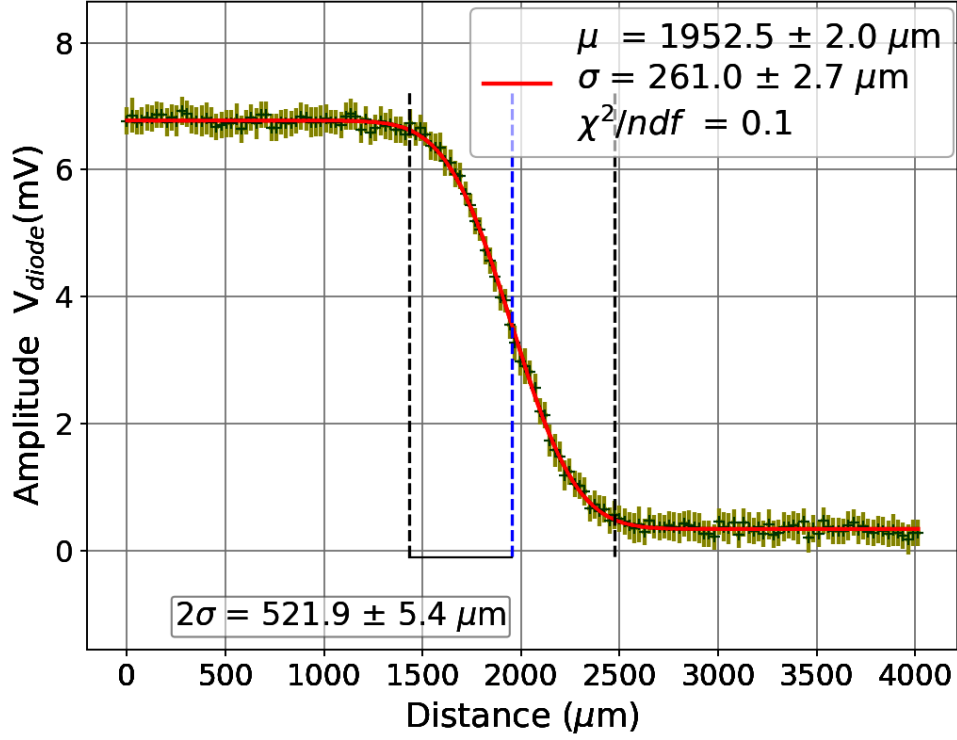


Figure 4.8: A Gaussian cumulative distribution fit for the voltage measurements of the photodiode as a function of the beam position with respect to the active area. Image obtained from [96].

value as a standard. The difference between the three spot radii can be expressed in terms of the number of standard deviations by:

$$n_\sigma = \frac{|w_{CMOS} - w_{sensor}|}{\sigma} \quad (4.8)$$

where w_{sensor} represents the radius measurement by the photodiode and LDR, and the σ is defined as:

$$\sigma = \sqrt{(\Delta w_{CMOS})^2 + (\Delta w_{sensor})^2} \quad (4.9)$$

Where, Δw_{CMOS} and Δw_{sensor} represent the radii errors measurement calculated for the CMOS sensor, and the photodiode/LDR. The comparison of the spot radius show compatibility in the measurements obtained with the CMOS sensor, the photodiode, and the LDR with less than 0.5σ as is shown in Table 4.1.

Table 4.1: Comparison of radii obtained from the CMOS sensor with the results from the photodiode and LDR

Sensor	$w(\mu m)$	η_σ
CMOS	500.4 ± 5.5	
Photodiode	480.8 ± 56.7	0.4
LDR	486.9 ± 54.1	0.3

According to our results, we can see that the CMOS sensor has the highest precision method for beam profiling. The error in the minimum spot radius is 2.9%, 3.8% for the x and y axes, respectively. Thus, it is a good tool to determine beam characteristics with acceptable precision.

4.4 Comparing prices of sensors

There are many commercial (including CMOS and CCD) devices to measure and characterize a laser beam of which their prices are over \$2000. These devices guarantee a characterization of laser with beam grater than $20 \mu s$, also more of them respond properly from 350 to 1100 nm as is shown in the Table 4.2. The cost of the tool that we made is \$ 308 which is very low in comparison with commercial devices.

Table 4.2: Commercial devices to measure a laser beam size

Sensor	Price (\$)	Response (nm)	pixel pitch (μm)	Total active area (mm^2)	Beam minimum diameter (μm)
Omni Vision	308	350-1000	1.4	3.7×2.7	21
WinCamD-XHR-1/2" [99]	2750	355-1150	3.2	6.5×4.9	32
CinCam CMOS 1204 [100]	2860	400-1150	2.2	5.7×4.3	22
CCD BC106N-VIS [101]	4648	350-1100	6.45	9.0×6.7	20

The minimum beam diameter that the tool we made can measure is over $21 \mu m$ which could have allowed us to characterize the infra red (1024 nm) laser for the study of the response of the pALPIDE-2 pixels when is irradiated.

We could not test a response of a single pixel of pALPIDE-2 when it is irradiated with a laser beam smaller than its pixel pitch because the sensor was broken in the laboratory during the setup implementation.

Chapter 5

Conclusions

In this thesis, we describe the upgrade program of the ALICE experiment, emphasizing the characteristics and advantages of one of its new detectors, called Muon Forward Tracker. This detector has been installed in December of 2021 and the data has started its operations for Run 3 in June of 2022. The MFT is implemented with sensors called ALPIDE, which are a kind of Monolithic Active Pixel Sensor. We explain the characteristics and operation modes of the MFT. Before the final design of the ALPIDE, some prototypes were made as the pALPIDE-1/2/3 to study and improve its data taking, efficiency and power consumption.

As part of this study, we made several tests on the pALPIDE-2 as the digital, threshold, and analog scans to characterize the sensor which has four types of pixels. In the part of characterization, even though the same pitch size, we found that the threshold value depends on the geometrical configuration in the pixel input, greater space between the n-well and p-well showed higher threshold values. Also, we verified the direct dependence of the threshold with the current ITH. A digital test showed a group of pixels (more than 200) does not work correctly.

This sensor was also exposed to a soft X-ray radioactive source, Fe-55, to analyze its response. The distance variation between X-ray radioactive source and pALPIDE-2 shows that the hits counts vary with the inverse square with a reasonable adjustment.

In addition, we collaborated with the implementation of two non-sensitive geometric parts of the MFT into the new O2 system. We implemented these geometric elements according to their blueprints, which are the Half-Cone and the Patch-Panel. The Half-Cone acts as a support of the MFT, and the Patch-Panel carries the data concentrator.

Additionally, in the way to study the behaviour of a single pixel of the pALPIDE-2 when it is exposed to a pulsed infrared laser, we designed an affordable tool to characterize a Gaussian laser beam. This tool was implemented with a Raspberry and a CMOS webcam as a sensor. Two other sensors were used in the measurement of the laser spot size to compare their results.

The spot size measurements were made with a photodiode, light-dependent resistor, and CMOS sensor. Comparing their results show that the lower significance error corresponds to the CMOS sensor. Indicating it is a very efficient tool to characterize lasers beam. Also, it is an affordable system that was automatized.

Bibliography

- [1] H. R. Schmidt and J. Schukraft, "The physics of ultra-relativistic heavy-ion collisions". J. Phys. G 19, 1705 (1993). <https://doi.org/10.1088/0954-3899/19/11/006>
- [2] I. Arsene et al. [BRAHMS Collaboration] "Quark–gluon plasma and color glass condensate at RHIC? The perspective from the BRAHMS experiment". Nucl. Phys. A 757, 1 (2005) <https://doi.org/10.1016/j.nuclphysa.2005.02.130>.
- [3] J. Schukraftthe, ALICE Collaboration et al, "First Results from the ALICE experiment at the LHC," Nucl. Phys. A 862-63 (2011) 78-84, <https://doi.org/10.1016/j.nuclphysa.2011.05.023>
- [4] ALICE collaboration, "Technical Design Report for the Muon Forward Tracker", CERN-LHCC-2015-001; ALICE-TDR-018 (2015). <https://cds.cern.ch/record/1981898>
- [5] Johann Rafelski and Jeremiah Birrell, "Traveling Through the Universe: Back in Time to the Quark-Gluon Plasma Era" 2014 J. Phys.: Conf. Ser. 509 012014 <https://doi.org/10.1088/1742-6596/509/1/012014>
- [6] Expansion of the universe, http://www-alice.gsi.de/fsp201/qgp/hist_univ.gif
- [7] Wells, James, 2020, 51-69, "The Once and Present Standard Model of Elementary Particle Physics" https://doi.org/10.1007/978-3-030-38204-9_2

- [8] Butterworth J. M. 2016 "The Standard Model: How far can it go and how can we tell?". *Phill. Trans. R. Soc. A.* 374:20150260. <https://doi.org/10.1098/rsta.2015.0260>. 2016
- [9] CERN Document Server. <https://cds.cern.ch/record/1473657> 2022.
- [10] G. Martínez, (2013) "Advances in Quark Gluon Plasma", arXiv: Nuclear Experiment, <https://arxiv.org/pdf/1304.1452.pdf>
- [11] M. Tanabashi et al. (Particle Data Group) "Review of Particle Physics" *Phys. Rev. D* 98, 030001 – Published 17 August 2018. <https://pdg.lbl.gov/>
- [12] Halzen, F. and Martin, Alan D, "QUARKS AND LEPTONS: AN INTRODUCTORY COURSE IN MODERN PARTICLE PHYSICS" isbn :978-0-471-88741-6, 1984.
- [13] I. Bautista, C. Pajares, and and J. Ramírez, "String percolation in AA and p+p collisions", *Rev. Mex. Fís.*, vol. 65, no. 3 May-Jun, pp. 197–223, May 2019. <https://doi.org/10.31349/RevMexFis.65.197>
- [14] Fukushima, Kenji and Hatsuda, Tetsuo, "The phase diagram of dense QCD", 2010. [arXiv:1005.4814 [hep-ph]], <https://doi.org/10.1088/0034-4885/74/1/014001>.
- [15] Haque, Najmul. "Some Applications of Hard Thermal Loop Perturbation Theory in Quark Gluon Plasma" 2014 [arXiv:1407.2473 [hep-ph]] <https://inspirehep.net/literature/1305436>
- [16] Baym, Gordon and Hatsuda, Tetsuo and Takatsuka, Tatsuyuki, 2018, "From hadrons to quarks in neutron stars: a review". United States: N. p., <http://doi.org/10.1088/1361-6633/aaae14>
- [17] R. Pasechnik and M. Šumbera, "Phenomenological Review on Quark-Gluon Plasma: Concepts vs. Observations". *Universe* 2017, 3(1), 7; <https://doi.org/10.3390/universe3010007>. 2017

- [18] ALICE Collaboration. "Charged-particle multiplicity and transverse energy in Pb–Pb collisions at $\sqrt{s_{NN}} = 2.76$ TeV with ALICE". *J.Phys.G* 38 (2011) 124040. <https://doi.org/10.1088/0954-3899/38/12/124040>
- [19] Cristina Bedda. "The ALICE experiment: D^+ -meson production in heavy-ion collisions and silicon low noise sensors characterization for the ITS Upgrade". PhD thesis. CERN-THESIS-2016-263: Turin 2016 <https://cds.cern.ch/record/2255649/files/>
- [20] Prashant Shukla. "Glauber model for heavy ion collisions from low energies to high energies". In: (2001). <https://arXiv.org/abs/nucl-th/0112039>
- [21] cerncourier, 2013, "Participants and spectators at the heavy-ion fireball" <https://cerncourier.com/a/participants-and-spectators-at-the-heavy-ion-fireball> arXiv:nucl-th
- [22] H. Wang, "Study of particle ratio fluctuations and charge balance functions at RHIC" [Ph.D. thesis], Michigan State University, 2013, <http://arxiv.org/abs/1304.2073>.
- [23] J. Schukraft. "Heavy ion physics at the Large Hadron Collider: what is new? What is next?" In: *Phys. Scripta* T158 (2013), p. 014003. <https://doi.org/10.1088/0031-8949/2013/T158/014003>.
- [24] James D Bjorken. "Highly relativistic nucleus-nucleus collisions: The central rapidity region". In: *Physical review D* 27.1 (1983), p. 140
- [25] R.Sahoo, "Relativistic Kinematics" 2016 [<https://arXiv.org/abs/1604.02651> [nucl-ex]].
- [26] Monnai, Akihiko, "Prompt, pre-equilibrium, and thermal photons in relativistic nuclear collisions", *Journal of Physics G, Nuclear and Particle Physics*, 47(7), 14. (2020) <http://dx.doi.org/10.1088/1361-6471/ab8d8c>.

- [27] Akihiko Monnai. "Effects of quark chemical equilibration on thermal photon elliptic flow". 2015 J. Phys.: Conf. Ser. 612 012026. <https://doi.org/10.1088/1742-6596/612/1/012026>
- [28] G. Bencedi. 09-2016 "Nuclear modification factor of charged particles and light-flavour hadrons in p-Pb collisions measured by ALICE" [<https://arxiv.org/abs/1609.05665>] [nucl-ex]
- [29] Baoyi Chen, et al. 2919 "Probe the tilted Quark-Gluon Plasma with charmonium directed flow" <https://doi.org/10.1016/j.physletb.2020.135271>
- [30] P. Braun-Munzinger and J. Stachel, (Non)Thermal Aspects of Charmonium Production and a New Look at J/ψ Suppression. Phys.Lett. B490, 196 (2000), [arXiv:nucl-th/0007059], [http://dx.doi.org/10.1016/S0370-2693\(00\)00991-6](http://dx.doi.org/10.1016/S0370-2693(00)00991-6)
- [31] Mateu Vicent, G. Ortega, Entem D., Fernandez Francisco. (2019) "Calibrating the naive Cornell model with NRQCD" The European Physical Journal C. 79. 10.1140/epjc/s10052-019-6808-2. <https://doi.org/10.1140/epjc/s10052-019-6808-2>
- [32] Rajeev S. Bhalerao. "Relativistic Heavy-Ion Collisions". arXiv:1404.3294 [nucl-th]. <https://doi.org/10.48550/arXiv.1404.3294>
- [33] L. Evans and P. Bryant. "LHC Machine". In: JINST 3 (2008), S08001. <https://doi.org/10.1088/1748-0221/3/08/S08001>.
- [34] Jowett, John M. and Schaumann, Michaela, "Overview of Heavy Ions in LHC Run 2", 9th LHC Operations Evian Workshop 2019. <https://cds.cern.ch/record/2750273>
- [35] <https://people.ece.uw.edu/hauck/LargeHadronCollider/> (2022).

- [36] The ALICE Collaboration. "The ALICE experiment at the CERN LHC". In: JINST 3 (2008), S08002. doi:<https://dx.org/10.1088/1748-0221/3/08/S08002>.
- [37] Bruce, Roderik and Argyropoulos, Theodoros and Bartosik, Hannes and De Maria, Riccardo and Fuster Martinez, Nuria and Jebrancik, Marc Andre and Jowett, John and Mounet, Nicolas and Redaelli, Stefano and Rumolo, Giovanni and Schaumann, Michaela and Timko, Helga "HL-LHC operational scenarios for Pb-Pb and p-Pb operation" CERN-ACC-2020-0011. Geneva 2020 <https://cds.cern.ch/record/2722753>.
- [38] ALICE Collaboration, "The ALICE Transition Radiation Detector: construction, operation, and performance. The ALICE Transition Radiation Detector: construction, operation, and performance". CERN-EP-2017-222. <https://cds.cern.ch/record/2281131>.
- [39] ALICE Collaboration, "Technical Design Report for the Upgrade of the ALICE Inner Tracking System" [CERN-LHCC-2013-024] (2013) [ALICE-TDR-017]. <https://doi.org/10.1088/0954-3899/41/8/087002>
- [40] B Abelev et al and The ALICE Collaboration, 2014. "Upgrade of the ALICE Experiment: Letter Of Intent", J. Phys. G: Nucl. Part. Phys. 41 087001 <https://doi.org/10.1088/0954-3899/41/8/087001>
- [41] J. Alme, et al, "The ALICE TPC, a large 3-dimensional tracking device with fast readout for ultra-high multiplicity events" <https://doi.org/10.1016/j.nima.2010.04.042>
- [42] Gros, Philippe, 2011, "Identifying Charged Hadrons on the Relativistic Rise Using the ALICE TPC at LHC2, CERN-THESIS-2011-036,<http://cds.cern.ch/record/1362724>

- [43] T. L. Karavicheva on behalf of the ALICE Collaboration, 2017. "The Fast Interaction Trigger detector for the ALICE Upgrade" <http://dx.doi.org/10.1088/1742-6596/798/1/012186>
- [44] E. Garcia, et al, "Perspectives of the ALICE Experiment and Detector Upgrade" <https://doi.org/10.1016/j.nuclphysbps.2015.10.134>
- [45] ALICE Collaboration, 2019, "Muon physics at forward rapidity with the ALICE detector upgrade", NUCLEAR PHYSICS A. V-982 947- 950. <http://dx.doi.org/10.1016/j.nuclphysa.2018.10.034>
- [46] ALICE collaboration, "Addendum of the Letter of Intent for the upgrade of the ALICE experiment : The Muon Forward Tracker". CERN-LHCC-2013-014, LHCC-I-022-ADD-1. <https://cds.cern.ch/record/1592659>.
- [47] twiki.cern, 2020, <https://twiki.cern.ch/twiki/bin/view/ALICE/MFTWP4>
- [48] ALICE Collaboration, 2005, "ALICE technical design report of the computing", CERN-LHCC-2005-018, <https://cds.cern.ch/record/832753/files/ALICE-TDR-012.pdf>
- [49] ALICE collaboration, "Technical Design Report for the Upgrade of the Online-Offline Computing System", CERN-LHCC-2015-006. ALICE-TDR-019 (2015) <https://cds.cern.ch/record/2011297>
- [50] <http://www-subatech.in2p3.fr>
- [51] R. Turchetta "CMOS Monolithic Active Pixel Sensors (MAPS) for future vertex detectors" Journal of Instrumentation. 1. 2006, <https://doi.org/10.1088/1748-0221/1/08/p08004>.
- [52] K. Nakamura. Review of Particle Physics". In: J. Phys. G 37.7A (2010), p. 075021. <https://doi.org/10.1088/0954-3899/37/7A/075021>

- [53] L. Landau. "On the energy loss of fast particles by ionization". In: J. Phys.(USSR) 8 (1944), pp. 201–205.
- [54] H. Bichsel. "Straggling in thin silicon detectors". In: Rev. Mod. Phys. 60 (3 1988), pp. 663–699. doi: 10.1103/RevModPhys.60.663. <https://doi.org/10.1103/RevModPhys.60.663>
- [55] W. R. Leo "Techniques for Nuclear and Particle Physics Experiments". Printed 1987 http://tesla.phys.columbia.edu:8080/eka/William_R_Leo_Techniques_for_nuclear_and_partic.pdf
- [56] E. R. Fossum, 1997 "CMOS Image Sensors: Electronic Camera On A Chip", IEEE Transactions on Electron Devices <https://doi.org/10.1109/16.628824>
- [57] J. W. van Hoorne. "Study and Development of a Novel Silicon Pixel Detector for the Upgrade of the ALICE Inner Tracking System". PhD thesis. CERN-THESIS-2015-255: TU Wien, 2015. <https://cds.cern.ch/record/2119197>.
- [58] L. Rossi et al. "Pixel detectors: From fundamentals to applications". Springer, 2006. <https://doi.org/10.1007/3-540-28333-1>.
- [59] Raskina, Valentina & Křížek, Filip. (2019). Characterization of Highly Irradiated ALPIDE Silicon Sensors. Universe 2019. 5. 91. <https://doi.org/10.3390/universe5040091>.
- [60] R. L. Boylestad. "Electronic devices and circuit theory". Printed 2013 Eleventh Edition. <http://www.rtna.ac.th/departments/elect/Data/EE306/Electronic/20Devices/20and/20Circuit20Theory.pdf>
- [61] G. S. Aglieri et al., "Monolithic active pixel sensor development for the upgrade of the ALICE Inner Tracking System", 2013 JINST 8 C12041. <https://doi.org/10.1088/1748-0221/8/12/C12041>

- [62] p. Yang et al.,(2015) " MAPS development for the ALICE ITS upgrade", Journal of Instrumentation, 10(03), C03030. <https://doi.org/10.1088/1748-0221/10/03/C03030>
- [63] D. Kim et al. (2016) "Front end optimization for the monolithic active pixel sensor of the ALICE Inner Tracking System upgrade" <https://doi.org/10.1088/1748-0221/11/02/C02042>
- [64] P. Yang et al., 2015 "Low-power priority Address-Encoder and Reset-Decoder data-driven readout for Monolithic Active Pixel Sensors for tracker system", Nucl. Instrum. Meth. A 785 61 <https://doi.org/10.1016/j.nima.2015.02.063>
- [65] ALICE collaboration, G. Aglieri Rinella et al., 2027. "The ALPIDE pixel sensor chip for the upgrade of the ALICE Inner Tracking System". <https://doi.org/10.1016/j.nima.2016.05.016>
- [66] E. Belau et al. "Charge collection in silicon strip detectors". In: NIM 214.2-3 (1983), pp. 253-260. [https://doi.org/10.1016/0167-5087\(83\)90591-4](https://doi.org/10.1016/0167-5087(83)90591-4).
- [67] Felix Reidt. "Studies for the ALICE Inner Tracking System Upgrade". PhD thesis. CERN-THESIS-2016-033: Heidelberg 2016 <https://cds.cern.ch/record/2151986?ln=es>.
- [68] I. Ravasenga, "Development of Monolithic Pixel Sensors for ALICE Experiment," Università di Torino, 2015.
- [69] Suljic, Miljenko. 2016. "ALPIDE: the Monolithic Active Pixel Sensor for the ALICE ITS upgrade" <https://doi.org/10.1088/1748-0221/11/11/C11025>.
- [70] "pALPIDE-3-operations-manual", <http://sunba2.ba.infn.it/MOSAIC/ALICE-ITS/Documents/pALPIDE-3-operations-manual.pdf>

- [71] TowerJazz. Available online: <https://towersemi.com>
- [72] P. Yang, Chenfei et al. 2019. "A Prototype Readout System for the ALPIDE Pixel Sensor". IEEE Transactions on Nuclear Science. PP. 1-1. 10.1109/TNS.2019.2913335. <https://doi.org/10.1109/TNS.2019.2913335>
- [73] ALPIDE Operations Manual <https://www-subatech.in2p3.fr>
- [74] J. Bazo. 2017, Testing FLUKA on neutron activation of Si and Ge at nuclear research reactor using gamma spectroscopy. <https://arxiv.org/pdf/1709.02026.pdf>
- [75] L. Servoli et al. 2010, Characterization of standard CMOS pixel imagers as ionizing radiation detectors. Journal of Instrumentation, <https://doi.org/10.1088/1748-0221/5/07/P07003>
- [76] S. Pommé , H. Stroh, R. Van Ammel, 2019, "The ^{55}Fe half-life measured with a pressurised proportional counter", Applied Radiation and Isotopes. <https://doi.org/10.1016/j.apradiso.2019.01.008>
- [77] Bé et al. Table of Radionuclides (Vol. 3 - A = 3 to 244). http://www.lnhb.fr/nuclides/Fe-55_tables.pdf.
- [78] Berger et al. 2005, "Stopping-Power and Range Tables for Electrons, Protons, and Helium Ions". <http://www.nist.gov/pml/data/star/index.cfm>.
- [79] J. H. Hubbell and S. M. Seltzer, 2004. "X-Ray Mass Attenuation Coefficients" <https://physics.nist.gov/PhysRefData/XrayMassCoef/ComTab/air.html>
- [80] hanilnuclear.com.kr, <http://hanilnuclear.co.kr/wp-content/uploads/2018/08/Fe-55.pdf>, accessed July 2020.
- [81] <https://www.photonicsolutions.co.uk/upfiles/CFR.pdf> 2020

- [82] Jui-Teng Lin, Progress of medical lasers: Fundamentals and Applications. <https://doi.org/10.15761/MDDE.1000111>.
- [83] Martienssen W. 2004 Landolt-Börnstein-Laser Physics and Applications vol 1, (Berlin: Springer).
- [84] C. Huber, S. Orlov, P. Banzer, and G. Leuchs, 2013, "Corrections to the knife-edge based reconstruction scheme of tightly focused light beams," Opt. Express 21, 25069-25076 <https://doi.org/10.1364/OE.21.025069>
- [85] R. Paschotta, article on Gaussian beams in the Encyclopedia of Laser Physics and Technology, 1. edition October 2008, Wiley-VCH, ISBN 978-3-527-40828-3 <https://www.rp-photonics.com/>
- [86] RP Photonics https://www.rp-photonics.com/gaussian_beams.html 2021.
- [87] Alda, Javier, 2003, "Laser and Gaussian Beam Propagation and Transformation", Encyclopedia of Optical Engineering. <https://doi.org/10.1081/E-E0E2-120009751>
- [88] O. Svelto, 2013, "Principles of Laser", fifth edition Springer Italy. <https://doi.org/10.1007/978-1-4419-1302-9>
- [89] Data-sheets rectangular step variable metallic neutral density filters NDL-25S-4, https://www.thorlabs.com/NewGroupPage9.cfm?ObjectGroup_ID=1624 2020
- [90] Datasheets photodiode PS100-5 THD, (2020), https://www.mouser.com/datasheet/2/313/PS100-5_THD_501433-586508.pdf
- [91] Brahim Haraoubia, 2018 "Nonlinear Electronics 1", ISBN, <https://doi.org/10.1016/C2017-0-01442-8>

- [92] Omnivision 5647 https://cdn.sparkfun.com/datasheets/Dev/RaspberryPi/ov5647_full.pdf
- [93] Datasheets LDR, <https://www.kth.se/social/files/54ef17dbf27654753f437c56/GL5537.pdf> 2020.
- [94] Datasheets LED laser model LBS-532, <https://www.laserglow.com/img/specifications/LBS-532-TC.pdf> 2020.
- [95] Datasheets Helium-Neon gas laser model 1507-0, <https://resource.lumentum.com/s3fs-public/technical-library-items/schn1500-ds-cl-ae.pdf> 2020.
- [96] M. Bonnet del Alamo. "Laser spot measurement using simple devices" 2021 <https://aip.scitation.org/doi/pdf/10.1063/5.0046287>.
- [97] A. Alsultanny, 2006, "Laser Beam Analysis Using Image Processing" Journal of Computer Science 2 (1): 109-113, <https://citeseerx.ist.psu.edu/viewdoc/download?doi=10.1.1.165.7474&rep=rep1&type=pdf>
- [98] Wikimedia Commons, Rayleigh length, 2009, https://en.wikipedia.org/wiki/Rayleigh_length#/media/File:GaussianBeamWaist.svg
- [99] Dataray inc: Wincamd-xhr-1/2" cmos beam profiling camera system" <https://dataray.com/products/wincamd-xhr-1-2-cmos-beam-profiler-system> (2020-12)
- [100] Axiom optics: Cincam cmos 1204 rayci lite. <https://axiom-optics.myshopify.com/collections/laser-beam-characterization/products/cincam-cmos-1204-rayci-lite> (2020-12)
- [101] Thorlabs: Bc106n-vis/m-ccd camera beam profiler <https://www.thorlabs.com/thorproduct.cfm?partnumber=BC106N-VIS/M> accessed: 2020-12